Spherically-symmetric naked singularities with minimally-coupled scalar fields: effects of self-interaction and quasi-normal modes

Dissertation
zur Erlangung des Doktorgrades
der Naturwissenschaften

vorgelegt beim Fachbereich Physik
der Johann Wolfgang Goethe-Universität
in Frankfurt am Main

von
Oleksandr Stashko
aus Zhytomyr, Ukraine

Frankfurt am Main 2023
D30

vom Fachbereich Physik der
Johann Wolfgang Goethe-Universität als Dissertation angenommen.

Dekan: Prof. Dr. Roger Erb

Gutachter: Prof. Dr. Luciano Rezzolla
Prof. Dr. Valery Zhdanov

Datum der Disputation: 24.11.2023

Acknowledgements

In this acknowledgment, I would like to express my gratitude to all the people with whom I had the opportunity to communicate during my PhD.

First and foremost, I would like to express my enormous gratitude to my supervisors, Valery Zhdanov and Luciano Rezzolla, for their insightful discussions and invaluable assistance throughout my PhD. Without their support, this work would not have been possible.

I am deeply appreciative of Igor Klebanov, Horst Stöcker, Luciano Rezzolla, and Jan Steinheimmer for their tremendous support during these challenging times, which have affected all Ukrainians.

I am grateful to my friends and co-authors, Oleh Savchuk, Roman Poberezhnuk, Vladimir Kuznetsov, Volodymyr Vovchenko, Mark Gorenstein, Horst Stöcker, Leonid Satarov, Igor Mishustin, Nikolay Sukhov, Anton Motornenko, Nadezhda Fishchenko, Elias Most and Ivan Pidhurskyi for the scientific and personal support they have provided me with. Their contributions have been invaluable.

I am immensely appreciative to the Frankfurt Institute for Advanced Studies, and particularly grateful to Horst Stöcker for his warm hospitality and invaluable support.

I am enormously thankful to Igor Klebanov, Lyman Page, Elizabeth Olson, Nikolay Sukhov, Nadezhda Fishchenko, and Elias Most, for their assistance during my time in Princeton.

Finally, I am profoundly thankful to my parents and grandparents for everything they have done for me.

Zusammenfassung

In dieser Dissertation schlagen wir eine detaillierte Untersuchung von Lösungen der Einstein-Gleichungen mit statischen, minimal gekoppelten selbstwechselwirkenden skalaren Feldern vor, die statische kugelsymmetrische Konfigurationen mit asymptotisch flachem Raum-Zeit-Verlauf in der Allgemeinen Relativitätstheorie beschreiben. Das Hauptmerkmal besteht darin, dass wir nichtlineare Effekte aufgrund verschiedener Selbstwechselwirkungspotenziale untersuchen. Ein weiteres Merkmal sind die nackten Singularitäten, die in statischen Systemen mit skalaren Feldern häufig auftreten und eine besondere Beachtung erfordern, wenn das asymptotische Verhalten in der Nähe der nackten Singularität betrachtet wird.

In der Regel gibt es keine analytischen Lösungen für die untersuchten Probleme, und ein erheblicher Teil der Dissertation befasst sich mit numerischen Simulationen. Bevor jedoch Berechnungen durchgeführt werden, ist es wichtig, sich über das qualitative Verhalten der Ergebnisse im Klaren zu sein. In diesem Zusammenhang wird besonderes Augenmerk auf allgemeine Eigenschaften der Lösungen gelegt. Dies bestimmt die Hauptforschungsrichtungen in dieser Arbeit:

- Globale und asymptotische Eigenschaften der statisch kugelsymmetrischen Konfiguration, die durch die Einstein-Gleichungen in Gegenwart von statischen, minimal gekoppelten selbstwechselwirkenden skalaren Feldern beschrieben wird.

- Numerische Analyse von statisch kugelsymmetrischen Lösungen mit spezifischer Wahl der Selbstwechselwirkung des skalaren Feldes.
  - Untersuchung der linearen Stabilität der entsprechenden Lösung gegenüber gravitativen (ungeradzahligen) Störungen.
  - Untersuchung der Bewegung von Testteilchen mit Schwerpunkt auf der Struktur der Verteilung stabiler kreisförmiger Bahnen und möglicher Beobachtungsmerkmale.

Auf diesem Weg betrachten wir:

(a) Die allgemeine Form von monotonen, positiv-definierten, exponentiell begrenzten Selbstwechselwirkungspotenzialen $V(\phi) \geq 0,\ \phi V'(\phi) > 0,\ V(\phi) \leq e^{\kappa\phi}$.

(b) Ein stark nichtlineares Selbstwechselwirkungspotenzial in der Form $V(\phi) = w \sinh\big(\kappa\phi^{2n}\big)$.

(c) Wir erzeugen auch eine Familie exakter Lösungen mit speziell ausgewählten nichtmonotonen Potenzialen (einschließlich des sogenannten "Mexikanerhut"-Potenzials).

(d) Als konkretes Beispiel für Fall (a) verwenden wir $V(\phi) = w\phi^{2n}$ mit $n > 2$.

Anschließend untersuchen wir in Kapitel 1 globale und asymptotische Eigenschaften von Konfigurationen mit N minimal gekoppelten statischen, selbstwechselwirkenden skalaren Feldern unter spezifischen Anforderungen an das Selbstwechselwirkungspotenzial $V(\Phi)$, das dem Fall (a) entspricht.

Wir zeigen, dass die entsprechenden Lösungen der Einstein-Skalare-Feld-Gleichungen im Bereich $r \in (0, \infty)$ existieren, wobei r den radialen Krümmungskoordinaten (Schwarzschild-ähnliche Koordinaten) darstellt. Wir zeigen, dass es keine sphärischen Singularitäten bei $r > 0$ gibt und dass immer eine nackte Singularität im Zentrum vorliegt. Wir bestimmen rigoros das asymptotische Verhalten der metrischen Funktionen und des skalaren Feldes in der Nähe der Singularität bei $r = 0$ für das allgemeine Selbstwechselwirkungspotenzial (Fall (a)), wenn $\kappa < 32\pi/N$ gilt.

Als Beispiel betrachten wir eine spezifische Wahl von $V(\phi) = w\phi^{2n}$ mit $n > 2$ (Fall (d)) und untersuchen sie im Detail. Für diesen Fall bestimmen wir die Terme höherer Ordnung in den asymptotischen Erweiterungen in der Nähe der Singularität. Wir analysieren das mögliche asymptotische Verhalten des skalaren Feldes am räumlichen Unendlichen in Abhängigkeit vom Wert von n. Um die numerischen Lösungen zu konstruieren, verwenden wir asymptotische Lösungen am räumlichen Unendlichen als Anfangsbedingungen und führen eine Rückwärtsintegration bis zur Singularität bei $r = 0$ durch. Um unsere Vorgehensweise zu rechtfertigen, schreiben wir die Einstein-Skalare-Feld-Gleichungen in einer Integralform um und zeigen, dass das iterative Verfahren mit der 0. Iteration in Form der asymptotischen Lösungen am räumlichen Unendlichen konvergiert und zu einer eindeutigen Lösung führt. Als Ergebnis erhalten wir eine dreiparametrige Lösungsfamilie, die eindeutig durch die Masse der Konfiguration M, die 'skalare Ladung' $Q = \lim_{r\to\infty} r\phi(r)$ und die Potenz n bestimmt ist. Das qualitative Verhalten der Lösungen ähnelt dem Fall der Fisher-Janis-Newman-Winicour-Lösung.

In Kapitel 2 präsentieren wir ein Beispiel, das die Konsequenzen einer

Verletzung der Bedingung der exponentiellen Begrenztheit (Fall (b)) veranschaulicht.

Zunächst zeigen wir, dass es in der flachen Raumzeit sphärische Singularitäten bei $r = r_s > 0$ gibt, auch wenn die Anforderungen für Fall (a) erfüllt sind. Anschließend betrachten wir ein skalares Feld mit einem exponentiell unbegrenzten Selbstwechselwirkungspotenzial der Form $V(\phi) = w \sinh\big(\kappa\phi^{2n}\big)$ für $n > 2$ und zeigen das Auftreten von sphärischen Singularitäten in der gekrümmten Raumzeit bei $r = r_s > 0$. Wir bestimmen die genaue Form der asymptotischen Lösungen in der Nähe der Singularität bei $r = r_s$. In diesem Fall ist das asymptotische Verhalten qualitativ anders im Vergleich zum regulären Fall. Wir überprüfen unsere Ergebnisse durch numerische Lösungen. Wir bestimmen auch die Abhängigkeiten von r_s als Funktionen der Konfigurationsparameter M, Q, n.

In Kapitel 3 finden wir zwei exakte Lösungen der Einstein-Skalarfeld-Gleichungen. Die erste Lösung ist eine Verallgemeinerung der Fisher-Janis-Newmann-Winicour-Lösung in Anwesenheit von N skalaren Feldern ohne Selbstwechselwirkung. Die Form der erhaltenen Lösung ist genau die gleiche wie im Fall eines einzelnen skalaren Feldes.

Die zweite Lösung ist eine zweiparametrige Lösungsfamilie (Fall (c)) mit einem masselosen nichtlinearen skalaren Feld. Für verschiedene Parameterkombinationen können die Lösungen Raumzeiten mit nackten Singularitäten oder Schwarzen Löchern beschreiben. Die Form der Selbstwechselwirkung ähnelt dem sogenannten "Mexikanischen Hut"-Potential.

In Kapitel 4 untersuchen wir die lineare Stabilität gegenüber ungeradzahligen Störungen und die damit verbundene Frage der ungeradzahligen Quasinormalmoden-Spektren. Wir leiten die Master-Gleichung für lineare ungeradzahlige Störungen her und zeigen, dass die Konfigurationen in den Fällen (a, b, d) aufgrund des positiv definierten effektiven Potentials V_{eff} in der Wellengleichung linear stabil sind.

Im Fall der speziellen Lösungsfamilie (Fall (c)) kann es für bestimmte Parameterwerte im Schwarzen-Loch-Fall zu $V_{\text{eff}} < 0$ in der Nähe des Horizonts kommen, was auf Instabilität hindeuten kann. Wir zeigen jedoch, dass solche Konfigurationen (im Allgemeinen) stabil sind, indem wir die Methode der S-Deformation verwenden. Im Fall einer nackten Singularität gilt $V_{\text{eff}} > 0$ und die Konfigurationen sind ebenfalls stabil.

In Anwesenheit einer nackten Singularität ist die Raumzeit nicht mehr global hyperbolisch, was bedeutet, dass die Zeitevolution nicht eindeutig ist. Gemäß Wald [1] können wir eine eindeutige Zeitevolution sicherstellen, wenn es eine eindeutige selbstadjungierte Erweiterung $\mathcal{H}$ gibt. Dabei steht $\mathcal{H}$ für den räumlichen Teil des Wellenoperators. Wenn $\mathcal{H}$ nicht wesentlich selbstadjungiert ist, hängt die Dynamik von der spezifischen Wahl der selbstadjungierten Erweiterung ab, d.h. von der Wahl einer speziellen Randbedingung an der Singularität.

Für die Fälle (a, d) mit $\kappa < 32\pi$ zeigen wir die wesentliche Selbstadjungiertheit von $\mathcal{H}$. Im Fall (b) ist $\mathcal{H}$ nicht wesentlich selbstadjungiert. Im Fall (c) ist $\mathcal{H}$ ebenfalls ein wesentlich selbstadjungierter Operator.

Für alle Fälle mit nackten Singularitäten legen wir die Null-Dirichlet-Randbedingungen an der Singularität fest und verwenden eine Gauss'sche Anfangsstörung, um die Master-Wellengleichung numerisch zu lösen. Mit Hilfe der Prony-Methode extrahieren wir die Werte der fundamentalen QNM-Frequenzen.

Im Fall des Potentials mit Potenzgesetz (Fall d) gibt es signifikante numerische Unterschiede in ω im Vergleich zu den Schwarzschild- und FJNW-Fällen. Es ist wichtig zu beachten, dass $\omega(M, Q, n)$ auch für sehr kleine Skalarfelder vom Schwarzschild-Fall abweicht. Bei ausreichend großen Werten von n nähert sich ω den FJNW-Frequenzen an, aber aufgrund der nichtlinearen Selbstwechselwirkung bleibt eine geringe Abweichung bestehen.

Im Fall (b) ist die Situation analog zum vorherigen Fall. Die Werte von ω für $\kappa = 1$ ähneln denen im Fall (d).

Im Fall (c) zeigen sich diskontinuierliche Trajektorien der fundamentalen QNM-Frequenzen aufgrund des Auftretens von Eroberer-Moden in den Lösungen der Master-Wellengleichung. Darüber hinaus bleiben die Werte von ω während des Übergangs von einem Schwarzen Loch zu einer nackten Singularität kontinuierlich.

Im letzten Abschnitt von Kapitel 4 untersuchen wir die Stabilität von skalaren, vektoriellen und Dirac-Feldern auf dem Hintergrund der Kehagias-Sfetsos-nackten Singularität. Vorherige Überlegungen in [2] lieferten fehlerhafte Ergebnisse bezüglich der Instabilität von Testfeldern mit $l > 1$. Daher zeigen wir die Stabilität von Testfeldern mit $l > 1$ und ermitteln die korrekten Werte der QNM-Frequenzen.

In Kapitel 5 untersuchen wir detailliert die kreisförmige Bewegung von Testpartikeln für alle zuvor betrachteten Lösungen. Wir bestimmen und kategorisieren die möglichen Verteilungen stabiler Kreisbahnen um die Konfigurationen. Die Klassifizierung umfasst die Schwarzschild-ähnlichen Konfigurationen, bei denen die Kreisbahnen den gesamten Raum ausfüllen, sowie Konfigurationen, die zwei oder mehr getrennte Ringe um das Zentrum enthalten. Für alle diese Fälle bestimmen wir die Parameterbereiche, in denen solche Konfigurationen auftreten.

Im Fall (d) bestehen die Hauptunterschiede zur FJNW-Lösung darin, dass es Kreisbahnen mit Radien $r_b/M > 6$ gibt und eine Verteilung stabiler Kreisbahnen mit drei Bereichen.

Im Fall (b) gibt es immer einen Ring instabiler Kreisbahnen in der Nähe der Singularität. Ähnlich wie im Fall (d) beobachten wir eine Verteilung stabiler Kreisbahnen mit drei Bereichen.

Im Fall (c) treten getrennte Verteilungen stabiler Kreisbahnen sowohl für Schwarze Löcher als auch für nackte Singularitäten auf. Der Hauptunterschied besteht darin, dass im Fall einer nackten Singularität eine abstoßende Kugel vorhanden ist, auf der ein Teilchen in Ruhe verweilen kann, ohne Drehimpuls zu haben.

Für verschiedene Arten von Verteilungen stabiler Kreisbahnen erstellen wir Abbildungen von dünnen Akkretionsscheiben, die aus flachen Verteilungen von Kreisbahnen bestehen und für einen entfernten Beobachter mit verschiedenen Neigungen zur Sichtlinie sichtbar sind. Alle diese Abbildungen enthalten den dunklen Fleck in der Mitte, wie bei einem gewöhnlichen Schwarzen Loch. Die Ursache für diesen dunklen Fleck in Abwesenheit einer Photonensphäre liegt in der abstoßenden Natur der Singularität.

Contents

Chapter 1

Introduction

For over a century, Einstein's General Relativity (GR) remains to be the main theory for describing gravitational phenomena. She has successfully passed numerous tests, both in the weak-field regime [3,4] and new appeared test in the strong-field regime [5–7], including the direct observation of gravitational waves by the LIGO collaboration [8] and the first images of black holes obtained by the Event Horizon Telescope (EHT) collaboration [9–11]. Even satisfied all possible observations, GR has several problems [12,13], preventing her from being the ultimate theory of gravity. Such circumstances requires from us to search models beyond standard GR and find more precise boundaries where GR is valid. As a result, a wide range of modified gravity theories have been already proposed [14–16], like non-metric theories, theories with additional fields or extra dimensions, and so on.

Compact objects can pretend on the role of valuable astrophysical laboratories for searching of the smoking guns of modified gravity models and seeking potential signatures of "new physics". Typically, black holes have served this role, and recent observations from the EHT and LIGO collaborations are largely in line with expectations for the standard Kerr black hole model. However, a wide variety of exotic compact objects (ECOs) exist, including naked singularities [17,18], wormholes [19], boson stars [20,21], Dirac stars [22,23], gravastars [24] and so on [25].

Interest in studying ECOs has grown substantially after the publication of images of the accretion disk in the core of M87 and Sgr A* by EHT [9–11]. Also it has been discovered that ECOs can closely resemble black holes [25–35] and play role of their mimickers.

Testing of the observational properties of the corresponding objects can answer us about presence and properties of such solutions in our world.

One of the primary sources of observational data for compact objects comes from the radiative properties of the surrounding matter, such as accretion disks and jets, as well as their resulting images from the perspective of distant observer. A key aspect of this consideration is the structure of test particles stable circular orbits distributions, especially if it contains distributions in a form of of multiple non-connected rings of SCOs. As well as form and geometrical properties of ECOs shadows visible for a distant observer. A number of authors have studied various properties, including the circular motion of test particles [36–49], images of accretion disk [50–59], radiation fluxes and luminosity [59–68], profiles of Fe-Kα lines [69–75], gravitational lensing [76–84] and many more.

The second source of observational data is due to gravitational wave astronomy. In particular, perturbed astrophysical objects exhibit relaxation through the emission of exponentially damped oscillating modes during the ringdown phase. These oscillations, known as quasi-normal modes [85–87], their values and their damping times can be used to explore the non-GR solutions and detect deviations from standard GR scenarios [88–91], particularly in light of forthcoming measurements by LIGO and LISA [92].

One of the natural approaches to modify GR with preserving her main properties is the introduction of new interacting fields. Among these, scalar-tensor theories [93–95] are the simplest and most popular, where scalar fields play role of an additional degree of freedom. At present, the sole fundamental scalar field detected in the natural world is the Higgs field. However, the existence of other fundamental scalar fields, for example, active in the Early Universe during the inflation or as models of the dark matter and dark energy [96–99] cannot be rule out. Considering Occam's razor principle, in this thesis, we focus on the simplest model with a minimally coupled scalar field.

The typical type of static solutions with scalar field is the naked singularity. Naked singularity can be roughly defined as singularities visible to a distant observer. According to the Cosmic Censorship hypothesis [100, 101], this type of solutions is considered as pathological and be forbidden in the real Universe. However, this remains an open question, as this hypothesis has not proven yet. Such configurations can emerge as a result of the gravitational collapse [102–105] of non-homogeneous matter with some specific initial conditions. They also appear as exact solutions of the Einstein equations.

The first exact solution of the Einstein equations involving a static linear massless scalar field was obtained by Fisher [17]. Subsequently, alternative formulations of the solution were found by Janis, Newman, and Winicour [106], as well as Wyman [107]. Virbhadra [108] shown the equivalence of these solutions. Fisher solution has been extensively studied from various points of view [32, 51, 52, 109–114]. Currently, there are exact solutions with non-linear scalar fields (not limited to naked singularities) but with complicated and exotic forms of self-interaction potentials [115–119]

In this thesis, we provide a comprehensive analysis of static spherically symmetric asymptotically flat configurations with non-linear scalar fields, including those described by the most commonly used self-interaction potentials.

Structure of the thesis

In Chapter 2, we formulate the basic properties for N minimally coupled static self-interacting scalar fields with specific requirements on the self-interaction potential $V(\Phi)$. We provide a proof that spherically symmetric asymptotically flat solutions of the joint system of the Einstein-scalar field equations are regular for all values of $r > 0$ in the curvature coordinates. We rigorously establish the asymptotic behavior of the metric and the scalar field near $r = 0$. To validate our results, we carry out a detailed numerical study of a case with a power-law self-interaction potential $V(\phi) = w\phi^{2n}$.

In Chapter 3, we demonstrate the possibility of "spherical singularities" in the case of flat space-time and for exponentially unbounded self-interaction potentials. We find the asymptotic behavior of the metric functions and the scalar field near the singularity for the specific case of $V(\phi) = w \sinh\big(\kappa\phi^{2n}\big)$. Additionally, we perform numerical simulations to study the corresponding full solutions.

In Chapter 4, we present two exact solutions of the Einstein-scalar field equations. The first solution is the generalization of the Fisher-Janis-Newman-Winicour (FJNW) solution in the presence of N identical scalar fields. The second solution represents a two-parametric "toy-model" family of solutions that contains both naked singularities and black holes.

In Chapter 5, we consider the linear stability against odd-parity gravitational perturbations. We demonstrate that all previously considered solutions are stable under odd-parity perturbations. Furthermore, we determine the values of the corresponding fundamental quasinormal mode frequencies. In the final section, we revisit the question of the stability of the Kehagias-Sfetsos naked singularity.

In Chapter 6, we provide a detailed analysis of circular test particle motion for all previously considered solutions. We demonstrate the possible images of Keplerian accretion disks as seen by a distant observer.

The conclusions of the thesis are presented in Chapter 7, where we summarize the main results.

This thesis is based on the following papers

1. **O. Stashko**, O. Savchuk, V. Zhdanov, Quasi-normal modes of naked singularities in presence of non-linear scalar fields. *Physical Review D*, **109**, 024012, 2023.

2. **O. Stashko**, V. Zhdanov, Singularities in static spherically symmetric configurations of general relativity with strongly nonlinear scalar fields, *Galaxies*, 9(4):72, 2021.

3. **O. Stashko**, V. Zhdanov, N. Alexandrov, Thin accretion discs around spherically symmetric configurations with nonlinear scalar fields. *Physical*

Review D. **104**, 2021.

4. V. Zhdanov, **O. Stashko**, Static spherically symmetric configurations with N nonlinear scalar fields: Global and asymptotic properties. *Physical Review D*, **101**, 2020.

5. **O. Stashko**, V. Zhdanov, Black Hole Mimickers in Astrophysical Configurations with Scalar Fields. *Ukrainian Journal of Physics*, **64(11)**, 1078, 2019.

6. **O. Stashko**, V. Zhdanov, Spherically symmetric configurations of General Relativity in presence of scalar fields: separation of circular orbits. *General Relativity And Gravitation*. **50**, 2018.

Chapter 2

Self-interaction scalar fields with exponentially bounded potentials

2.1 Basic relations

In this chapter, we consider the general properties of solutions of the Einstein equations with N minimally-coupled real scalar fields $\Phi = \{\phi_1, ..., \phi_N\}$ in space-time of four dimensions. Namely, we consider the action

$$S = \int \sqrt{|g|} \left(-\frac{R}{16\pi G} + L_s \right), \tag{2.1}$$

where L_s is the Lagrangian density of scalar fields

$$L_s = \frac{1}{2} \sum_{i=1}^{N} \partial_\mu \phi_i \partial^\mu \phi_i - V(\Phi), \tag{2.2}$$

and $V(\Phi)$ is the self-interaction potential of scalar fields.

Properties of the $V(\Phi)$ are strongly affect on possible types of solution. In particular, for the static scalar fields with positive-defined potential $V(\Phi)$, black hole solutions are excluded according to no-hair theorems [120–122]. Likewise, regular solutions are also not possible [115, 123]. The most typical solutions which occur in such cases are naked singularities. Hence, we restrict ourselves with this case, i.e. we assume that $V(\Phi) \in C^2$ and

$$V(\Phi) \geq 0, \tag{2.3}$$

and

$$\phi_i \frac{\partial V}{\partial \phi_i} \geq 0, \quad i = 1, ..., N, \tag{2.4}$$

We assume that there are positive constants C_0, C_0', κ, and κ', such that

$$|V(\Phi)| < C_0 \exp(\kappa\|\Phi\|), \tag{2.5}$$

and for all $i = 1, 2, ..., N$

$$\left|\frac{\partial V}{\partial \phi_i}\right| < C_0' \exp(\kappa'\|\Phi\|), \tag{2.6}$$

where $\|\Phi\| = \sqrt{\sum_i \phi_i^2}$ is the Euclidean norm of the N-component vector Φ. In fact, (2.5, 2.6) are not independent estimates, if (2.6) is valid, then

$$V = \int\limits_0^{\phi_i} \frac{\partial V}{\partial \phi_i} d\phi_i < \int\limits_0^{\phi_i} C_0' e^{\kappa'\|\Phi\|} d\phi_i < \int\limits_0^{\phi_i} C_0' e^{\kappa' \sum\limits_i |\phi_i|} d\phi_i < C_0'' e^{\kappa' \sum\limits_i |\phi_i|}. \tag{2.7}$$

Therefore, only one (2.6) estimate is necessary.
The Einstein equations

$$R_\mu^\nu - \frac{1}{2}\delta_\mu^\nu R = 8\pi T_\mu^\nu\,. \tag{2.8}$$

The Klein-Gordon equations for scalar fields follow from (2.2)

$$g^{\mu\nu}\nabla_\mu\nabla_\nu\phi_i = -V_i'(\Phi), \quad i = 1, ..., N; \tag{2.9}$$

The energy-momentum tensor for the scalar field is defined in the standard way

$$T_{\mu\nu} = \sum_{i=1}^{N} \partial_\mu\phi_i\partial_\nu\phi_i - g_{\mu\nu}L_s\,. \tag{2.10}$$

We assume that the space-time is a static, spherically-symmetric and asymptotically-flat with the metric $g_{\mu\nu}$, which has the following form in curvature coordinates

$$ds^2 = e^{\alpha(r)}dt^2 - e^{\beta(r)}dr^2 - r^2(d\theta^2 + (\sin\theta)^2 d\varphi^2), \tag{2.11}$$

For metric (2.11), we can write down Einstein equations in the explicit form

$$\frac{d}{dr}\left[r\left(e^{-\beta} - 1\right)\right] = -8\pi r^2 T_0^0\,, \tag{2.12}$$

where $T_0^0 = e^{-\beta}\sum\limits_{i=1}^{N} \phi_i'^2/2 + V(\Phi)$, $\phi_i' = d\phi_i/dr$,

$$re^{-\beta}\frac{d\alpha}{dr} + e^{-\beta} - 1 = -8\pi r^2 T_1^1, \tag{2.13}$$

where $T_1^1 = -e^{-\beta} \sum\limits_{i=1}^{N} \phi_i'^2/2 + V(\Phi)$.
The explicit form of the Klein-Gordon equation (2.9)

$$\frac{d}{dr}\left[r^2 e^{\frac{\alpha-\beta}{2}} \frac{d\phi_i}{dr}\right] = r^2 e^{\frac{\alpha+\beta}{2}} V_i'(\Phi)\, i = 1, ..., N, \tag{2.14}$$

We assume that the corresponding space-time is asymptotically-flat, i.e.

$$\lim_{r\to\infty}\left[r(e^{\alpha}-1)\right] = \lim_{r\to\infty}\left[r(e^{-\beta}-1)\right] = -r_g, \tag{2.15}$$

where $r_g = 2M$ and $M > 0$ is the mass of configuration.

We assume that components ϕ_i of the SF Φ are independent and at spatial infinity they can be treated as scalar fields in the flat space, $\Phi(r) \to 0$ for $r \to \infty$ and

$$\exists K: \quad r^2\|\Phi'(r)\| < C < \infty, \tag{2.16}$$

from where, we have

$$r\|\Phi(r)\| < C\,. \tag{2.17}$$

We define the solutions of Einstein's equations in the following way.

Definition. The set of functions $\{\alpha(r), \beta(r) \in C^1, \Phi(r) \in C^2\}$ is called a solution of the Einstein-scalar field equations (2.12 – 2.14) on (r_0, ∞), $r_0 \geq 0$, if they satisfy equations (2.12 – 2.14) on (r_0, ∞) and conditions (2.15-2.16).

We need to note that at this stage we confine ourselves by condition (2.16), but we do not impose a more stringent condition on $\phi_i(r)$ for $r \to \infty$ that ensures the uniqueness of the solution, because it is different for different kinds of potentials.

The equations (2.12 – 2.13) can be rewritten in more convenient form

$$\alpha' + \beta' = 8\pi r \sum_{i=1}^{N} \phi_i'^2\,, \tag{2.18}$$

$$\beta' - \alpha' = \frac{2}{r} + e^{\beta}\left[16\pi r V(\Phi) - \frac{2}{r}\right]\,, \tag{2.19}$$

Now we introduce new functions

$$X = e^{(\alpha+\beta)/2}, \quad Y = re^{(\alpha-\beta)/2}\,, \tag{2.20}$$

and

$$Z_i = -rY\phi_i', \quad i = 1, ..., N. \tag{2.21}$$

for which we obtain an equivalent system of equations

$$\frac{dX}{dr} = 4\pi \frac{X}{rY^2} \sum_{i=1}^{N} Z_i^2\,, \tag{2.22}$$

$$\frac{dY}{dr} = X\left[1 - 8\pi r^2 V(\Phi)\right] . \tag{2.23}$$

The Klein-Gordon equation (2.14) can be rewritten in the form of two first-order differential equations

$$\frac{dZ_i}{dr} = -r^2 X V_i' , \tag{2.24}$$

$$\frac{d\phi_i}{dr} = -\frac{Z_i}{rY} . \tag{2.25}$$

for $i = 1, ..., N$.

Then, the conditions (2.15) in terms of functions X, Y, and Z are

$$\lim_{r\to\infty} [r(X-1)] = 0, \quad \lim_{r\to\infty} (Y - r) = -r_g . \tag{2.26}$$

and for the conditions (2.16, 2.17), we have

$$|Z_i(r)| < K, \quad \lim_{r\to\infty} [\phi_i(r) Z_i(r)] = 0. \tag{2.27}$$

2.2 Regularity of solutions for $r > 0$

We are interested in the regularity properties of the solutions of the Einstein-SFs equations on the interval $r \in (0, \infty)$ in the presence of the some general self-interaction potential $V(\Phi)$. This self-interaction potential is assumed to fulfill certain conditions (2.5, 2.6). To prove regularity, we need to exclude the possibility of certain special cases:

$$X(r) \to 0, \ Y(r) \to 0, \ |Z_i(r)| \to \infty, \ |\phi_i(r)| \to \infty,$$

for $r \to r_0 + 0$ for some $r_0 > 0$.

Throughout this Chapter, we consistently assume that there is at least one nontrivial component of Φ, i.e., $\phi_i(r) \neq 0$ for some i.

We will start our consideration by establishing the monotonicity properties of the corresponding solutions.

Lemma 1. *Let condition (2.4) is valid for all Φ, and $\alpha(r)$, $\beta(r)$ are continuously differentiable on (r_0, ∞), $r_0 \geq 0$, and satisfy (2.15). Let, for some i, $\phi_i(r) \in C^2$ is a non-trivial solution of (2.14) on this interval with conditions (2.16, 2.17). Then functions $\phi_i(r)$, $Z_i(r)$ and $d\phi_i/dr$ do not change their signs, $\phi_i(r)Z_i(r) > 0$ and $\phi_i(r)d\phi_i/dr < 0$ on (r_0, ∞).*

Proof. We begin the proof by multiplying both sides of the equation (2.24) by ϕ_i and using the equation (2.25). This gives us the equation

$$-\frac{d}{dr}(\phi_i Z_i) = \frac{Z_i^2}{rY} + r^2 X \phi_i V_i'. \tag{2.28}$$

The right-hand side of this equation is non-negative due to the condition (2.4) and positivity of X and Y functions. Therefore, the product $\phi_i Z_i$ is a non-increasing function.

Now, suppose for a contradiction that there exists an arbitrary point r_1 such that $\phi_i(r_1)Z_i(r_1) < 0$ for $r_1 > r_0$. This inequality holds for all $r > r_1$, but this is in contradiction to the assumption that $\phi_i(\infty)Z_i(\infty) = 0$. Hence, we have that $\phi_i(r)Z_i(r) \geq 0$ for $r > r_0$.

Next, we need to show that $\phi_i(r_1)Z_i(r_1) \neq 0$. Suppose, on the contrary, that $\phi_i(r_1)Z_i(r_1) = 0$. Then, we have that $\phi_i(r)Z_i(r) \equiv 0$ for $r > r_1$, which leads to $\phi_i(r)\phi_i'(r) \equiv 0$ or $\phi_i(r) = const$. However, since $\phi_i(\infty) = 0$ and $\phi_i(r)$ is non-trivial, this also leads to a contradiction. Hence, we have $\phi_i(r_1)Z_i(r_1) \neq 0$.

Finally, we can see that $\phi_i(r)Z_i(r) > 0$, which implies that both $\phi_i(r)$ and $Z_i(r)$ cannot change their signs on the interval (r_0, ∞). ∎

Throughout this Chapter, without loss of generality, we can suppose that $\phi_i(r)$ is a positive and monotonically strictly decreasing function., i.e. $\phi_i(r) > 0$, $Z_i(r) > 0$, $\phi_i'(r) < 0$.

Lemma 2. *Let conditions (2.3, 2.4) be satisfied, and let functions $\alpha(r)$, $\beta(r)$, $\Phi(r) \in C^1$ satisfy equations (2.14, 2.18, 2.19) and $\phi_i(r) \neq 0$ for $i = 1, ..., N$ in $(r_0, r_1]$, where $0 < r_0 < r_1 < \infty$. Then there exists $\eta_0 > 0$, such that $Y(r) > \eta_0$ and, for each i, we have $S_i Z_i(r) > S_i Z_i(r_1) > 0$, where $S_i = \operatorname{sign} \phi_i$.*

Proof. One can see that the right-hand side of equation (2.24) is negative, then $Z_i(r) > 0$ is a decreasing function, such that $Z_i(r) > Z_i(r_1)$ for $r < r_1$.

In view of (2.22), we know that $X(r)$ is a monotonically increasing function. Then, for $r < r_1$, we can use equations (2.22) and (2.23) and obtain the following series of estimations

$$\frac{1}{Y^2}\frac{dY}{dX} = \frac{r}{4\pi \sum_{i=1}^{N} Z_i^2}\left[1 - 8\pi r^2 V(\Phi)\right] \leq \frac{r_1}{4\pi \sum_{i=1}^{N} Z_i^2(r)} \leq \frac{r_1}{4\pi \sum_{i=1}^{N} Z_i^2(r_1)}, \tag{2.29}$$

where we have used the positivity of $V(\Phi)$ and $X'(r)$, and the monotonicity of $S_i Z_i$. After integration of (2.29), we find

$$\frac{1}{Y(r)} \leq \frac{1}{Y_1} + \frac{r_1 X_1}{4\pi \sum_{i=1}^{N} Z_i^2(r_1)} < \frac{1}{\eta_0}.$$

Hence, $1/Y(r)$ is a positive bounded function, which means that there is a positive constant η_0 such that $Y(r) > \eta_0$. ■

Lemma 3. *Let the conditions (2.5, 2.6) are fulfilled and functions* $\alpha(r)$, $\beta(r) \in C^1$, $\Phi(r) \in C^2$, $\phi_i \neq 0$ *satisfy equations (2.18, 2.19) and (2.14) on* $(r_0, r_1]$, *where* $0 < r_0 < r_1 < \infty$. *Then there exist finite limits*

$$\bar{Y}(r_0) = \lim_{r \to r_0+0} Y(r) > 0,\ \ \bar{Z}_i(r_0) = \lim_{r \to r_0+0} Z_i(r) > 0, \tag{2.30}$$

$$\bar{X}(r_0) = \lim_{r \to r_0+0} X(r) > 0,\ \ \bar{\phi}_i(r_0) = \lim_{r \to r_0+0} \phi_i(r) \neq 0. \tag{2.31}$$

Proof. By assumption $X(r_1)$ is finite. For $r \in (r_0 r_1]$ from (2.18), we have

$$X(r) = X(r_1)\exp\left\{-4\pi \int_r^{r_1} x \sum_{i=1}^{N} \phi_i'^2(x) dx\right\}. \tag{2.32}$$

After applying the integral Cauchy–Schwarz inequality, we obtain for $r < r_1$

$$|\phi_i(r) - \phi_i(r_1)| = \left| \int_r^{r_1} (\phi_i'(x)\sqrt{x}\,) \cdot \frac{1}{\sqrt{x}} \cdot dx \right| \leq$$

$$\leq \int_r^{r_1} |\phi_i'(x)|\sqrt{x} \cdot \frac{1}{\sqrt{x}} \cdot dx \leq \sqrt{\int_r^{r_1} x[\phi_i'(x)]^2 dx \, \ln(r_1/r)}\ .$$

Thus, we obtain

$$\int_r^{r_1} x[\phi_i'(x)]^2 dx \geq \frac{[\phi_i(r) - \phi_i(r_1)]^2}{\ln(r_1/r)}. \tag{2.33}$$

And using (2.32), we obtain

$$X(r) \leq X(r_1)\exp\left\{-4\pi \sum_{i=1}^{N} \frac{[\phi_i(r) - \phi_i(r_1)]^2}{\ln(r_1/r)}\right\}. \tag{2.34}$$

Finally, this inequality can be strengthened by replacing $\ln(r_1/r)$ by $\ln(r_1/r_0)$

$$X(r) \leq X(r_1)\exp\left\{-4\pi \sum_{i=1}^{N} \frac{[\phi_i(r) - \phi_i(r_1)]^2}{\ln(r_1/r_0)}\right\}. \tag{2.35}$$

Let us define $B(r)$ and $\tilde{B}_i(r)$ as follows:

$$B(r) = X(r)|V(\Phi(r))|, \quad \tilde{B}_i(r) = X(r)|V_i'(\Phi(r))|. \tag{2.36}$$

Then, from the inequalities (2.35) and (2.5), we have

$$B(r) \le C_1 \exp\left\{\sum_{i=1}^{N}\left[-4\pi\frac{[\phi_i(r)-\phi_i(r_1)]^2}{\ln(r_1/r_0)} + \kappa|\phi_i(r)|\right]\right\}, \tag{2.37}$$

where we denoted $C_1 = X(r_1)C_0 > 0$. The expression in the exponent remains bounded as a function of ϕ even if $\phi \to \infty$. It has a maximum at

$$\phi_{\max} = \phi_i(r_1) + \frac{\kappa}{8\pi}\ln(r_1/r_0),\ \ B(r) \le C_1 \exp\left\{\sum_{i=1}^{N}\left[\frac{\kappa^2\ln(r_1/r_0)}{16\pi} + \kappa\phi_i(r_1)\right]\right\}. \tag{2.38}$$

Therefore, we can conclude that $B(r)$ is a finite uniformly bounded function for $r \to r_0 + 0$.

After repeating the similar consideration for $\tilde{B}_i(r)$, we obtain

$$\tilde{B}_i(r) \le \kappa' C_2 \exp\left\{\sum_{i=1}^{N}\left[-4\pi\frac{[\phi_i(r)-\phi_i(r_1)]^2}{\ln(r_1/r_0)} + \kappa'|\phi_i(r)|\right]\right\}\frac{\phi_i}{\|\Phi\|}. \tag{2.39}$$

Then, taking into account that $\phi_i/\|\Phi\| \le 1$, we conclude that it is also a bounded function.

Thus, the expressions (2.36) and the right-hand sides of (2.23, 2.24) are bounded, which lead to the existence of the finite limits $\bar{Y}(r_0), \bar{Z}_i(r_0)$. From the Lemmas 1, 2 follow that $\bar{Y}(r_0) > 0$, $S_i\bar{Z}_i(r_0) > 0$.

Hence, the functions $\phi_i(r)$ and $|\phi_i'(r)|$ are bounded and we have a finite limits for $r \to r_0$. From (2.22), we obtain existence of $\bar{X}(r_0) > 0$.

■

Now, we can summarize our results as

Theorem 1. *Let the SF potential satisfies conditions (2.3, 2.4) and (2.5, 2.6) for all Φ. Let $\alpha(r)$, $\beta(r), \in C^1$, $\Phi(r) \in C^2$ represent a non-trivial ($\phi_i(r) \not\equiv 0$, $i = 1, ..., N$) solution of equations (2.14, 2.18, 2.19) on open interval (r_0, ∞), $r_0 > 0$ with conditions (2.15, 2.16, 2.17).*

Then

(i) there exist finite limits of functions $\alpha(r)$, $\beta(r)$, $\phi_i(r)$ and $\phi_i'(r)$ for $r \to r_0$;

(ii) solution can be regularly continued onto a left neighbourhood of r_0;

(iii) solution can be regularly continued for all $r > 0$ up to the center.

Proof. (i) This statement is the result of Lemma 3.

(ii) This statement directly follows from the existence-uniqueness theorem for ODEs and analyticity of the right-hand sides of the (2.22 – 2.25) in the neighbourhood of $\bar{X}(r_0) > 0$, $\bar{Y}(r_0) > 0$, $S_i \bar{Z}_i(r_0) > 0$, $S_i \bar{\phi}_i(r_0) > 0$.

(iii) We immediately obtain this result from statements (i), (ii) and application of the real induction to continue this solutions for all $r > 0$. ■

We should point out that the regularity for $r > 0$ doesn't rule out a singularity at the origin $r = 0$.

2.3 Asymptotic behaviour near the singularity at $r = 0$

Another crucial aspect is to consider the behavior of the asymptotic solutions near the singularity, which is necessary to gain a comprehensive understanding of the space-time geometry and properties of the singularity. This can be carried out in a similar way as we used in the proof of Lemma 3. We can prove the following Lemma.

Lemma 4. *Let conditions (2.3, 2.4) and (2.5, 2.6) are fulfilled with* $\max(\kappa^2, \kappa'^2) < 32\pi/N$. *Let* $\alpha(r), \beta(r), \phi_i(r) \not\equiv 0$ $(i = 1, ..., N)$ *represent a solution of (2.12, 2.13, 2.14) on* $(0, \infty)$ *with conditions (2.15– 2.17). Then there exist finite nonzero limits*

$$Z_{i,0} = \lim_{r \to 0+0} Z_i(r), \quad Y_0 = \lim_{r \to 0+0} Y(r), \tag{2.40}$$

such that $S_i Z_{i,0} > 0$, $Y_0 > 0$.

Proof. Let r_1 is an arbitrary point, such that $0 < r < r_1 < \infty$. After repeating consideration of the proof of Lemma 3 for $D(r) = r^2 B(r)$ in the right-hand side of (2.23) we obtain

$$D(r) = r_1^2 (r/r_1)^2 B(r) = r_1^2 e^{-2L} B(r) \leq \tag{2.41}$$

$$C_2 e^{-2L} \cdot \exp\left\{ -\sum_{i=1}^{N} \left[\frac{4\pi}{L} [\phi_i(r) - \phi_{i,1}]^2 - \kappa |\phi_i(r)| \right] \right\}, \tag{2.42}$$

where we denoted $C_2 = r_1^2 X(r_1) C_0 > 0$, $\phi_{i,1} = \phi_i(r_1)$ and $L = \ln(r_1/r)$.

Throwing off some negative terms, we obtain

$$D(r) \leq C_2 \exp\left\{ -2L + \frac{\kappa^2 N}{16\pi} L \right\} \exp\left\{ \sum_{i=1}^{N} \left[\frac{4\pi}{L} |\phi_{i,1}|^2 + \kappa |\phi_{i,1}| \right] \right\}. \tag{2.43}$$

One can see that $L \to \infty$ for $r \to 0$, but meantime $D(r)$ remains bounded if $\kappa^2 < 32\pi/N$. Then the right-hand side of (2.23) is integrable and the finite limit $Y_0 \geq 0$ exists.

After repeating the similar consideration for $r^2 X V_i'$ we obtain that the right-hand side of (2.24) is also bounded, integrable and the corresponding finite limits $Z_{i,0}$ exist.

■

Using results of Lemma 4, we can determine the asymptotic behavior of the metric functions and scalar field for $r \to 0$. From (2.25) and (2.40), we obtain for scalar field

$$\frac{d\phi_i}{dr} \sim -\frac{\zeta_{i,0}}{r}, \quad \phi_i(r) \sim -\zeta_{i,0} \ln r\,, \tag{2.44}$$

where we denoted $\zeta_{i,0} = Z_{i,0}/Y_0$. Then, from (2.18, 2.19) we obtain the leading terms for the metric functions

$$\alpha(r) \sim (\eta - 1)\ln r, \quad \beta \sim (\eta + 1)\ln r, \tag{2.45}$$

where $\eta = 4\pi \sum\limits_{i=1}^{N} \zeta_{i,0}^2$.

The scalar curvature and Kretschmann scalar both diverge for $r \to 0$ as

$$R \sim -D_1/r^{\eta+3}, \;\; R_{\alpha\beta\gamma\delta}R^{\alpha\beta\gamma\delta} \sim D_2/r^{2\eta+6}, \tag{2.46}$$

Where D_1 and D_2 depend on the explicit form of $V(\Phi)$.

We need to note that the main asymptotic terms have the same form as in the case of $V(\Phi) = 0$.

In order to determine the next order terms of the expansion near the singularity, we can use the following iteration procedure.

Let us take into account that the leading order terms are

$$X(r) \sim \chi_0 r^\eta, \;\; Y(r) \sim Y_0, \;\; Z(r) \sim Z_0, \;\; \phi(r) \sim -\zeta_0 \ln(r) \equiv \phi^0, \;\; r \to 0. \tag{2.47}$$

Then, we can seek solutions in the form

$$X(r) = r^\eta \chi(r), \;\; Y(r) = Y_0 + \gamma(r), \;\; Z(r) = Z_0 + \psi(r), \;\; \phi(r) = \phi^0 + \varphi(r), \tag{2.48}$$

where

$$\chi(0) = \chi_0, \;\; \psi(0) = 0, \;\; \gamma(0) = 0, \;\; \varphi(0) = \varphi_0. \tag{2.49}$$

The Einstein-SF equations can be rewritten in terms of the new unknown functions $\chi(r)$, $\gamma(r)$, $\psi(r)$, $\varphi(r)$ and then reduced to a system of integral equations

$$\chi(r) = \chi_0 + 4\pi \int_0^r \frac{\chi(x)}{x} \left[\frac{(2Z_0 + \psi(x))\psi(x) - \zeta_0^2(2Y_0 + \gamma(x))\gamma(x)}{(Y_0 + \gamma(x))^2} \right] dx, \tag{2.50}$$

$$\gamma(r) = \int_0^r x^\eta \chi(x) \left[1 - 8\pi x^2 V(\phi)\right] dx, \tag{2.51}$$

$$\psi(r) = -\int_0^r x^{\eta+2} \chi(x) \frac{dV}{d\phi} dx, \tag{2.52}$$

$$\varphi(r) = \varphi_0 + \int_0^r \frac{\zeta_0 \gamma(x) - \psi(x)}{x(Y_0 + \gamma(x))} dx, \tag{2.53}$$

Thus, the next order terms of the asymptotic solution near the singularity can be obtained using the fixed-point iteration procedure with the 0-th iteration in the form of (2.49).

2.4 Asymptotic behaviour at spatial infinity

For our future purposes we need to know how the scalar field behaves at spatial infinity. Assuming that components ϕ_i of SF Φ are asymptotically independent and behave like SFs in the flat space, we can limit ourselves to the case of single scalar field ϕ.

We suppose that self-interaction potential has asymptotically the power-law form for $\phi \to 0$ as $r \to \infty$.

$$V(\phi) \simeq w|\phi|^p, \quad w > 0,\ p \geq 2. \tag{2.54}$$

The scalar field equation in the flat space-time has form

$$\frac{d}{dr}\left[r^2 \frac{d\phi}{dr}\right] = pwr^2\phi|\phi|^{p-2}. \tag{2.55}$$

Depending on the value of p there are four qualitatively different cases.

(i) Massive scalar field case: $p = 2$, $w = \mu^2/2$. There is an exact solution for $r \to \infty$

$$\phi(r) = \frac{Q}{r} e^{-\mu r}, \tag{2.56}$$

or in the more precise form in the general case

$$\phi(r) \sim \frac{Q}{r^{1+\mu M}} e^{-\mu r}, \tag{2.57}$$

where Q is an arbitrary constant and M is the mass of the configuration.

For $p > 2$, we can make the following substitution

$$\phi = e^{-qt}\psi, \quad t = \ln r, \quad q = \frac{2}{p-2}, \tag{2.58}$$

that gives us the autonomous differential equation

$$\frac{d^2\psi}{dt^2} + (1-2q)\frac{d\psi}{dt} + q(q-1)\psi = pw\psi^{p-1}, \tag{2.59}$$

which can be rewritten as the two-dimensional dynamical system

$$\frac{du}{dt} = (2q-1)u - q(q-1)\psi + pw\psi^{p-1}, \quad \frac{d\psi}{dt} = u. \tag{2.60}$$

We can analyze the phase portrait of the system and qualitatively analyze the properties of the corresponding solutions by determining the critical points and their stability. Some examples of the phase portraits of the corresponding dynamical system are shown in Fig. 2.1.

The corresponding dynamical system has two critical points: The first-one at $P_1 = (\psi = 0,\, u = 0)$ with the eigenvalues

$$\lambda_1^* = q = \frac{2}{p-2}, \quad \lambda_2^* = q - 1 = \frac{4-p}{p-2}, \quad p > 2. \tag{2.61}$$

And the second-one critical point is $P_2 = (\psi = Q_0,\, u = 0)$, where

$$Q_0 = \left[\frac{q(q-1)}{pw}\right]^{q/2}, \tag{2.62}$$

with eigenvalues

$$\lambda_\pm = \frac{6-p}{2(p-2)}\left[1 \pm \sqrt{1 + \frac{8(4-p)(p-2)}{(6-p)^2}}\right], \tag{2.63}$$

for $2 < p < 4$.

(ii) If $2 < p < 4$, then $q(q-1) = 2(4-p)(p-2)^{-2} > 0$.

In this case the eigenvalues of the linearized system are real and at P_1 they are positive ($\lambda^*_{1,2} > 0$), and at P_2 have opposite signs ($\lambda_+ > 0$, $\lambda_- < 0$). Thus, P_1 is an unstable node, and P_2 is a saddle. The phase portrait is shown in Fig. 2.1(a).

The asymptotic solutions of (3.1) for $r \to \infty$ correspond to the separatrix branches that enter the saddle. For them, we have

$$\psi(t) \approx Q_0[1 + C\exp(-\lambda t)], \quad t \to \infty,$$

where C is an arbitrary constant and $\lambda = -\lambda_- > 0$. After returning to the old variables, we have

$$\phi(r) \approx \phi(r) = \frac{Q_0}{r^q}\left(1 + \frac{C}{r^\lambda}\right), \tag{2.64}$$

The rest of the solutions around the saddle point do not fulfill the condition $\phi(\infty) = 0$.

(iii) If $p > 4$, then $q(q-1) < 0$.

The eigenvalues of the linearized system at P_1 are real and have opposite signs ($\lambda^*_1 > 0$, $\lambda^*_2 < 0$), which means that P_1 is a saddle. The eigenvalues at P_2 are complex conjugate with negative real part, which means that P_2 is a stable focus.

The saddle separatrix defines by condition $\phi(\infty) = 0$, we have

$$\psi(t) \approx Qe^{-|\lambda^*_2|t},\ t \to \infty, \tag{2.65}$$

or

$$\phi(r) \approx \frac{Q}{r},\ r \to \infty, \tag{2.66}$$

where Q is an arbitrary constant.

(iv) If $p = 4$, then $q = 1$, $P_1 = P_2$ and situation becomes more complicated. One of the eigenvalues at P_1 is equal to zero ($\lambda^*_2 = 0$). Similarly to (iii), we have solutions that tend to P_1 for $r \to \infty$ as

$$\phi(r) = \frac{Q}{r\sqrt{|\ln r|}}\left(1 + \frac{3\ln|\ln r|}{4\ln r} + \dots\right), \tag{2.67}$$

where Q is an arbitrary constant. The phase portrait is shown in Fig. 2.1(b).

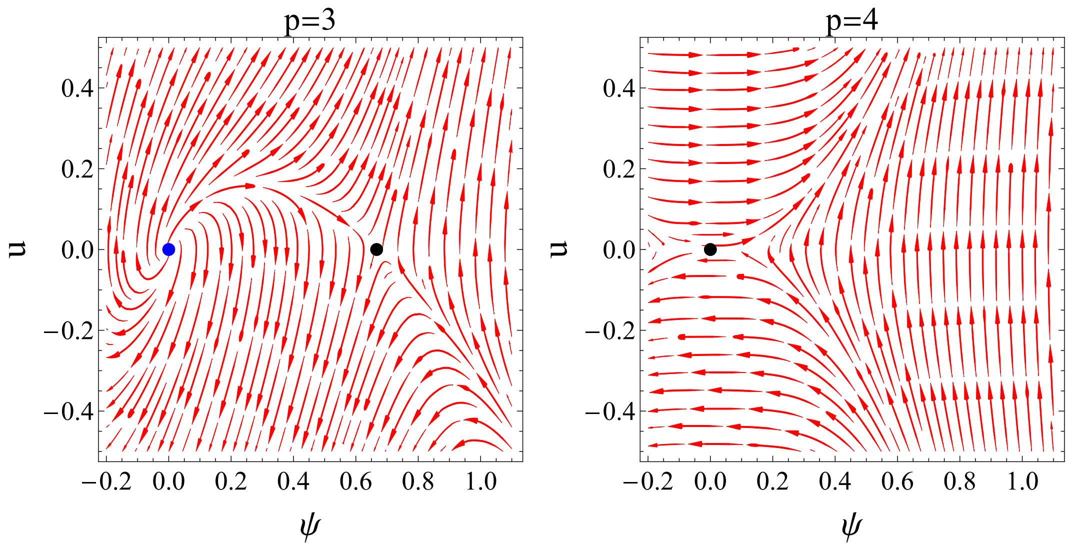

Figure 2.1: The phase portraits for $p = 3$ (left panel) and $p = 4$ (right panel).

2.5 Iteration method for solutions at large distances

In order to get a numerical solutions of the Einstein-SF equations, we take the approximate solutions at spatial infinity as initial conditions at some fixed point $r = r_\infty$ and then continue these solutions to lower values of r. However, to justify this approach, we need to demonstrate that the iterative procedure that starts from a large distance from the singularity will convergence and will lead to a unique solution. We focus on self-interaction potentials, which have the asymptotic form $V(\phi) \sim |\phi|^{2n}$ and for simplicity, we restrict our consideration only to cases with $n > 2$. The other cases can be treated in similar way.

Let us introduce new functions

$$X(r) = r\left(e^{-\beta} - 1\right), \quad Y(r) = r^2 e^{\frac{\alpha-\beta}{2}} \frac{d\phi}{dr}. \tag{2.68}$$

Then, we can rewrite the Einstein equations (2.12, 2.13) and the Klein-Gordon equation (2.14) in the form of a first order system

$$\frac{dX}{dr} = -8\pi\left[e^{-\alpha}\frac{Y^2}{2r^2} + r^2|\phi|^{2n}\right], \tag{2.69}$$

$$\frac{dY}{dr} = 2nr^2 e^{\alpha/2}\frac{\phi|\phi|^{2n-2}}{\sqrt{1+X/r}}, \tag{2.70}$$

$$\frac{d\alpha}{dr} = \frac{1}{1+X/r}\left\{-\frac{X(r)}{r^2} + 8\pi r\left[e^{-\alpha}\frac{Y^2}{2r^4} - |\phi|^{2n}\right]\right\}, \tag{2.71}$$

$$\frac{d\phi}{dr} = e^{-\alpha/2}\frac{Y}{r^2\sqrt{1+X/r}}. \tag{2.72}$$

The asymptotic flatness conditions transform to

$$\lim_{r\to\infty} X(r) = -r_g, \quad \lim_{r\to\infty} Y(r) = -Q, \quad \lim_{r\to\infty} [r\alpha(r)] = -r_g, \;\; r_g = 2M. \tag{2.73}$$

And (2.16) also transforms as

$$\lim_{r\to\infty}[r\phi(r) - Q] = -\lim_{r\to\infty} r\int_r^\infty \frac{x^2 d\phi/dx + Q}{x^2} = 0,$$

or, we have

$$\lim_{r\to\infty}[r\phi(r)] = Q. \tag{2.74}$$

For our purposes, it is convenient to single out the dominating terms for $r\to\infty$ in (2.71, 2.72). We have

$$\frac{d\alpha}{dr} = \frac{r_g}{r^2(1-r_g/r)} + D(Z,r)\,, \tag{2.75}$$

$$\frac{d\phi}{dr} = -\frac{Q}{r^2\sqrt{1-r_g/r}} + E(Z,r)\,, \tag{2.76}$$

where we denoted

$$D(Z,r) = \frac{1}{1+X/r}\left\{-\frac{X+r_g}{r^2(1-r_g/r)} + 8\pi r\left[e^{-\alpha}\frac{Y^2}{2r^4} - |\phi|^{2n}\right]\right\}. \tag{2.77}$$

and

$$E(Z,r) = e^{-\alpha/2}\frac{Y}{r^2\sqrt{1+X/r}} + \frac{Q}{r^2\sqrt{1-r_g/r}} = \frac{Y\left(e^{-\alpha/2}-1\right)}{r^2\sqrt{1+X/r}} + \tag{2.78}$$

$$+\frac{Q(X+r_g)}{r^3(\sqrt{1-r_g/r}+\sqrt{1+X/r})\sqrt{1-r_g/r}\sqrt{1+X/r}} + \frac{Y+Q}{r^2\sqrt{1+X/r}}. \tag{2.79}$$

Let us consider the set $\mathbf{S}$ of continuously–differentiable bounded vector-functions $Z(r) = \{X(r), Y(r), \alpha(r), \phi(r)\}$ defined on $[r_{\text{in}}, \infty)$ and equipped with the norm given by

$$\|Z\| \equiv \sup_{r\in[r_{\text{in}},\infty)} \left(|X(r)| + r|\alpha(r)| + |Y(r)| + r|\phi(r)|\right), \tag{2.80}$$

where r_{in} is a sufficiently large value of r.

Let the components of $Z(r)$ satisfy the following estimates for $r \in [r_{\rm in}, \infty)$

$$|X(r)| \le 2r_g, \quad |\alpha(r)| \le 2r_g/r, \quad |Y(r)| \le 2|Q|, \quad |\phi(r)| \le 2|Q|/r, \tag{2.81}$$

Thus, we can replace then the system (2.69, 2.70, 2.75, 2.76) with the conditions (2.73) by the equivalent system of integral equations for the solutions from **S**.

Equations (2.69, 2.70) give us

$$X(r) = -r_g + A_1(Z, r), \tag{2.82}$$

$$A_1(Z, r) \equiv 8\pi \int\limits_r^\infty ds \left[\frac{Y^2(s)}{2s^2} e^{-\alpha(s)} + s^2|\phi(s)|^{2n}\right], \tag{2.83}$$

$$Y(r) = -Q + A_2(Z, r), \tag{2.84}$$

$$A_2(Z, r) \equiv -2n \int\limits_r^\infty ds \, \exp\left[\alpha(s)/2\right] \frac{s^2\phi(s)|\phi(s)|^{2n-2}}{\sqrt{1 + X(s)/s}}. \tag{2.85}$$

And from (2.75, 2.76), we have

$$\alpha(r) = \alpha_0(r) + A_3(Z, r)\,, \quad \alpha_0(r) = \ln(1 - r_g/r), \tag{2.86}$$

$$A_3(Z, r) \equiv -\int\limits_r^\infty D(Z, s) ds, \tag{2.87}$$

$$\phi(r) = \phi_0(r) + A_4(Z, r)\,, \quad \phi_0(r) = \frac{2Q}{r_g}\left[1 - \sqrt{1 - r_g/r}\right]. \tag{2.88}$$

$$A_4(Z, r) \equiv -\int\limits_r^\infty E(Z, s) ds, \tag{2.89}$$

where we specified our integral operators A_i on **S**.

Let us introduce mapping $\mathbf{R} : \mathbf{S} \to \mathbf{S}$, which transforms vector-function Z in the following way

$$Z \to Z' \to \tilde{Z} = \{\tilde{X}(r), \tilde{Y}(r), \tilde{\alpha}(r), \tilde{\phi}(r)\},$$

where

$$\tilde{X}(r) = -r_g + A_1(Z, r), \quad \tilde{Y}(r) = -Q + A_2(Z, r), \tag{2.90}$$

and

$$\tilde{\alpha}(r) = \alpha_0(r) + A_3(Z', r)\,, \quad \tilde{\phi}(r) = \phi_0(r) + A_4(Z', r). \tag{2.91}$$

where $Z' \equiv \{\tilde{X}(r), \alpha(r), \tilde{Y}(r), \phi(r)\}$.

Proposition 1. $\mathbf{R}: \mathbf{S} \to \mathbf{S}$ *that is if* $Z \in \mathbf{S}$ *then* $\tilde{Z} = \mathbf{R}(Z) \in \mathbf{S}$.

Proof. For sufficiently large r the following estimations take place

$$|\tilde{X}(r) + r_g| = |A_1(Z,r)| \leq \frac{C_1}{r}, \quad |\tilde{Y}(r) + Q| = |A_2(Z,r)| \leq \frac{C_3}{r^{2n-4}}, \tag{2.92}$$

where $C_i > 0$ are some constants. We can observe that for sufficiently large r, we have

$$|\tilde{X}(r)| \leq 2r_g, \quad |\tilde{Y}(r)| \leq 2|Q|,$$

which means that $Z' \equiv \{\tilde{X}(r), \alpha(r), \tilde{Y}(r), \phi(r)\} \in \mathbf{S}$.

From (2.81, 2.92), we have

$$|r\tilde{\alpha}(r) + r_g| = |rA_3(Z',r)| \leq \frac{C_4}{r}. \tag{2.93}$$

and

$$|r\tilde{\phi}(r) + Q| = |rA_4(Z',r)| \leq C_5\mu(r), \tag{2.94}$$

where

$$\mu(r) = \left\{ \begin{array}{ll} 1/r, & \text{if } n \geq 3 \\ 1/r^{2n-4}, & \text{if } 2 < n < 3 \end{array} \right\}. \tag{2.95}$$

Thus, for sufficiently large r,

$$|\tilde{\alpha}(r)| < 2r_g/r, \quad |\phi(r)| < 2|Q|/r, \tag{2.96}$$

which means that $\tilde{Z} \equiv \{\tilde{X}(r), \tilde{Y}(r), \tilde{\alpha}(r), \tilde{\phi}(r)\} \in \mathbf{S}$.

Hence, $\tilde{Z} \equiv \mathbf{R}(Z) = \{\tilde{X}(r), \tilde{Y}(r), \tilde{\alpha}(r), \tilde{\phi}(r)\} \in \mathbf{S}$ ■

Proposition 2. *Let* $\mathbf{R}: \mathbf{S} \to \mathbf{S}$ *be an operator defined above. Then* $\mathbf{R}$ *has a contraction mapping property.*

Proof. Let $Z_1 = \{X_1, Y_1, \alpha_1, \phi_1\} \in \mathbf{S}$, $Z_2 = \{X_2, Y_2, \alpha_2, \phi_2\} \in \mathbf{S}$; $\tilde{Z}_1 = \mathbf{R}(Z_1)$, $\tilde{Z}_2 = \mathbf{R}(Z_2)$; $\delta Z \equiv Z_1 - Z_2$.

Using (2.90) and (2.81), we obtain

$$|\delta\tilde{X}(r)| = |A_1(Z_1,r) - A_1(Z_2,r)| \leq \frac{C_7}{r}\|\delta Z\|, \tag{2.97}$$

$$|\delta\tilde{Y}(r)| = |A_2(Z_1,r) - A_2(Z_2,r)| \leq \frac{C_8}{r^{2n-4}}\|\delta Z\|. \tag{2.98}$$

For $D(X,r)$, we have

$$|D(Z_1,s) - D(Z_2,s)| \leq$$
$$\leq \frac{C_9}{s^2}|\delta X(s)| + \frac{C_{10}}{s^3}|\delta Y(s)| + \frac{C_{11}}{s^4}\left(s|\delta\alpha(s)|\right) + \frac{C_{12}}{s^{2n-1}}\left(s|\delta\phi(s)|\right).$$

After substitution $Z_i \to \tilde{Z}_i$, $i = 1, 2$ and taking into account (2.97, 2.98), we have

$$|D(Z_1', s) - D(Z_2', s)| \leq \left\{ \frac{C_9 C_7}{s^3} + \frac{C_{11}}{s^4} + \frac{C_{10} C_8 + C_{12}}{s^{2n-1}} \right\} \|\delta Z\|, \tag{2.99}$$

whence

$$|\delta \tilde{\alpha}(r)| = |A_3(Z_1', r) - A_3(Z_2', r)| \leq \frac{C_{13}}{r^2} \|\delta Z\| \,. \tag{2.100}$$

Similarly,

$$|E(Z_1, s) - E(Z_2, s)| \leq \frac{C_{14}}{s^2} |\delta Y(s)| \left[1 + O\left(\frac{1}{s}\right) \right] + \frac{C_{15}}{s^4} |\delta X(s)| + \frac{C_{16}}{s^2} |\delta \alpha(s)|, \tag{2.101}$$

then

$$|E(Z_1', s) - E(Z_2', s)| \leq \frac{C_{14} C_8}{s^{2n-2}} \|\delta Z\| \left[1 + O\left(\frac{1}{s}\right) \right] + \frac{C_{15}}{s^4} |\delta X(s)| + \frac{C_{16}}{s^3} |s \delta \alpha(s)|), \tag{2.102}$$

$$|\delta \tilde{\phi}(r)| = |A_4(Z_1', r) - A_4(Z_2', r)| \leq \frac{C_{17}}{r} \mu(r) \|\delta Z\|. \tag{2.103}$$

Thus,

$$\|\mathbf{R}(Z_1) - \mathbf{R}(Z_2)\| \leq \max \left[\frac{C_{16}}{r_{\text{in}}}, \frac{C_{17}}{r_{\text{in}}^{2n-4}} \right] \|\delta Z\|. \tag{2.104}$$

Therefore, choosing a sufficiently large r_{in} we obtain that operator $\mathbf{R}$ is contraction mapping. ■

Therefore, the equation $Z = \mathbf{R}(Z)$ has a unique solution.

In order to obtain an asymptotic solutions at spatial infinity, we can use an iteration method with 0-th iteration

$$Z^{(0)} = \{-r_g, -Q, \alpha_0, \phi_0\}.$$

Keeping only main terms, for sufficiently large r, in the first iteration, we get

$$X^{(1)}(r) = -r_g + \frac{4\pi Q^2}{r} \{1 + O[\mu(r)]\} \,, \tag{2.105}$$

$$Y^{(1)}(r) = -Q - \frac{nQ|Q|^{2n-2}}{(n-2) r^{2n-4}} \{1 + O[\mu(r)]\} \,, \tag{2.106}$$

$$\alpha^{(1)}(r) = \alpha_0 + O\left[\frac{\mu(r)}{r^2}\right], \tag{2.107}$$

$$\phi^{(1)}(r) = \frac{Q}{r} \left\{ 1 + \frac{r_g}{2r} + \frac{n|Q|^{2n-2}}{(n-2)(2n-3) r^{2n-4}} \right\} + O\left[\frac{\mu(r)}{r^2}\right], \tag{2.108}$$

where $\mu(r)$ is defined earlier (2.95).

2.6 Numerical solutions with $V(\phi) = w\phi^{2n}$

As an example, we consider a single scalar field ($\Phi = \phi$) with monomial self-interaction potential in the form

$$V(\phi) = w\phi^{2n}, \quad n > 2. \tag{2.109}$$

This self-interaction potential fulfills the conditions (2.3–2.6) so Lemmas 1–4 and Theorem 1 can be applied.

First of all we start with considering of the asymptotic properties of the solutions.

Using the results from section 2.3 for the corresponding explicit form of the self-interaction potential, we can find the next order terms of the asymptotic expansion near singularity $r = 0$.

The scheme of the iteration procedure (2.50–2.53) is the following.

$$\{\chi^{(i-1)}, \phi^{(i-1)}\} \to \{\psi^{(i)}, \gamma^{(i)}\} \to \{\chi^{(i)}, \phi^{(i)}\}, \; i \geq 1.$$

As 0-th iteration for $\chi(r)$ and $\varphi(r)$ we take $\chi^{(0)} = \chi_0$, $\varphi^{(0)} = \phi^0 = -\zeta \ln r$. Then the 1-st iteration has the following form

$$\gamma^{(1)}(r) \simeq \frac{\chi_0}{\eta+1} r^{\eta+1} + \frac{8\pi w \chi_0}{(3+\eta)} r^{\eta+3} [\phi^0]^{2n} \left[1 + O\left(\frac{1}{\ln r}\right)\right], \tag{2.110}$$

$$\psi^{(1)}(r) \simeq -\frac{2nw\chi_0}{\eta+3} r^{\eta+3} [\phi^0]^{2n-1} \left[1 + O\left(\frac{1}{\ln r}\right)\right], \tag{2.111}$$

$$\varphi^{(1)}(r) \simeq \varphi_0 + \frac{\zeta_0 \chi_0}{Y_0(\eta+3)^2} r^{\eta+1} - \begin{cases} \dfrac{8\pi w \zeta_0 \chi_0}{(\eta+3)^2} r^{\eta+3} [\phi^{(0)}(r)]^{2n}, & \text{if } \eta \geq 1, \\ \dfrac{\zeta_0 \chi_0^2}{2Y_0^2(\eta+1)^3} r^{2\eta+2}, & \text{if } 0 < \eta < 1, \end{cases} \tag{2.112}$$

$$\chi^{(1)}(r) \simeq \chi_0 - \frac{8\pi \chi_0^2 \zeta_0^2}{Y_0(\eta+1)^2} r^{\eta+1} + \begin{cases} \dfrac{w}{Y_0} \left(\dfrac{8\pi \chi_0 \zeta_0}{\eta+3}\right)^2 r^{\eta+3} [\phi^{(0)}(r)]^{2n}, & \text{if } \eta \geq 1, \\ -2\pi \left(\dfrac{\zeta_0}{Y_0}\right)^2 \left(\dfrac{\chi_0}{\eta+3}\right)^3 r^{2\eta+2}, & \text{if } 0 < \eta < 1, \end{cases} \tag{2.113}$$

where we have used the asymptotic expansion of the integral

$$\int_0^r x^a [\phi^{(0)}(x)]^b = \frac{r^{a+1}}{a+1} [\phi^{(0)}(r)]^b \left[1 - \frac{b}{a+1} \frac{1}{\ln r} + O\left(\frac{1}{\ln^2 r}\right)\right],$$

for $r \to 0$, and keep only first two main terms.

The asymptotic solutions for $n > 2$ at spatial infinity can be found in the form of inverse power series and the results from section 2.5 are applicable. Here, we write down only the first few terms of the asymptotic solution.

$$\phi(r) = \frac{Q}{r}\left[1 + \frac{r_g}{2r} + \frac{n|Q|^{2n-2}}{(n-2)(2n-3)r^{2n-4}}\right] + O\left[\frac{\mu(r)}{r^2}\right], \tag{2.114}$$

$$e^{\alpha} = \left(1 - \frac{r_g}{r}\right)\left[1 + O\left(\frac{\mu(r)}{r^2}\right)\right], \; e^{-\beta} = \left(1 - \frac{r_g}{r}\right)\left[1 + \frac{4\pi Q^2}{r^2} + O\left(\frac{\mu(r)}{r^2}\right)\right], \tag{2.115}$$

where $\mu(r)$ is defined earlier (2.95), Q is a scalar "charge" and M is the mass of the configuration. They define the corresponding solution uniquely.

The asymptotic solutions near $r = 0$ in general are defined by four arbitrary constants (χ_0, ζ_0, Y_0, ϕ_0), while in the expansion at spatial infinity we have only two arbitrary constants (M, Q). Also, our equations contain two additional parameters, n and w, from the self-interaction potential.

To numerically integrate the Einstein-SF equations (2.12-2.14), we can use asymptotic expansions at either $r \to 0$ or $r \to \infty$ as initial conditions and integrate forward or backward in r, respectively. The second option is more preferable due to the lower number of free parameters (2 vs 4), and rule out necessary to fine-tune parameters in order to achieve the correct asymptotic behavior at spatial infinity. Also in this case we have already shown that corresponding solution convergence and unique.

To obtain the solutions, we start at a sufficiently large initial radius r_∞. Specifically, for $n > 2$ we use $r_\infty = 10^5$, which provides a perfect match between the exact and numeric FJNW solution. We set initial conditions in accordance with the asymptotic relations (2.114, 2.115). We can lower the number of parameters, by re-scaling to eliminate w[1]. Then, we fix (Q, M, n) and integrate backwards from r_∞ to lower values of $r \in (0, r_\infty]$ up to the singularity at $r = 0$. As a result, we obtain a 3-parametric family of solutions described by M, Q, and n.

The typical examples of solutions are shown in Figs. 2.2-2.4 for different values of (M, Q, n). The qualitative properties of the metric functions and scalar field are rather similar for different values of parameters (M, Q, n): $e^{\alpha(r)}$ is a monotonically increasing function bounded from above ($e^{\alpha(r)} \leq 1$) and $e^{\beta(r)}$ has a maximum at some point $r = r_{\max}(M, Q, n)$. Also, one can see that $e^{\alpha} \gg e^{\beta}$ for $r \to 0$ which is in accordance with (2.45).

The SF is always a monotonically decreasing function and $\phi \to 0$ for $r \to \infty$. For large n and fixed M, Q, the solutions approach the FJNW solution, except for a small region near the singularity, where $|\phi(r)| > 1$.

[1] $r = r/\sqrt{w}$

One of interesting question pertains to the relationship between the parameters (χ_0, ζ_0, Y_0, ϕ_0) and (M, Q). To illustrate this relationship, we have plotted the typical dependencies of these parameters against (M, Q) for different values of n, Q, and M in Figs. 2.5-2.9. They reveal that the dependencies of (χ_0, ζ_0, Y_0, ϕ_0) on (M, Q) exhibit non-monotonic and non-unique behavior.

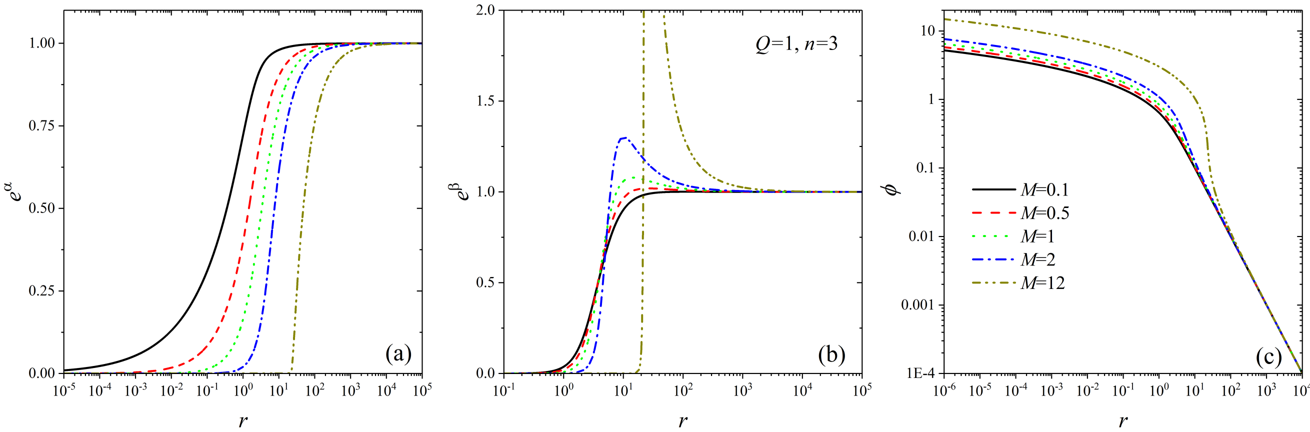

Figure 2.2: The typical behaviour of the metric functions and scalar field for $Q = 1, n = 3$ and different values of M.

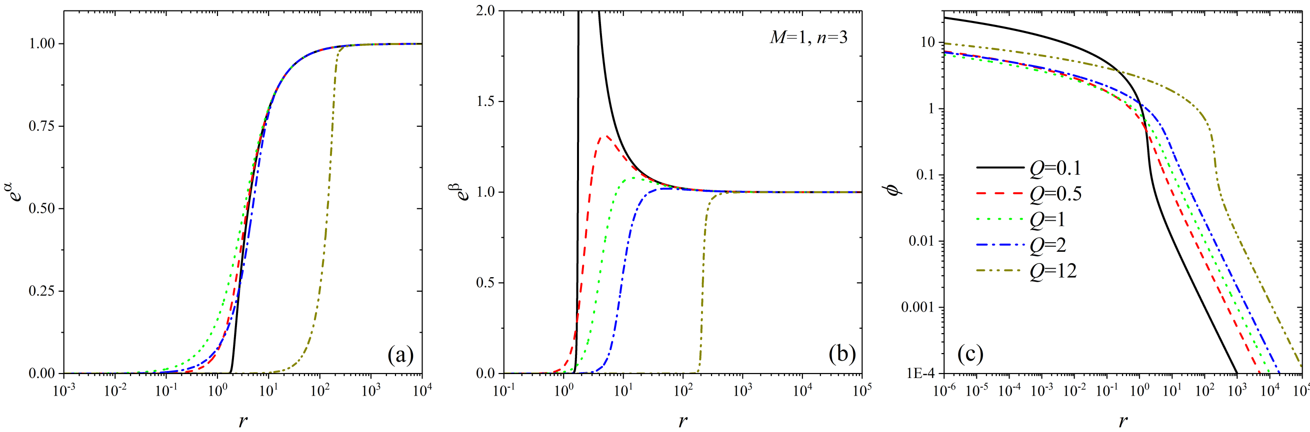

Figure 2.3: The typical behaviour of the metric functions and scalar field for $M = 1, n = 3$ and different values of Q.

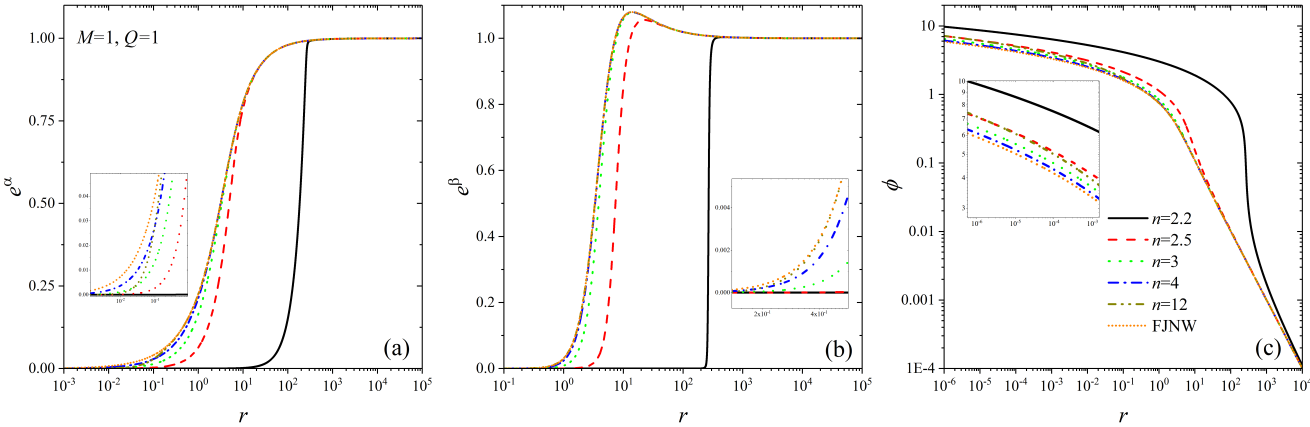

Figure 2.4: The typical behaviour of the metric functions and scalar field for $M = 1, Q = 1$ and different values of n. The small pictures illustrate behavior of the corresponding functions in the domain of small values of r.

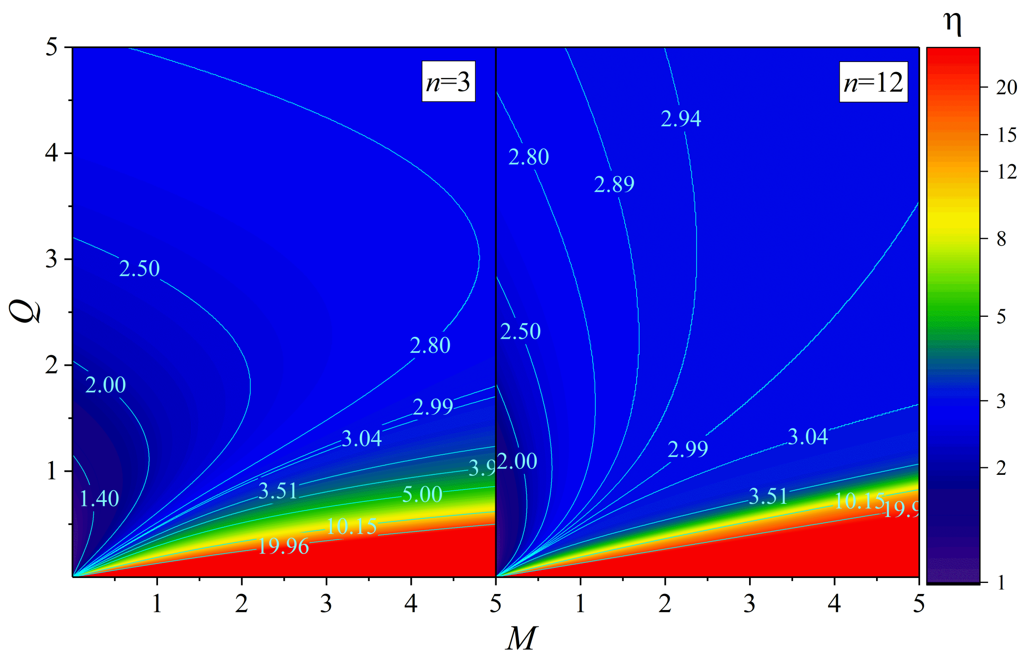

Figure 2.5: The contour plot of $\eta(M, Q)$ for $n = 3$ (left panel) and $n = 12$ (right panel). It can be observed that as Q approaches zero, η tends to infinity. For all values of (M, Q, n) that were studied, it was found that $\eta > 1$. The case where $\eta = 3$ is critical. The corresponding dependencies are non-monotonic for $\eta < 3$, and monotonic for $\eta > 3$. Increasing the value of n leads to η being closer to 3.

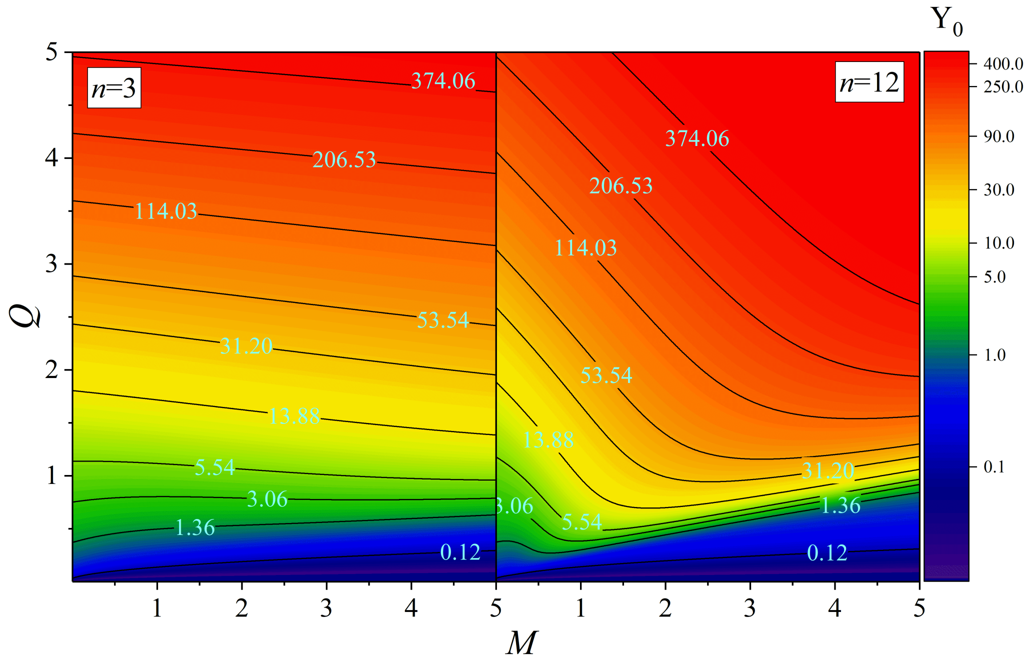

Figure 2.6: The contour plot of $Y_0(M,Q)$ for $n = 3$ (left panel) and $n = 12$ (right panel) is shown in the figure. It can be observed that as Q approaches zero, Y_0 tends to zero. Increasing the value of n leads to non-monotonic behavior of $Y_0(M,Q)$.

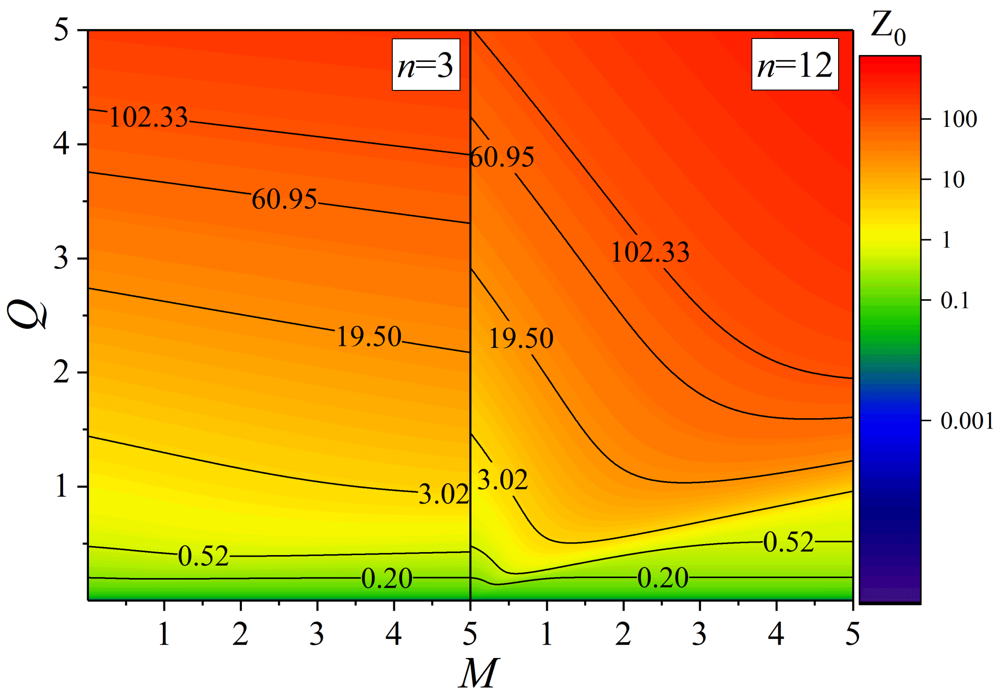

Figure 2.7: The contour plot of $Z_0(M,Q)$ for $n = 3$ (left panel) and $n = 12$ (right panel) is shown in the figure. It can be observed that as Q approaches zero, Z_0 tends to zero. Increasing the value of n leads to non-monotonic behavior of $Z_0(M,Q)$.

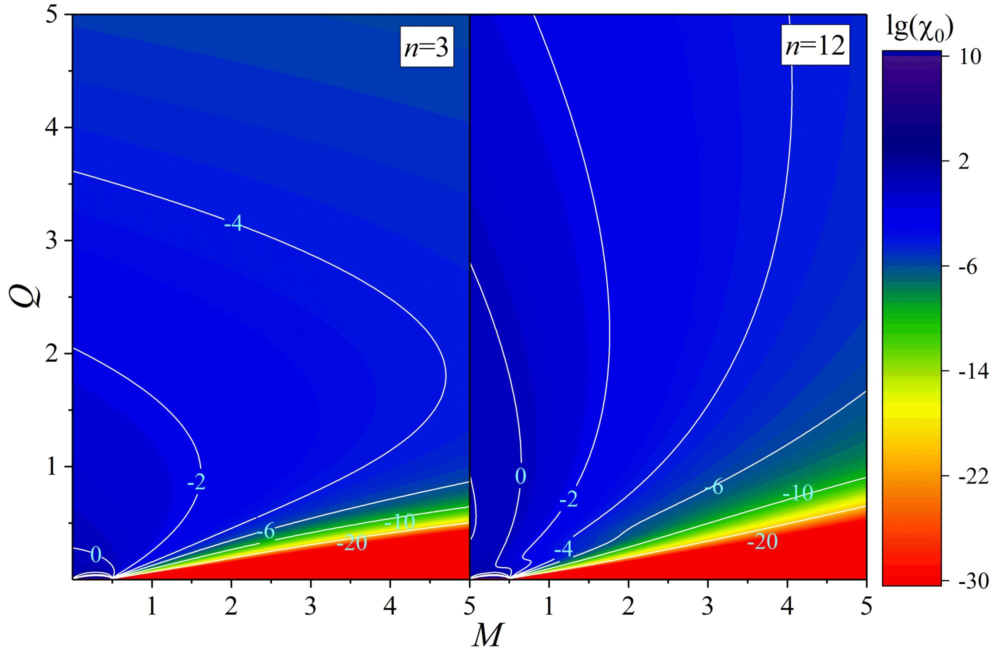

Figure 2.8: The contour plot of $\lg(\chi_0(M,Q))$ for $n = 3$ (left panel) and $n = 12$ (right panel) is shown in the figure. It can be observed that in a small domain near zero, χ_0 becomes large as $Q \to 0$. On the other hand, for $M > M_{cr}$, χ_0 tends to zero as $Q \to 0$.

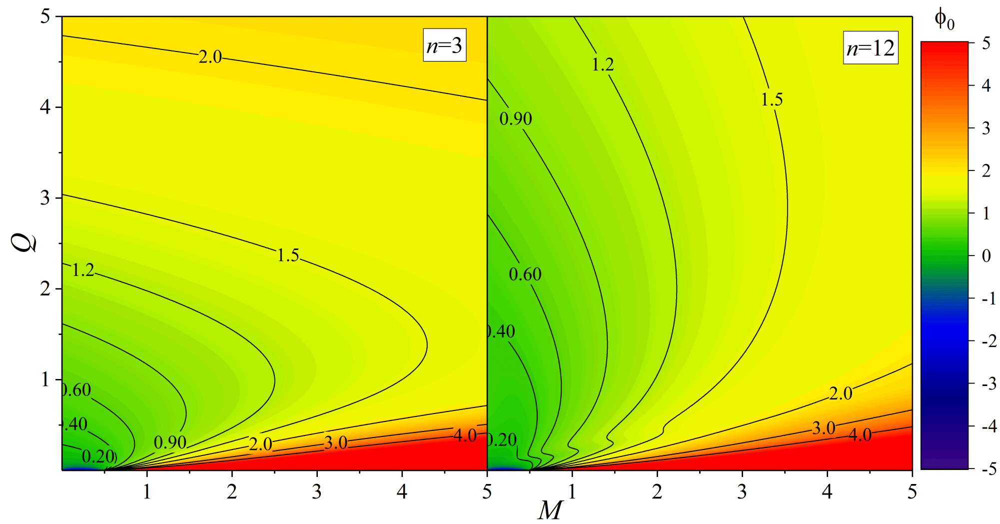

Figure 2.9: The contour plot of $\phi_0(M,Q)$ for $n = 3$ (left panel) and $n = 12$ (right panel) is shown in the figure. It can be observed that in a small domain near zero, $\phi_0 < 0$. On the other hand, for $M > M_{cr}$, $\phi_0 \to \infty$ as $Q \to 0$.

Chapter 3

Spherical singularities

One typical phenomenon in the theory of nonlinear equations is the emergence of singularities in solutions of differential equations. It's evident that the Einstein-SF equations are nonlinear. In Chapter 2, we proved that, under certain conditions on the self-interaction potential $V(\phi)$, the corresponding solutions will be regular up to $r = 0$.

It is interesting to investigate what might occur if we violate some of the conditions of Theorem 1.

3.1 Spherical singularities in Minkowski space-time

First of all, let us consider the appearance of spherical singularities at a finite value of r in the case of flat space for the self-interaction potential $V(\phi) = w\phi^p$.

The Klein-Gordon equation in the flat space has the following form

$$\frac{d}{dr}\left[r^2\frac{d\phi}{dr}\right] = pwr^2\phi|\phi|^{p-2}, \tag{3.1}$$

One can see, that for $p > 2$, equation (3.1) admits a singular solution at some point $r = r_s > 0$, which has the following asymptotic behaviour near $r = r_s$

$$\phi(r) \approx \left[\frac{q(q+1)}{pw(r-r_s)^2}\right]^{q/2}, \quad q = 2/(p-2), \quad r_s > 0. \tag{3.2}$$

We don't know anything about the asymptotic behavior of such solutions at spatial infinity. Now we will consider an example with $p = 2n$, where $n > 2$.

We can transform (3.1) as

$$\frac{dE}{dr} = -\frac{2}{r}[\phi'(r)]^2 \leq 0, \quad E(r) = [\phi'(r)]^2/2 - w\phi^{2n}. \tag{3.3}$$

Let r_0 is a sufficiently large value r such that

$$\phi(r_0) \approx Q/r_0 \ll 1, \quad \phi'(r) \approx -Q/r_0^2. \tag{3.4}$$

Then, for $r < r_0$, one can see that $E(r) \geq E(r_0)$. And for $r = r_0$, we obtain $E(r_0) > 0$ or

$$[\phi'(r)]^2 > 2w\phi^{2n}(r). \tag{3.5}$$

Hence,

$$\phi'(r) < -\sqrt{2w}\phi^n, \tag{3.6}$$

$$\frac{d}{dr}\left(\frac{1}{\phi^{n-1}}\right) > \sqrt{2w}(n-1), \tag{3.7}$$

where we assumed that ϕ is a positive and monotonically decreasing function. For $r \in [r, r_0]$, from the inequality (3.7), we have

$$\phi(r) > \left[\phi_0^{-(n-1)} - \sqrt{2w}(n-1)(r_0 - r)\right]^{1/(n-1)}, \ \phi(r_0) = \phi_0. \tag{3.8}$$

If

$$\phi_0^{-(n-1)} - \sqrt{2w}(n-1)r_0 = 0, \tag{3.9}$$

then it implies that $\phi \to \infty$ for $r \to r_s$.

For sufficiently large r_0, both estimations will hold if

$$Q > r_0^{(n-2)/(n-1)}[\sqrt{2w}(n-1)]^{-1/(n-1)}. \tag{3.10}$$

This guarantees the presence of a singularity for some certain $r = r_s$.

To illustrate this, we perform numerical integration of equation (3.1) for $p = 2n$, $n > 2$ and $w = 1$ with initial conditions given by (3.4) for a different values of Q and n, with $r_0 = 10^5$. The results are shown in Fig. 3.1. We can see that the singularity occurs for lower values of Q then predicted by (3.10).

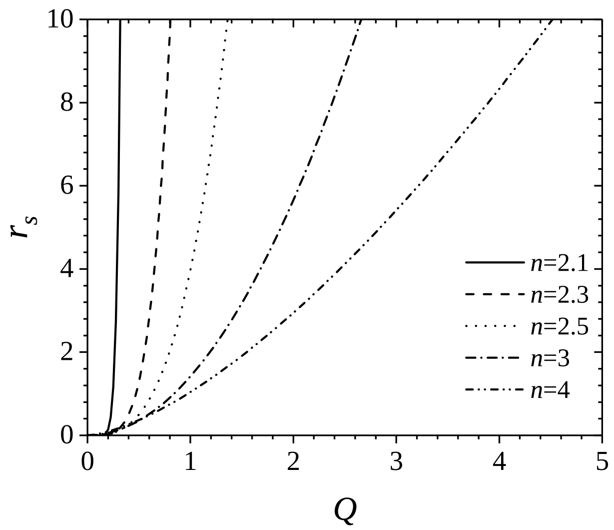

Figure 3.1: The radii r_s of the singularities for different $p = 2n$ as a functions of Q.

3.2 Example of SS in general case for exponentially unbounded potentials

In Chapter 2, we proved that if the self-interaction potential $V(\phi)$ satisfies the following conditions:

$$V(\phi) \geq 0,\ \ \phi_i V_i'(\phi) \geq 0,\ \ |V(\phi)| < C_0 \exp(\kappa\phi),$$

then the corresponding solutions of the Einstein-SF equations are regular on the interval $r \in (0, \infty)$.

It is interesting to consider what happens if we violate the exponential boundedness assumption. For example, let us consider the following self-interaction potential

$$V(\phi) = w \sinh\left(\kappa\phi^{2n}\right). \tag{3.11}$$

It is evident, that the condition $|V(\phi)| < C_0 \exp(\kappa\phi)$ is not satisfied, so for $n \geq 1$, it can be expected that the solutions may demonstrate the singular behavior at some finite $r = r_s > 0$.

As in the previous considerations, we are interested in asymptotically static asymptotically flat spherically symmetric configurations with the asymptotic conditions given by (2.15). From Lemma 1, we already know that the functions $\phi(r)$ and $\phi'(r)$ do not change their signs. Then, without loss of generality, we fix them as $\phi(r) > 0$ and $\phi'(r) < 0$ on $r \in (0, \infty)$.

In this subsection, we focus on the singularities that can occur at some non-zero $r = r_s$ for the potential given by (3.11), i.e. we seek solutions on the interval (r_s, ∞), such that

$$\phi'(r) \to -\infty \quad \text{as} \quad r \to r_s + 0. \tag{3.12}$$

We don't know how to find the full exact solution but at least we can estimate his asymptotic behavior near the singularity.

Starting from the Einstein-SF equations (2.12) and (2.13), we obtain the following expression for $\beta'(r)$

$$\beta'(r) = 4\pi r \phi'(r)^2 + \frac{1}{r}\left(1 - e^{\beta(r)}\right) + 8\pi r e^{\beta(r)} V(\phi(r)). \tag{3.13}$$

For simplicity, we fix $\kappa = w = 1$. Our numerical estimations near $r = r_s$ show that $\alpha(r)$ is asymptotically less than $\beta(r)$ and $\phi(r)$. Hence, in the first approximation, we can neglect terms with $\alpha(r)$. Next, here and after we consider the leading terms of (2.14) in the small enough vicinity of $r = r_s$.

The Klein-Gordon equation has the following form in the vicinity of the singularity

$$e^{-\beta/2}\frac{d}{dr}\left[e^{-\beta/2}\phi'\right] \simeq V'(\phi). \tag{3.14}$$

It can be rewritten as $e^{-\beta}\phi'^2 \simeq 2V(\phi) + \text{const} \simeq 2V(\phi)$. Thus, we have

$$e^{-\beta}\phi'^2 \simeq 2V(\phi). \tag{3.15}$$

Hence, $e^{\beta}V(\phi) \simeq \phi'^2 \to \infty$, which means that both sides tend to infinity for $r \to r_s + 0$. After substitution (3.15) into (3.13) and saving only the main terms, we obtain

$$\beta' \simeq 16\pi r e^{\beta} V(\phi), \tag{3.16}$$

For $r \in (r_s, r_1]$, where r_1 is sufficiently small, we can observe that $\beta(r)$ is monotonically increasing function. For $r \to r_s + 0$, from (3.16) we obtain

$$\frac{d}{dr}\left[e^{-\beta/2}\right] \approx -8\pi r_s e^{\beta/2} V(\phi). \tag{3.17}$$

From (3.15), we have

$$\phi' \approx -\sqrt{2} e^{\beta/2}\sqrt{V(\phi)}, \tag{3.18}$$

where we took into account that $\phi(r)$ is a positive monotonically decreasing function. After combining equations (3.17, 3.18), we get

$$\frac{d}{d\phi}\left[e^{-\beta/2}\right] = \frac{8\pi r_s}{\sqrt{2}}\sqrt{V(\phi)}, \tag{3.19}$$

which can be easily integrated near r_s. The leading terms for $r \to r_s + 0$

$$e^{-\beta(r)/2} \simeq \frac{8\pi r_s}{\sqrt{2}}\Phi(\phi) + e^{-\beta(r_1)/2} \simeq \frac{8\pi r_s}{\sqrt{2}}\Phi(\phi), \tag{3.20}$$

where we denoted

$$\Phi(\phi) = \int_{\phi(r_1)}^{\phi} \sqrt{V(x)}dx = \frac{1}{\sqrt{2}} \int_{\phi(r_1)}^{\phi} \exp\left(\frac{1}{2}x^{2n}\right) dx.$$

The corresponding integral can be represented as the difference of two incomplete gamma functions.

$$\Phi(\phi) = \frac{(-1)^{\frac{1}{2n}}}{2^{\frac{3n-1}{2n}} n} \left(\Gamma\left[\frac{1}{2n}, -\frac{1}{2}\phi^{2n}\right] - \Gamma\left[\frac{1}{2n}, -\frac{1}{2}\phi_1^{2n}\right]\right).$$

Near singularity $r \to r_s + 0$ it can be expressed as

$$\Phi(\phi) = \frac{\sqrt{2V(\phi)}}{n\phi^{2n-1}} \left[1 + \sum_{j=1}^{\infty} \prod_{k=1}^{j} \frac{(-1)^{k+j} 2^{j-k}}{n^k} \frac{(2nk-1)}{\phi^{2nj}}\right], \tag{3.21}$$

Then taking into account only the leading term in (3.21) and using (3.18, 3.20), we have the following equation

$$\frac{d\phi}{dr} = -\frac{\sqrt{V(\phi)}}{4\pi r_s \Phi(\phi)} \simeq -\frac{n}{4\pi r_s}\phi^{2n-1}. \tag{3.22}$$

which has the following solution

$$\phi(r) = \left\{\frac{n(n-1)}{2\pi}\frac{r - r_1}{r_s} + \frac{1}{\phi_1^{2(n-1)}}\right\}^{-\frac{1}{2(n-1)}}.$$

where $\phi_1 = \phi(r_1)$ is some constant. One can see that the condition (3.12) can be satisfied if

$$\frac{n(n-1)}{2\pi} \cdot \frac{r_1 - r_s}{r_s} = \frac{1}{\phi_1^{2(n-1)}}. \tag{3.23}$$

Thus

$$\phi(r) \sim \frac{A^{\Delta}}{(r - r_s)^{\Delta}}, \quad A = \frac{2\pi r_s}{n(n-1)}, \quad \Delta = \frac{1}{2(n-1)}. \tag{3.24}$$

Using (3.20), we obtain the corresponding asymptotic behaviour for $\beta(r)$

$$\beta(r) \sim -2\ln\Phi(\phi) \sim -\frac{A^{1+2\Delta}}{(r - r_s)^{1+2\Delta}}. \tag{3.25}$$

We can also estimate the asymptotic behaviour of the Kretschmann invariant near such singularity at r_s. We have

$$R_{\alpha\beta\gamma\delta}R^{\alpha\beta\gamma\delta} \sim \frac{e^{-2\beta(r)}}{(r - r_s)^{4(1+\Delta)}}. \tag{3.26}$$

Also, the photons from a distant observer at some $r = r_0 < \infty$ can reach the singularity at r_s in a finite time, and vice versa For the radial photons, one can see that time

$$T = \int\limits_{r_s}^{r_0} e^{\frac{1}{2}(\beta-\alpha)} dr < \infty,$$

is finite, because $e^{(\beta-\alpha)/2}$ is a bounded function and tends to 0 for $r \to r_s$. Hence, the integral converges at r_s.

Therefore, this is a naked singularity.

3.3 Numerical solutions with $V(\phi) = w \sinh\left(\kappa\phi^{2n}\right)$

In this section, we numerically check the analytical approximation presented in the previous section.

At spatial infinity, the self-interaction potential $V(\phi) \sim w\kappa\phi^{2n}$. Which means that we have the same asymptotic solutions (2.114, 2.115), and the results of Chapter 2.5 remain valid.

To reduce the number of free parameters, we can rescale the variables in the following way $r \to r/\sqrt{Gw}$, $\phi \to \phi/\sqrt{G}$, $\kappa \to G^n\kappa$. Then we can fix $w = 1$, and our configuration is now describes only by four arbitrary constants: Q, M, n, and κ.

We can use (2.114, 2.115) as initial conditions and integrate backward in r towards to singularity. To get more numerical stable results, we assume that the spherical singularity is located at a point, where the value of the Kretschmann invariant is $R_{\mu\nu\sigma\delta}R^{\mu\nu\sigma\delta} = 10^{35}$.

The typical behavior of the solutions and the Kretschmann invariant is shown in Figs. 3.2. As predicted, the Kretschmann invariant tends to infinity and $e^\beta \to 0$, $e^\alpha \to e^{\alpha_0}$ for $r \to r_s{+}0$. Far away from the singularity, the behavior of the solutions is qualitatively similar to the behaviour of solutions from Chapter 2.6. e^α is a monotonically increasing and bounded function, with $e^{\alpha(r)} \leq 1$, while $e^{\beta(r)}$ reaches a maximum at some point $r = r_{\max}(M, Q, n, \kappa)$ and then decreases to 1 for $r \to \infty$.

The dependencies of the singularity radii values r_s are non-trivial, and some examples are shown in Figs. 3.3-3.5.

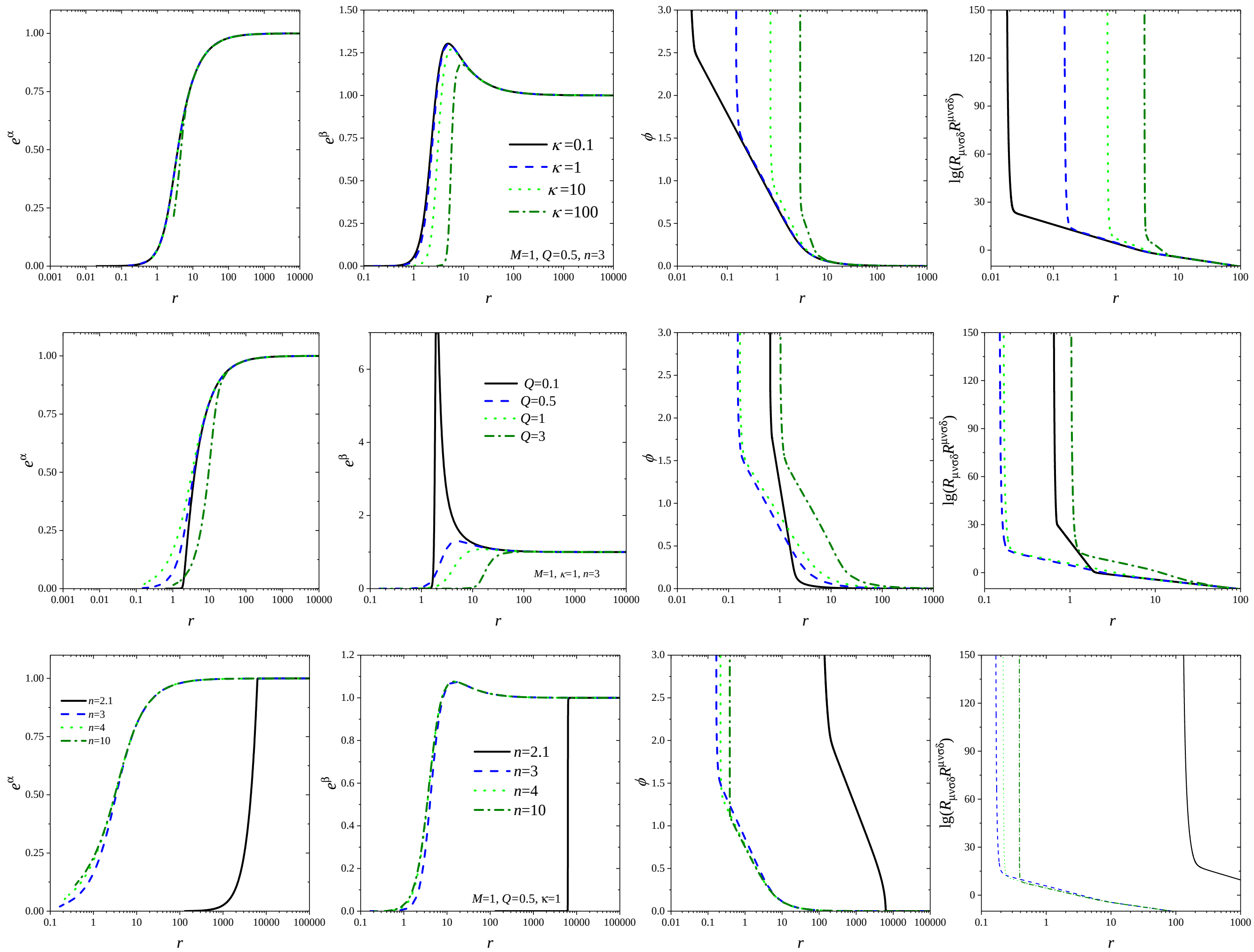

Figure 3.2: The typical behavior of the metric functions e^{α}, e^{β}, ϕ, and the Kretschmann invariant for different parameter configurations

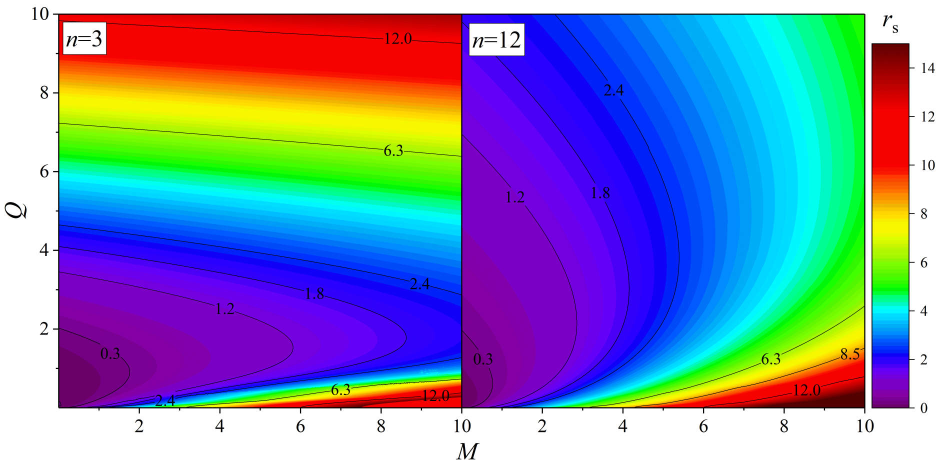

Figure 3.3: The typical dependencies of the radii of the spherical singularities for different M, Q, and $\kappa = 1$.

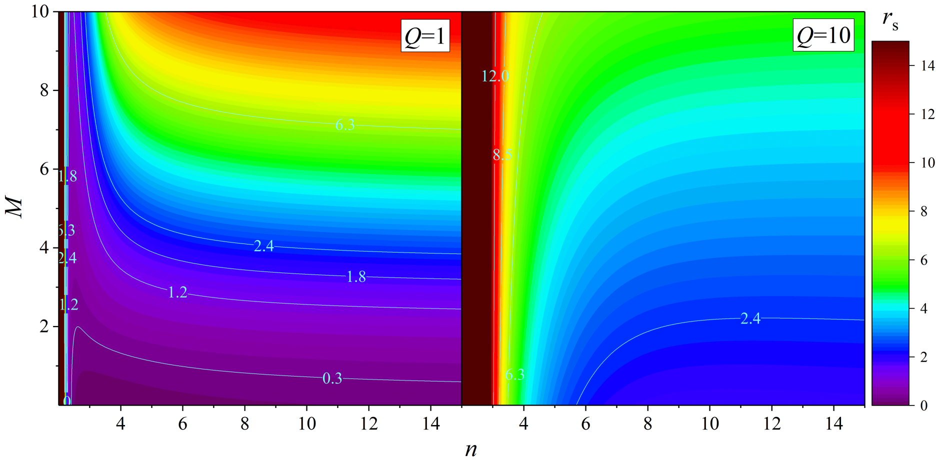

Figure 3.4: The typical dependencies of the radii of the spherical singularities for different n, M, $\kappa = 1$.

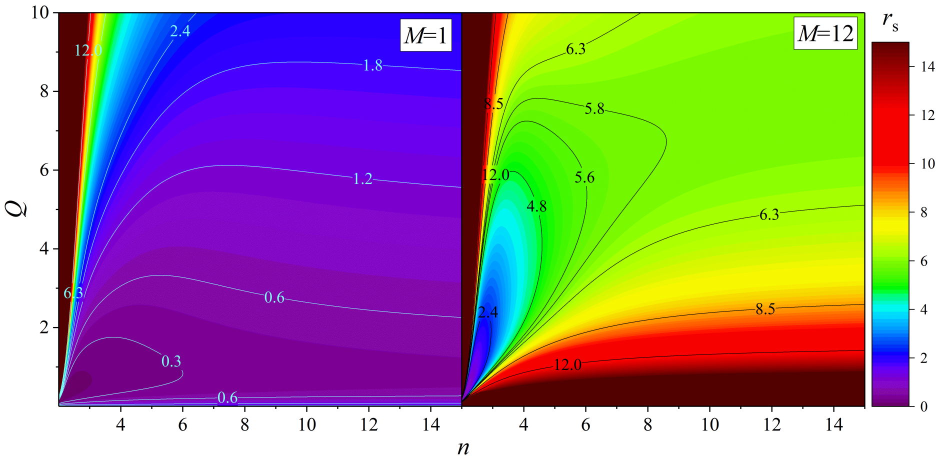

Figure 3.5: The typical dependencies of the radii of the spherical singularities for different n, Q, $\kappa = 1$.

Chapter 4

Some exact solutions of Einstein-scalar field equations

4.1 Generalized Fisher/JNW solution with N free scalar fields

In this section, we obtain generalization of the FJNW solution in the case of N scalar fields with $V(\Phi) = 0$. Solution with $N = 1$ was previously obtained by Fisher [17] in curvature coordinates and by Janis, Newman, Winicour [106] in quasi-global coordinates.

From (2.24), one can see that Z_i is constant, and then using equations (2.22) and (2.23), we can separate the variables and obtain the following equation

$$\frac{d^2Y}{dr^2} = \frac{\Xi}{rY^2}\frac{dY}{dr}, \tag{4.1}$$

where constant Ξ is defined as

$$\Xi = 4\pi \sum_{i=1}^{N} Z_i^2 = const. \tag{4.2}$$

We can transform equation (4.1) into an autonomous equation by substitution $r = \exp(t)$ and then integrate it. As result, we obtain

$$\frac{dY}{dt} = Y - \frac{\Xi}{Y} + A\,, \tag{4.3}$$

where $A = r_g = 2M$ is an integration constant.

Finally,

$$[g_-(Y)]^{(1-\nu)/2}\,[g_+(Y)]^{(1+\nu)/2} = r\,, \tag{4.4}$$

where $g_\pm(Y) = Y + M \pm \sqrt{M^2+\Xi}$, $\nu = M/\sqrt{M^2+\Xi}$. One can see that $Y(r) \in [\sqrt{M^2+\Xi} - M, \infty)$ for $r \in (0,\infty)$.

The metric components have the following form in terms of $g_\pm(Y)$

$$e^\alpha = (g_-/g_+)^\nu, \quad e^\beta = g_+g_-/Y^2, \tag{4.5}$$

and for the scalar field $\phi_i(Y)$, we have

$$\phi_i(Y) = \frac{Z_i}{2\sqrt{M^2+\Xi}}\ln\left(\frac{g_+(Y)}{g_-(Y)}\right). \tag{4.6}$$

One can see that we re-obtain the well-know Fisher solution [17], but with a small difference, we have N scalar fields in (4.2) and (4.6).

If we change to a new radial variable Y, we re-obtain the Janis-Newman-Winicour representation of the Fisher solution in quasi-global coordinates [106, 108].

$$ds^2 = \left(\frac{g_-}{g_+}\right)^\nu dt^2 - \left(\frac{g_+}{g_-}\right)^\nu dY^2 - (g_+)^{1+\nu}(g_-)^{1-\nu}dO^2. \tag{4.7}$$

4.2 Special exact solutions with non-monotonic self-interaction

In this Section we generate a "toy model" family of exact solutions that comprise black holes and naked singularities. To do this we use the "inverse" approach [119, 122, 124]. We can postulate a form for one of the metric functions and then find all other components of the metric and energy-momentum tensor.

4.2.1 Basic relations

The metric for a static spherically symmetric space-time in quasi-global coordinates has the following form

$$ds^2 = A(x)dt^2 - B(x)dx^2 - R^2(x)\left[d\theta^2 + \sin^2(\theta)d\varphi^2\right], \tag{4.8}$$

Due to spherical symmetry we can fix one of metric function in arbitrary way. For our purposes, it is convenient to put $B = 1/A$, then

$$ds^2 = A(x)dt^2 - \frac{dx^2}{A(x)} - R^2(x)\left[d\theta^2 + \sin^2(\theta)d\varphi^2\right]. \tag{4.9}$$

We say that x_0 is the point of center, if $R(x_0) = 0$ (i.e. point, where the radii of the 2D spheres approaches 0). Also, we suggest that $R(x) > 0$ for $x > x_0$.

We assume that $A(x)$, $R(x) \in C^{(2)}$, $\phi \in C^{(1)}$ with the following asymptotic behavior

$$R(x) = x + o(1/x), \quad R'(x) = 1 + o(1/x), \tag{4.10}$$

and

$$A(x) = 1 - 2M/x + o(1/x),\ M > 0,\ \phi \to 0. \tag{4.11}$$

as $x \to \infty$.

The Einstein equations have the following form [122, 124]

$$\frac{d}{dx}\left(\frac{dA}{dx}R^2\right) = -2R^2V(\phi), \tag{4.12}$$

$$\frac{d^2R}{dx^2} + \frac{1}{2}R\left(\frac{d\phi}{dx}\right)^2 = 0, \tag{4.13}$$

$$A\frac{d^2R^2}{dx^2} - R^2\frac{d^2A}{dx^2} = 2. \tag{4.14}$$

We do not consider Klein-Gordon equation for the scalar field, because it is not independent from the equations (4.12—4.14). Equation (4.14) can be written as

$$\frac{d}{dx}\left[R^4\frac{d}{dx}\left(\frac{A}{R^2}\right)\right] = -2.$$

Using (4.10,4.12, 4.13), we obtain

$$A(x) = R^2(x)\int_x^\infty \frac{2x' - C}{R^4(x')}dx', \quad \phi(x) = \pm\int_x^\infty \sqrt{-\frac{2}{R(y)}\frac{d^2R(y)}{dy^2}}dy. \tag{4.15}$$

where $C = 6M$ is an integration constant.

Then, using (4.12), we can represent the potential $V(x)$ as $V(\phi(x))$ in terms of $R(x)$.

$$V(x) = \frac{1}{R^2} - \frac{A}{R^2}\left(3\left(R'\right)^2 + RR''\right) + 2\frac{x - 3M}{R^3}\frac{dR}{dx}. \tag{4.16}$$

Equations (4.15-4.16) provide a general solution in an implicit form for any arbitrary $R(x)$ that satisfies (4.10, 4.11).

Further, we will use results of [124] for the asymptotical behaviour of solutions near the center. Let $R(x)$ is sufficiently-differentiable function and the conditions (4.10, 4.11) are fulfilled. Then we can employ the Taylor expansion in the vicinity of x_0 and obtain the asymptotic relations in a general case. We have [124]

$$A(x) \sim \frac{2(x_0 - 3M)}{3R'(x_0)\,R(x)}, \quad V(x) \sim \frac{(x_0 - 3M)\,R''(x_0)}{3R'(x_0)\,R^2(x)}; \tag{4.17}$$

One can observe that there are two basic variants in dependence on the sign $x_0 - 3M$ [124].

(a) Let $x_0 \geq 3M$, then $A(x) > 0$ for $x > x_0$ and $A(x) \to \infty$ for $x \to x_0 + 0$. The Kretschmann invariant near x_0 for $x_0 \neq 3M$ has the following behaviour

$$R_{\alpha\beta\gamma\delta}R^{\alpha\beta\gamma\delta} \sim \frac{16(x_0 - 3M)^2}{3[R'(x_0)]^4(x - x_0)^6}, \tag{4.18}$$

and for $x_0 = 3M$ and $R''(x_0) \neq 0$, we have

$$R_{\alpha\beta\gamma\delta}R^{\alpha\beta\gamma\delta} \sim \frac{24[R''(x_0)]^2}{[R'(x_0)]^6(x - x_0)^2}. \tag{4.19}$$

For the radial photons, the time T needed for signal emitted from the center x_0 to reach an distant observer at some $x_1 \in (x_0, \infty)$ and vice versa is

$$T = \int_{x_0}^{x_1} \frac{dx}{A(x)} < \int_{x_0}^{x_1} \frac{dx}{K} = \frac{1}{K}(x_1 - x_0) < \infty, \tag{4.20}$$

where we took into account that $A(x) \to \infty$ for $x \to x_0$, $A(x) \to 1$ as $x \to \infty$, and $A(x) > 0$ for all x, then there exists a constant $K > 0$ such that $A(x) \geq K$ for all x.

Hence, we deal with a naked singularity.

(b) Let $x_0 < 3M$, then $A(x) \to -\infty$ for $x \to x_0 + 0$ and $A(x) \to 1$ for $x \to \infty$ then there exist a point $x_h > x_0$ such that $A(x_h) = 0$ and $A(x) > 0$, $r(x) > 0$ for all $x > x_h$. We don't have any singularities of the metric functions, scalar field and curvature invariants at $x = x_h$. We have a usual the Schwarzschild-like singularity at $x = x_h$ that can be removed by a coordinate transformation, e.g.,

$$(t, x) \to (T, X) : T = t + \int dx A^{-1}(1 - A)^{1/2},\ X = t + \int dx A^{-1}(1 - A)^{-1/2}.$$

In these new coordinates the 2-dimensional surface $x = x_h$ is light-like. Therefore, this is the regular horizon and in this case we deal with a black hole.

4.2.2 Family of special solutions

Let us take the $R(x)$ in the following form

$$R(x) = x + \rho(x), \quad \rho(x) \to 0 \ \text{for}\, x \to \infty. \tag{4.21}$$

We can assume that SF can be represented as expansion in powers of $1/x$, given by

$$\phi(x) = \frac{A_0}{x^p}\left[1 + \sum_{n=1}^{\infty} A_n x^{-n}\right], \quad p > 1. \tag{4.22}$$

This leads to a series expansion for $\rho(x)$ in the following form

$$\rho(x) = \frac{1}{x^{2p-1}} \sum_{m=0}^{\infty} \frac{B_{n,m}}{x^m}. \tag{4.23}$$

Then, the leading term of $\rho(x)$ is

$$\rho(x) = x - \frac{A_0^2 p}{4(2p-1)x^{2p-1}}. \tag{4.24}$$

If we denote $2p = N$ and $x_0 = \left[\frac{A_0^2 p}{4(2p-1)}\right]^{1/N}$, then $R(x)$ can be written as

$$R(x) = x\left[1 - \left(\frac{x_0}{x}\right)^N\right], \quad N > 2, \tag{4.25}$$

where N, x_0 are some positive constants.

One can see that, for $x > x_0$ we have $R(x) > 0$, $R''(x) < 0$ and the conditions (4.10, 4.11) are fulfilled. Integral in (4.15) for $x > x_0$ gives us the explicit form of $A(x)$

$$A(x) = \left[1 - \left(\frac{x_0}{x}\right)^N\right]^2 G(x, x_0, N), \tag{4.26}$$

where we denoted

$$G(x, x_0, N) \equiv {}_2F_1\left[4, \frac{2}{N}, 1 + \frac{2}{N}, \left(\frac{x_0}{x}\right)^N\right] - \frac{2M}{x} {}_2F_1\left[4, \frac{3}{N}, 1 + \frac{3}{N}, \left(\frac{x_0}{x}\right)^N\right].$$

From (4.15), we have

$$\phi(x) = \pm\sqrt{\frac{8(N-1)}{N}} \arcsin\left[\left(\frac{x_0}{x}\right)^{N/2}\right]. \tag{4.27}$$

Thus, the formulas (4.16, 4.26, 4.27) define the self-interaction potential $V(\phi)$ for the scalar field. It can be seen that the scalar field is bounded from above and can only take values in the range $|\phi| \in (0, \pi\sqrt{2}]$, the self-interaction potential is defined for $|\phi| < (\pi/2)\sqrt{8(N-1)/N}$.

Using the statements (a) and (b) from Section 4.2.1, we immidiately obtain that for $x_0 \geq 3M$ we have a naked singularity and for $x_0 < 3M$, a black hole with a horizon located at some $x_h > x_0$, respectively.

The asymptotic behaviour near singularity is

$$A(x) \sim \frac{2(x_0 - 3M)}{3N^2(x - x_0)}, \quad V(x) \sim -\frac{(N-1)(x_0 - 3M)}{3N^2 x_0 (x - x_0)^2}, \tag{4.28}$$

for $x_0 > 3M$ and

$$A(x) \sim \frac{1}{N^2}, \quad V(x) \sim -\frac{6(N-1)}{N^2 x_0 (x - x_0)}. \tag{4.29}$$

for $x_0 = 3M$.
Asymptotic behaviour at spatial infinity can be obtained by expanding in powers of $1/x$

$$A(x) = 1 - \frac{2m}{x} + \frac{2(2-N)}{N+2}\left(\frac{x_0}{x}\right)^N \left[1 + O\left(\frac{1}{x}\right)\right], \tag{4.30}$$

$$V(x) = \frac{N(N-1)(N-2)}{N+2}\frac{x_0^N}{x^{N+2}}\left[1 + O\left(\frac{1}{x}\right)\right]. \tag{4.31}$$

The asymptotic behavior of $V(\phi)$ near $\phi = 0$ is

$$V(\phi) \sim \frac{(N-2)N^{2(1+1/N)}}{(N-1)^{2/N}(N+2)\, x_0^2}\left(\frac{|\phi|}{2\sqrt{2}}\right)^{2(1+2/N)}, \tag{4.32}$$

which is similar in the both considering cases.

One can see that $d^2V/d\phi^2 = 0$, which means that we are dealing with the nonlinear massless scalar field.

The typical form of the corresponding solutions (4.25–4.27) are presented in Figs. 4.1–4.4 for various values of (x_0, N). For this figures we have used the curvature coordinates in order to compare behaviour of the obtained solutions with the results of Chapters 2.6, 3.3. Specifically, we put $e^\alpha = A(x)$, $e^{-\beta} = (R')^2 A(x)$, $R(x) = y$, the point of center at x_0 is shifted to $y = 0$.

The solutions exhibit different behavior in both the BH and NS cases, as illustrated in Figs. 4.1, 4.2. In the BH case, e^α is a monotonically increasing function, with $e^\alpha \in [0, 1)$ for $x \in [x_h, \infty)$. In contrast, the e^β function shows a non-monotonic behaviour, with presence of additional local maxima and minima depending on the values of (x_0, N). In the NS case, we have that $e^\alpha \to +\infty$ as $y \to 0$ $(x \to x_0)$ and it is bounded from below by its local minimum $K = A_{\min}$. The function e^β is always positive and has a single maximum, with the possible appearance of additional local maxima and minima depending on the values of (x_0, N).

The scalar field behavior in the NS and BH cases is qualitatively similar, but the self-interaction potentials exhibit distinct behavior, as illustrated in Figs. 4.3 and 4.4. Specifically, as $|\phi| \to \pi\sqrt{2(1 - 1/N)}$ for the NS case, we have $V(\phi) \to -\infty$, while for the BH case, we have $V(\phi) \to \infty$, respectively. Also, one can see that $V(\phi)$ resembles a "Mexican hat" potential with infinity edges, as shown in Figs. 4.3 (b), 4.4 (b).

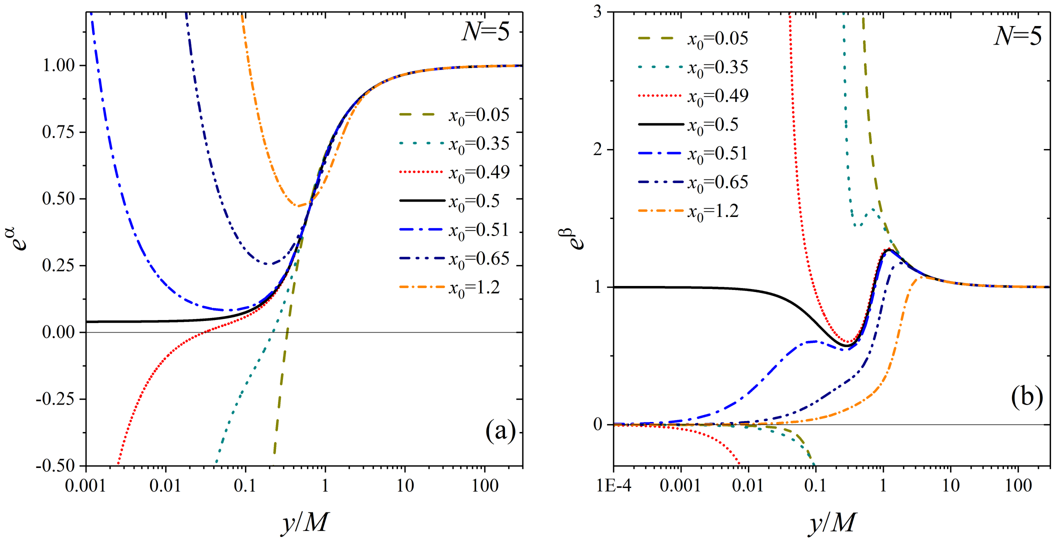

Figure 4.1: The typical behaviour of metric functions e^α (a) and e^β (b) for $N = 5$, $M = 1/6$ for different values of x_0.

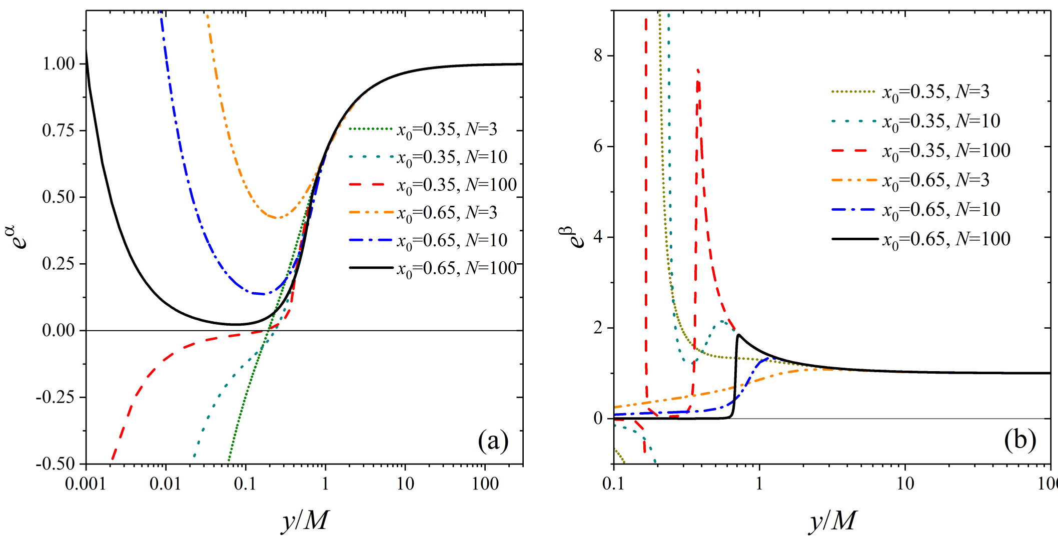

Figure 4.2: The typical behaviour of metric functions e^α (a) and e^β (b) for $M = 1/6$, $x_0 = 0.35$ (BH case) and $x_0 = 0.65$ (NS case) for different values of N.

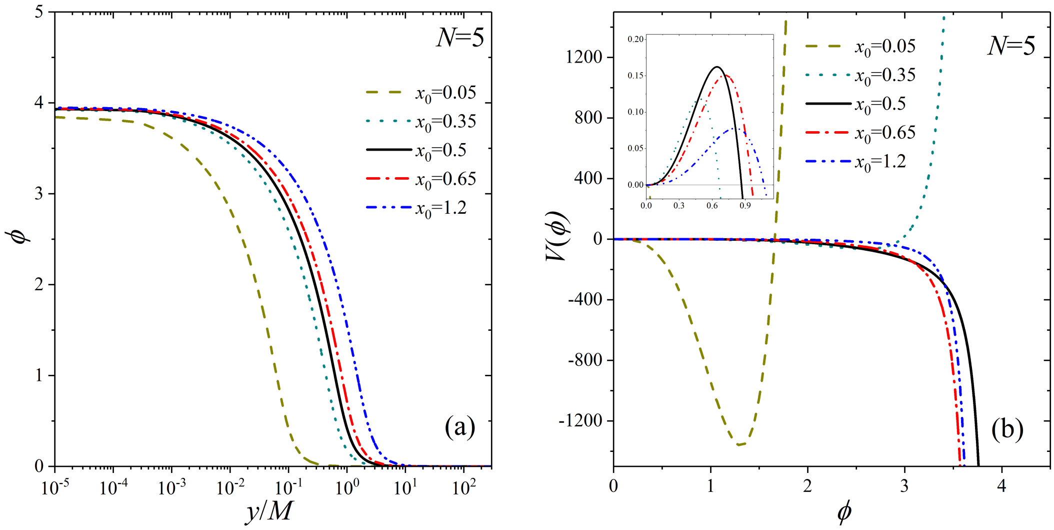

Figure 4.3: The typical behaviour of scalar field ϕ (a) and self-interaction potentials $V(\phi)$ (b) for $N = 5$, $M = 1/6$ and different values of x_0. The smaller panel in Fig. (b) illustrates the behavior of $V(\phi)$ near the origin.

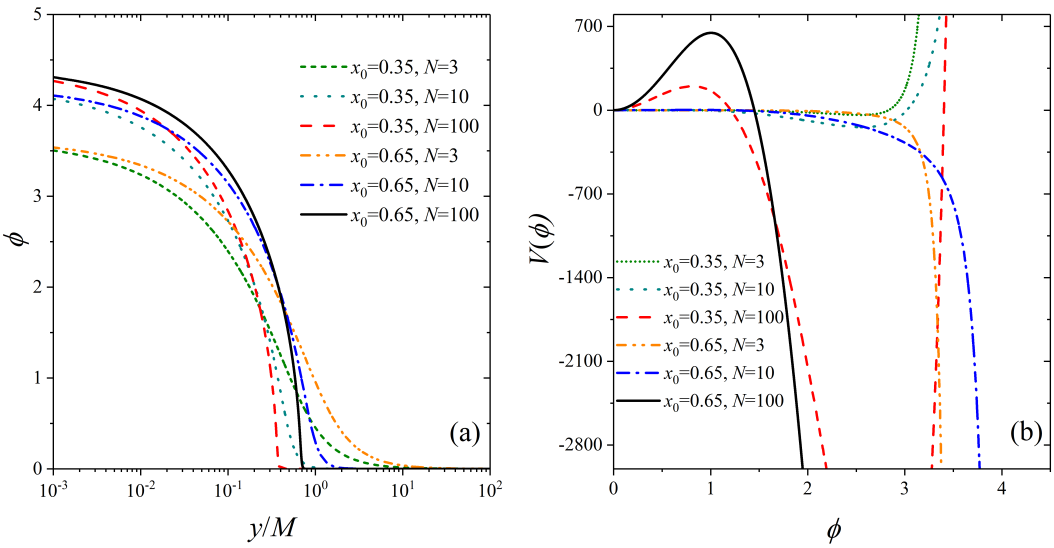

Figure 4.4: The typical behaviour of scalar field ϕ (a) and self-interaction potentials $V(\phi)$ (b) for $M = 1/6$, $x_0 = 0.35$ (BH case) and $x_0 = 0.65$ (NS case) and different values of N.

Chapter 5

Stability and quasi-normal modes

5.1 Basic relations

The perturbed space-time metric can be written in the following form

$$g_{\mu\nu} = g^{(0)}_{\mu\nu} + h_{\mu\nu}, \tag{5.1}$$

where $g^{(0)}_{\mu\nu}$ represents our static background metric and $h_{\mu\nu}$ is a small perturbation, $|h_{\mu\nu}/g^{(0)}_{\mu\nu}| \ll 1$. The inverse metric for linear order perturbations is $g^{\mu\nu} = g^{(0)\mu\nu} - h^{\mu\nu}$, where we use the background metric $g^{(0)}_{\mu\nu}$ to rise or lower indexes of $h_{\mu\nu}$. The first-order perturbations of Einstein's equations can be written as

$$\delta G_{\mu\nu} = 8\pi \delta T_{\mu\nu}, \tag{5.2}$$

where the perturbed functions are defined as

$$\delta\Gamma^{\sigma}_{\mu\nu} = \frac{1}{2} g^{(0)\sigma\delta} \left(\nabla_\nu h_{\mu\delta} + \nabla_\mu h_{\nu\delta} - \nabla_\delta h_{\mu\nu}\right), \tag{5.3}$$

$$\delta R_{\mu\nu} = \nabla_\sigma \delta\Gamma^{\sigma}_{\mu\nu} - \nabla_\nu \delta\Gamma^{\sigma}_{\mu\sigma}. \tag{5.4}$$

And finally

$$\begin{aligned}\delta G_{\mu\nu} =& \nabla_{(\mu}\nabla^{\sigma} h_{\nu)\sigma} - \frac{1}{2}\Big[\nabla_\mu\nabla_\nu h^{\sigma}_{\sigma} + \nabla^2 h_{\mu\nu} + 2R_{\mu}{}^{\alpha}{}_{\nu}{}^{\beta} h_{\alpha\beta} + g^{(0)}_{\mu\nu}\left(\nabla^{\alpha}\nabla^{\beta} h_{\alpha\beta} - \nabla^2 h^{\sigma}_{\sigma}\right) \\ & -2R^{\sigma}{}_{(\mu} h_{\nu)\sigma} + R h_{\mu\nu} - g^{(0)}_{\mu\nu} R^{\alpha\beta} h_{\alpha\beta}\Big].\end{aligned} \tag{5.5}$$

The perturbations $h_{\mu\nu}$ can be considered as expansion in tensor spherical harmonics. It is well known [125], that $h_{\mu\nu}$ can be split into two orthogonal independent classes, even (polar) $h^{even}_{\mu\nu}$ and $h^{odd}_{\mu\nu}$ odd (axial), based on their behavior under the parity transformations. The spherical harmonic index transforms as $(-1)^l$ for the even and $(-1)^{l+1}$ for the odd perturbations, respectively. In this thesis, we focus only on the odd-parity (axial) perturbations. In general case [125–127], we have

$$h_{ta} = \sum_{l,m} h_{0,(lm)}(t,r) E_{ab}\partial^b Y_l^m(\phi,\theta), \;\; h_{ra} = \sum_{l,m} h_{1,(lm)}(t,r) E_{ab}\partial^b Y_l^m(\phi,\theta), \tag{5.6}$$

$$h_{ab} = \frac{1}{2}\sum_{l,m} h_{2,(lm)}(t,r) \left[E_a^c \nabla_{cb} Y_l^m(\phi,\theta) + E_b^c \nabla_{ca} Y_l^m(\phi,\theta)\right],$$

where $Y_l^m(\phi,\theta)$ is spherical function, $E_{ab} = \sqrt{\det\gamma}\epsilon_{ab}$, $(a,b) = (\theta,\phi)$, γ_{ab} is a metric on a two-dimensional sphere, and ϵ_{ab} is a totally anti-symmetric tensor, respectively.

The perturbed part of the Einstein equations is also gauge invariant under infinitesimal transformations $x^\mu = x^\mu + \xi^\mu$. Then $h_{\mu\nu}$ transforms as

$$h_{\mu\nu} = h_{\mu\nu} - 2\nabla_{(\nu}\xi_{\mu)}. \tag{5.7}$$

In general case arbitrary vector ξ^μ can be also decomposed as

$$\xi_t = \sum_{l,m} A_{lm}(t,r) Y_l^m(\phi,\theta), \;\; \xi_r = \sum_{l,m} B_{lm}(t,r) Y_l^m(\phi,\theta), \tag{5.8}$$

$$\xi_a = \sum_{l,m}\Big[C_{lm}(t,r)\partial_a Y_l^m(\theta,\phi) + D_{lm}(t,r) E_a^b \partial_b Y_l^m(\theta,\phi)\Big].$$

Where A_{lm}, B_{lm}, C_{lm}, D_{lm} some arbitrary functions, which can be used to fix some components of $h_{\mu\nu}$.

For odd-parity perturbations, we have

$$\xi_t = 0, \quad \xi_r = 0, \quad \xi_a = \sum_{l,m} D_{lm}(t,r) E_a{}^b \partial_b Y_l^m(\theta,\phi), \tag{5.9}$$

Then for $h_{\mu\nu}$, we have

$$h_0 = h_0 + \frac{d}{dt} D_{lm}(t,r), \;\; h_1 = h_1 + r^2 \frac{d}{dr}\left(\frac{D_{lm}(t,r)}{r^2}\right) \tag{5.10}$$

$$h_2 = h_2 + 2D_{lm}(t,r). \tag{5.11}$$

By fixing $h_2 = 0$, we can obtain the Regge-Wheeler gauge [125]. One of the main advantages of this gauge is independence from the m.

The explicit form of $h^{odd}_{\mu\nu}$ in the the Regge-Wheeler gauge is

$$h^{odd}_{\mu\nu} = \begin{bmatrix} 0 & 0 & 0 & h_0(t,r) \\ 0 & 0 & 0 & h_1(t,r) \\ 0 & 0 & 0 & 0 \\ h_0(t,r) & h_1(t,r) & 0 & 0 \end{bmatrix} \left(\sin\theta \frac{\partial}{\partial\theta}\right) P_l(\cos\theta)\,, \tag{5.12}$$

where $h_0(t,r)$ and $h_1(t,r)$ are unknow functions and $P_l(\cos\theta)$ is the Legendre polynomial with $l \geq 2$.

We are interested in static spherically symmetric solutions and therefore the general ansatz for the metric $g^{(0)}_{\mu\nu}$ can be taken in the form

$$ds^2 = A(r)dt^2 - B(r)dr^2 - R^2(r)(d\theta^2 + \sin^2\theta d\varphi^2). \tag{5.13}$$

By substituting $g_{\mu\nu} = g^{(0)}_{\mu\nu} + h^{odd}_{\mu\nu}$ and $\phi(x^\mu) = \phi_0(r) + \delta\phi(x^\mu)$ into the Einstein-SF equations and saving only linear terms, we obtain

$$\delta\phi(x^\mu) = 0, \tag{5.14}$$

which is in accordance with [128] and the following equations for the perturbations

$$\ddot{h}_1 - \dot{h}'_0 + \frac{2R'}{R}\dot{h}_0 + A\frac{(l-1)(l+2)}{R^2}h_1 = 0,\ \ \dot{h}_0 - \frac{A}{B}h'_1 - \frac{1}{2}\left(\frac{A}{B}\right)' h_1 = 0. \tag{5.15}$$

After simple transformations, these equations can be reduced to the master wave equation.

$$\left(\frac{\partial^2}{\partial t^2} - \frac{\partial^2}{\partial r^{*2}}\right)\Psi(t,r^*) + V_{\text{eff}}(r,l)\Psi(t,r^*) = 0, \tag{5.16}$$

where $r^*(r)$ is a “tortoise” coordinate and Ψ is a new function, defined by

$$\frac{dr^*}{dr} = \sqrt{\frac{B}{A}},\ \ \Psi(t,r^*) = \sqrt{\frac{A}{B}}\frac{h_1(t,r^*)}{R}. \tag{5.17}$$

The effective potential $V_{\text{eff}}(r,l)$ for odd-parity perturbations has form

$$V_{\text{eff}}(r,l) = \frac{3A}{2B}\left(\frac{R'}{R}\right)^2 - \frac{A}{2B}\frac{R''}{R} - \frac{d}{dr}\left(\frac{A}{2B}\frac{R'}{R}\right) + A\frac{(l-1)(l+2)}{R^2}, \tag{5.18}$$

where $r = r(r^*)$.

The analytical solution with $V_{\rm eff}$ are not known, so we have to solve it numerically. To do this, we use a finite difference method. In the first option, we can replace derivatives with their central differences, and the resulting numerical scheme is following

$$\Psi_N = -\Psi_S + \left(\frac{\Delta t}{\Delta r^*}\right)^2 \left[\Psi_W - 2\Psi_C + \Psi_E\right] + \left[2 - (\Delta t)^2 V(C)\right]\Psi_C, \quad (5.19)$$

where the indices (N, W, C, E, S) denote the points on the space-time square grid, defined as $N = (t + \Delta t, r^*)$, $W = (t, r^* - \Delta r^*)$, $C = (t, r^*)$, $E = (t, r^* + \Delta r^*)$, $S = (t - \Delta t, r^*)$, and Δt, Δr^* are the corresponding time and space grid steps. The von Neumann stability condition requires that $k = \frac{\Delta t}{\Delta r^*} < \left(1 + \Delta r^{*2} V_{\rm eff,max}/4\right)^{-1/2}$. An illustration of the grid is shown in Fig. 5.1 (a).

Alternatively, we can rewrite the corresponding wave equation (5.16) in terms of the light-cone variables $u = t - r^*$, $v = t + r^*$ as

$$4\frac{\partial^2}{\partial u \partial v}\Psi(u, v) + V_{\rm eff}(u, v, l) = 0, \quad (5.20)$$

and use the Gundlach, Price, and Pullin numerical scheme [87, 129]

$$\Psi_N = \Psi_W + \Psi_E - \Psi_S - \frac{\Delta^2}{8} V_{\rm eff}(S)(\Psi_W + \Psi_E) + O(\Delta^4), \quad (5.21)$$

or the numerical scheme proposed by Chirenti and Rezzolla in [130]

$$\Psi_N = (\Psi_W + \Psi_E)\frac{16 - \Delta^2 V_{\rm eff}(S)}{16 + \Delta^2 V_{\rm eff}(S)} - \Psi_S + O(\Delta^4). \quad (5.22)$$

In both cases the indices (N, W, E, S) correspond to the grid points of the space-time triangular grid, defined as $N = (u + \Delta, v + \Delta)$, $W = (u + \Delta, v)$, $E = (u, v + \Delta)$, $S = (u, v)$, and Δ is the grid step size. We assume that the grid is equidistant and it is schematically shown in Fig. 5.1 (b).

The both schemes give the very close results.

As the initial condition, for the black hole case, we can take a Gaussian packet of width σ centered at $r^* = r^*_c$, i. e.

$$\Psi(r^*, t < 0) = 0, \quad \Psi(r^*, t = 0) = e^{-\frac{(r^* - r^*_c)^2}{2\sigma^2}}. \quad (5.23)$$

In black hole cases, singularities are hidden beneath the horizon, yielding globally hyperbolic space-times characterized by well-defined dynamics. However, in presence of the naked singularity the space-time isn't globally

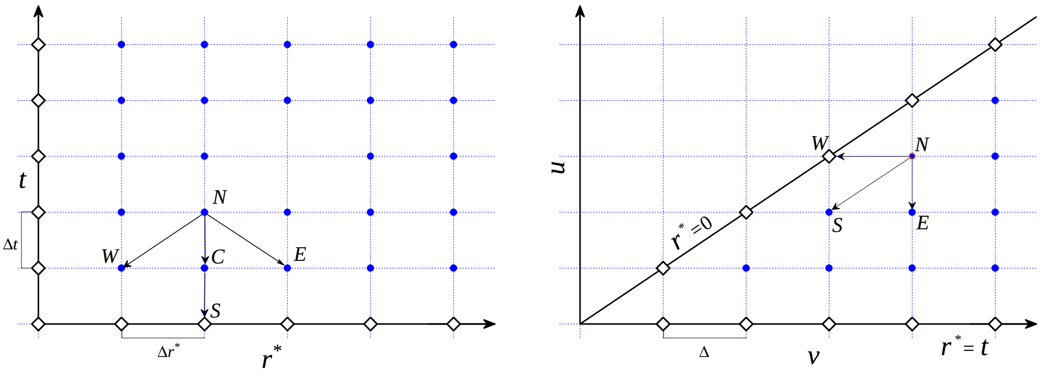

Figure 5.1: Typical example of the numerical grid. White diamonds and blue points correspond to known and unknown values, respectively.

hyperbolic anymore and the corresponding time evolution governed by (5.16) may not be unique [131], even for reasonable initial data. Despite this, it is still possible to have sensible dynamics in such space-times [1, 131–133] by suggesting specific boundary conditions at the singularity and restricted class of functions. In practice, this means, that we replacing the spatial part $\mathcal{H} = -\frac{d^2}{dr^{*2}} + V_{\text{eff}}$ of our wave operator (5.16) with its self-adjoint extension $\mathcal{H}_E$ [134]. If there is a unique self-adjoint extension, then the form of the initial conditions uniquely determine the time evolution, without any ambiguity in the boundary conditions at the singularity. If the self-adjoint extension is non-unique, we have to choose one of them by imposing some specific boundary condition. The number of self-adjoint extensions can be tested by using the von Neumann deficiency indices method or by the Weyl's limit point - limit circle criterion [135].

In the following, we consider only finite perturbations and use the Dirichlet boundary condition at the singularity $r^* = 0$

$$\Psi(t, r^* = 0) = \Psi(u = v, v) = 0. \tag{5.24}$$

Similarly to the BH case we can also use initial perturbation in the form of a Gaussian wave packet, i.e.

$$\Psi(u = 0, v) = A \exp\left[-\frac{(v - v_c)^2}{2\sigma^2}\right] \text{ or } \Psi(r^*, t = 0) = e^{-\frac{(r^* - r_c^*)^2}{2\sigma^2}}. \tag{5.25}$$

The resulting time-domain profiles during the ringdown phase can be represented as sum of complex exponentials $\Psi(t) \simeq \sum_{j=1}^{p} A_j e^{-i\omega_j t}$. In order to extract the fundamental frequency $\omega = \omega_R + i\omega_I$ from $\Psi(r^* = r_1^*, t)$ at some point r_1^* we use the well-known Prony method [136] with 250 − 800 terms.

5.2 $V(\phi) = w\phi^{2n}$

5.2.1 Properties of the V_{eff}

In curvature coordinates, defined as

$$A(r) = e^{\alpha(r)},\ B(r) = e^{\beta(r)},\ R(r) = r,$$

the effective potential $V_{\text{eff}}(r,l)$ takes the following form

$$V_{\text{eff}}(r,l) = e^{\alpha-\beta}\left(\frac{\beta'-\alpha'}{2r} + e^{\beta}\frac{(l-1)(l+2)}{r^2} + \frac{2}{r^2}\right), \tag{5.26}$$

using (2.18, 2.19), we can rewrite it as

$$V_{\text{eff}}(r,l) = e^{\alpha-\beta}\left(e^{\beta}\frac{(l-1)(l+2)-1}{r^2} + \frac{3}{r^2} + 8\pi e^{\beta}V(\phi)\right) > 0. \tag{5.27}$$

Near spatial infinity $r \to \infty$, the behaviour of the effective potential and the "tortoise" are as follows

$$r^* = r + r_g \ln r + O\left(\frac{1}{r}\right), \quad V(r) = \frac{l(l+1)}{r^2} + O\left(\frac{1}{r^3}\right), \quad V(r^*) \sim \frac{l(l+1)}{r^{*2}} \tag{5.28}$$

and near the singularity, we have

$$r^* = \frac{r^2}{2Y_0} + o(r^{\eta+3}), \quad V_{\text{eff}}(r) = \frac{3Y_0^2}{r^4} + o\left(r^{\eta-3}\right), \quad V_{\text{eff}}(r^*) = \frac{3}{4r^{*2}} + o\left(r^{*(\eta-3)/2}\right). \tag{5.29}$$

Equation (5.16) admits solutions in the form $\Psi = e^{\pm i\omega t}\psi(r^*)$, which leads to a Schrödinger-like equation for the spatial part of the wave operator

$$\mathcal{H}\psi = \omega^2\psi,\ \mathcal{H} = -\frac{d^2}{dr^{*2}} + V_{\text{eff}}(r^*,l), \tag{5.30}$$

where ω plays role of the eigenvalue. Near the singularity it takes the form

$$\psi''(r^*) + \left(\omega^2 - \frac{3}{4r^{*2}}\right)\psi(r^*) = 0, \tag{5.31}$$

and the corresponding solution is

$$\psi(r^*) = \sqrt{r^*}\left[C_1 J_1(\omega r^*) + C_2 Y_1(\omega r^*)\right] \sim \tilde{C}_1 (r^*)^{3/2} + \tilde{C}_2 (r^*)^{-1/2}. \tag{5.32}$$

The second solution isn't square-integrable near the singularity. Thus, the operator $\mathcal{H}$ is essentially self-adjoint which means that he has a unique self-adjoint extension $\mathcal{H}_E$. This extension is defined on the class of functions, that satisfy $\sqrt{r^*}\psi(r^*)|_{r^*=0} = 0$.

We also need to note that this holds true for any self-interaction potential that satisfies the assumptions from Chapter 2.

From (5.27), one can observe that the potential V_{eff} is always positive for all $V(\phi) \geq 0$, and from (5.28) that it decays at spatial infinity. Hence, all solutions of the master equation will be bounded in time and the exponentially growing modes are ruled out. This implies that the corresponding space-times with naked singularities are stable under odd-parity perturbations.

The examples of the typical behavior of the effective potential are shown in Fig. 5.2 for different values of Q(a), M(b) and n(c), respectively. One can see that for some set-up of parameters the local maximum of V_{eff} can appear.

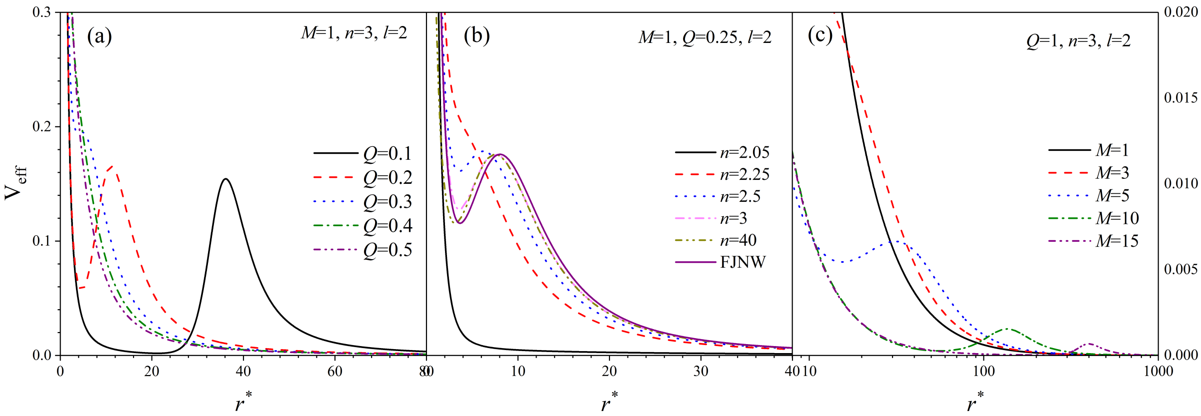

Figure 5.2: The typical behaviour of the effective potential $V_{\text{eff}}(r, l = 2)$: (a) $M = 1$, $n = 3$ for different Q (b) $Q = 0.25$, $M = 1$ for different n (c) $Q = 1$, $n = 3$ M for different M.

5.2.2 Quasi-normal modes

The typical examples of time-domain profiles are shown in Fig. 5.3. The left panel (a) of this figure shows the series of echoes within the interval $(0, Q_1)$. However, it can observed that echoes in the time-domain profiles align at late times, allowing us to observe a standard ringdown profile with very small value of $\mathrm{Im}(\omega)$. For larger values of Q, the local maximum of the effective potential disappears, and the time-domain profiles Ψ consist only few oscillations and look like a "single wave" with a power-law tail (see (c)). In such cases, it becomes hard or impossible to extract frequencies with adequate accuracy.

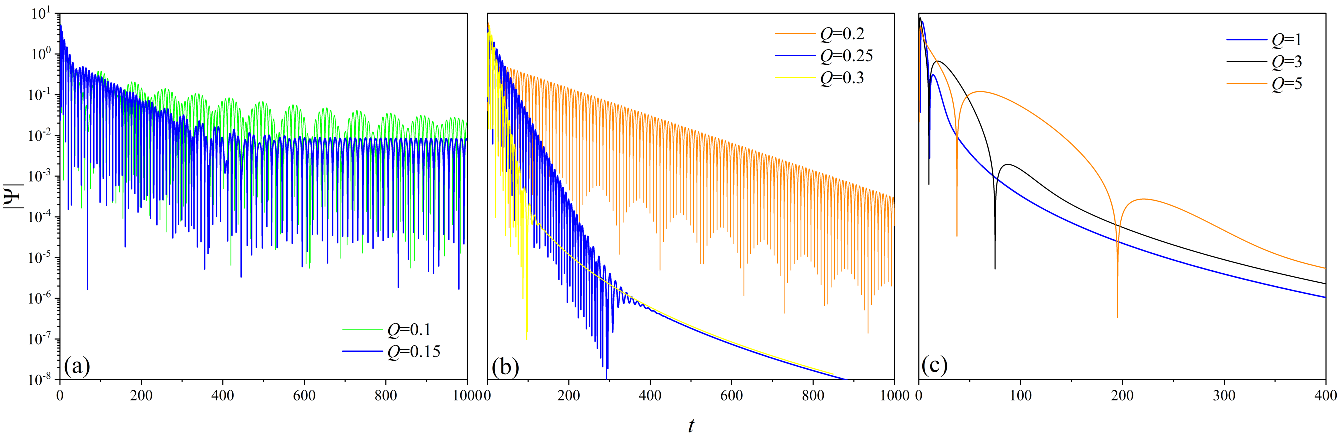

Figure 5.3: The typical examples of time-domain profiles $|\Psi(t, r^* = 200)|$ for $l = 2$, $n = 3$, $M = 1$. The left panel demonstrates solutions of wave equation where echoes are presence. One can see that on blue curve echoes align and ringdown profile appears. For $Q = 0.15$ (blue curve) the echoes align for $t > 600$.

The typical dependencies of the fundamental QNM as functions of Q, M and n are presented in Figs. 5.4–5.8 and examples of the exact values of ω are provided in Tabs. 5.1–5.4.

In Figs. 5.4–5.7, we can observe that $\omega(Q)$ and $\omega(M)$ curves, with fixed n and l, approach to the FJNW case for high values of n. In all cases, the curves demonstrate non-monotonic behavior and remain bounded. The $\omega_R(\omega_I)$ dependencies always consist a local maxima (minima). Beyond certain values of Q or M, the number of oscillations decreases, and Ψ takes on the form of a "single wave" profile (as illustrated in Fig. 5.3 (c)) with $\omega \to 0$. However, increasing the value of l or selecting lower values of n may lead to an increased number of oscillations in the ringdown.

In Fig. 5.8 are shown dependencies of ω on n with fixed Q, M, and $l = 2$. It can be observed that ω does not tend towards the value of ω_{FJNW} as $n \to \infty$. This can be explained as the influence of the region where $|\phi(r)| > 1$. Increasing the value of l leads to the disappearance of this effect. We found that in the eikonal approximation, this effect is absent.

Table 5.1: The values of fundamental QNM frequencies $M\omega$ for $M = 1$, $l = 2$ and different values of Q.

	$n = 2.1$	$n = 3$	FJNW
Q	$M\omega$		
Schwarzschild	$0.3730 - 0.0891i$	$0.3730 - 0.0891i$	$0.3730 - 0.0891i$
0.2	$0.4304 - 0.2426i$	$0.3815 - 0.0077i$	$0.3683 - 0.0052i$
0.25	$0.2172 - 0.2558i$	$0.4639 - 0.04798i$	$0.45481 - 0.0381i$
0.3	$0.0874 - 0.1371i$	$0.5051 - 0.112i$	$0.5042 - 0.0974i$
0.35	$0.0346 - 0.0573i$	$0.5131 - 0.1799i$	$0.5213(5) - 0.166i$
0.45	$0.0066 - 0.0112i$	$0.4682 - 0.2874i$	$0.4888 - 0.2839i$
0.55	$0.00194 - 0.0034i$	$0.3933 - 0.3449i$	$0.4161 - 0.3558i$
0.65	$0.00081 - 0.0014i$	$0.3203 - 0.3653i$	$0.3388 - 0.388i$

Table 5.2: The values of fundamental QNM frequencies $M\omega$ for $M = 1$, $l = 3$ and different values of Q.

	$n = 2.1$	$n = 3$	FJNW
Q	$M\omega$		
Schwarzschild	$0.5993 - 0.0927i$	$0.5993 - 0.0927i$	$0.5993 - 0.0927i$
0.2	$0.6917 - 0.2536i$	$0.489 - 0.0002i$	$0.4643 - 9 \cdot 10^{-5}i$
0.25	$0.4005 - 0.322i$	$0.6413 - 0.0145i$	$0.6196 - 0.0084i$
0.3	$0.1731 - 0.1748i$	$0.7293 - 0.0701i$	$0.7179 - 0.0534i$
0.35	$0.0692 - 0.0712i$	$0.7703 - 0.1484i$	$0.7723 - 0.1268i$
0.45	$0.0132 - 0.0137i$	$0.7567 - 0.2992i$	$0.7824 - 0.286i$
0.55	$0.0039 - 0.0041i$	$0.6803 - 0.3998i$	$0.7172 - 0.4067i$
0.65	$0.0016 - 0.0017i$	$0.5898 - 0.4512i$	$0.6269 - 0.4791i$

Table 5.3: The values of fundamental QNM frequencies $M\omega$ for $M = 1$, $l = 2$ and different values of n.

	$Q = 0.15$	$Q = 0.3$	$Q = 0.45$
n	$M\omega$		
Schwarzschild	$0.3730 - 0.0891i$	$0.3730 - 0.0891i$	$0.3730 - 0.0891i$
FJNW	$0.2436 - 0.00006i$	$0.5042 - 0.0974i$	$0.4888 - 0.2839i$
2.05	$0.467 - 0.1918i$	$0.0073 - 0.0123i$	$0.0006 - 0.001i$
2.1	$0.4517 - 0.0484i$	$0.0876 - 0.1369i$	$0.0066 - 0.0112i$
2.3	$0.3178 - 0.0012i$	$0.4698 - 0.2222i$	$0.2654 - 0.2943i$
2.5	$0.2802 - 0.00029i$	$0.5016 - 0.1558i$	$0.3952 - 0.306i$
3	$0.2532 - 0.00009i$	$0.5052 - 0.112i$	$0.4682 - 0.2874i$
4	$0.245 - 0.00007i$	$0.5043 - 0.0995i$	$0.4867 - 0.2837i$
5	$0.2439 - 0.0000633i$	$0.5042 - 0.0979i$	$0.4885 - 0.2839i$
7	$0.2436 - 0.0000625i$	$0.5042 - 0.0976i$	$0.48882 - 0.28394i$
10	$0.2436 - 0.0000624i$	$0.5042 - 0.0975i$	$0.48886 - 0.28395i$

Table 5.4: The values of fundamental QNM frequencies $M\omega$ for $M = 1$, $l = 3$ and different values of n. The hyphen $(-)$ in a cell indicates a situation where we cannot extract the value of ω due to the presence of echoes.

	$Q = 0.15$	$Q = 0.3$	$Q = 0.45$
n	$M\omega$		
Schwarzschild	$0.5993 - 0.0927i$	$0.5993 - 0.0927i$	$0.5993 - 0.0927i$
FJNW	$0.2796 - 6 \cdot 10^{-8}i$	$0.7183 - 0.0535i$	$0.7824 - 0.286i$
2.05	$0.721 - 0.1773i$	$0.0146 - 0.0151i$	$0.0012 - 0.0013i$
2.1	$0.6305 - 0.0158i$	$0.173 - 0.1748i$	$0.0132 - 0.0137i$
2.3	$0.3861 - 6 \cdot 10^{-6}i$	$0.7352 - 0.2153i$	$0.4839 - 0.3661i$
2.5	$0.33 - 6 \cdot 10^{-7}i$	$0.7475 - 0.1226i$	$0.6675 - 0.3476i$
3	$-$	$0.7293 - 0.0701i$	$0.7567 - 0.2992i$
4	$-$	$0.7201 - 0.056i$	$0.7792 - 0.2868i$
5	$-$	$0.7188 - 0.0541i$	$0.7817 - 0.2861i$
7	$-$	$0.7184 - 0.0536i$	$0.7823 - 0.286i$
10	$-$	$0.7184 - 0.0535i$	$0.78235 - 0.286i$

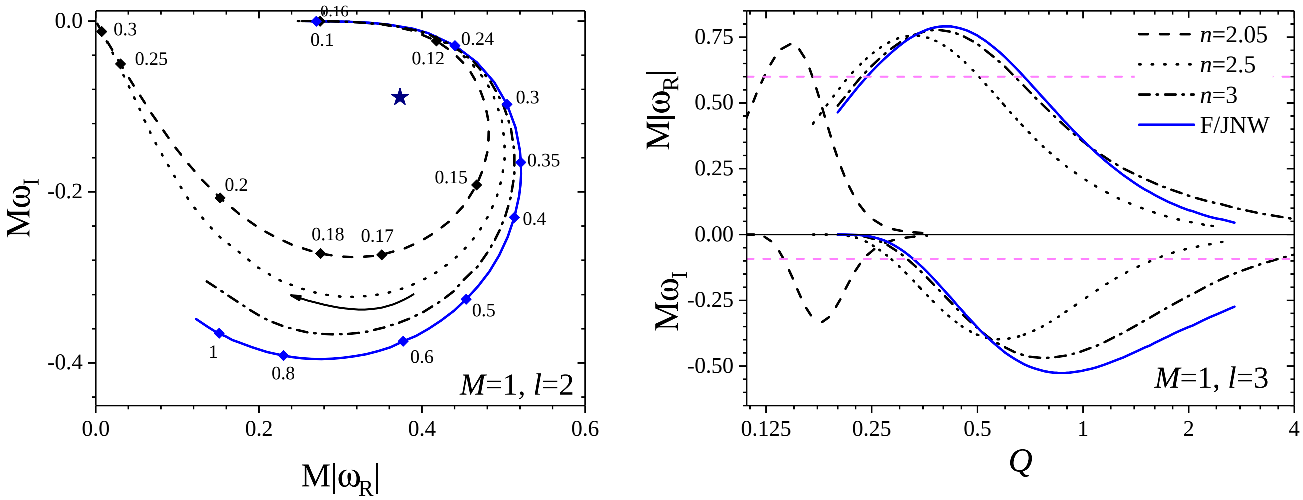

Figure 5.4: Left panel: the trajectories of the fundamental QNM frequencies in the ω plane as functions of Q for different values of n with $l = 2$, $M = 1$. Black arrows show the direction of increasing Q. Right panel: The dependencies ω_R and ω_I as functions of Q. The blue star and the horizontal dashed lines relate to the corresponding value of ω in the Schwarzschild black hole case, respectively. As n increases, the dependencies approach the curves in the FJNW case.

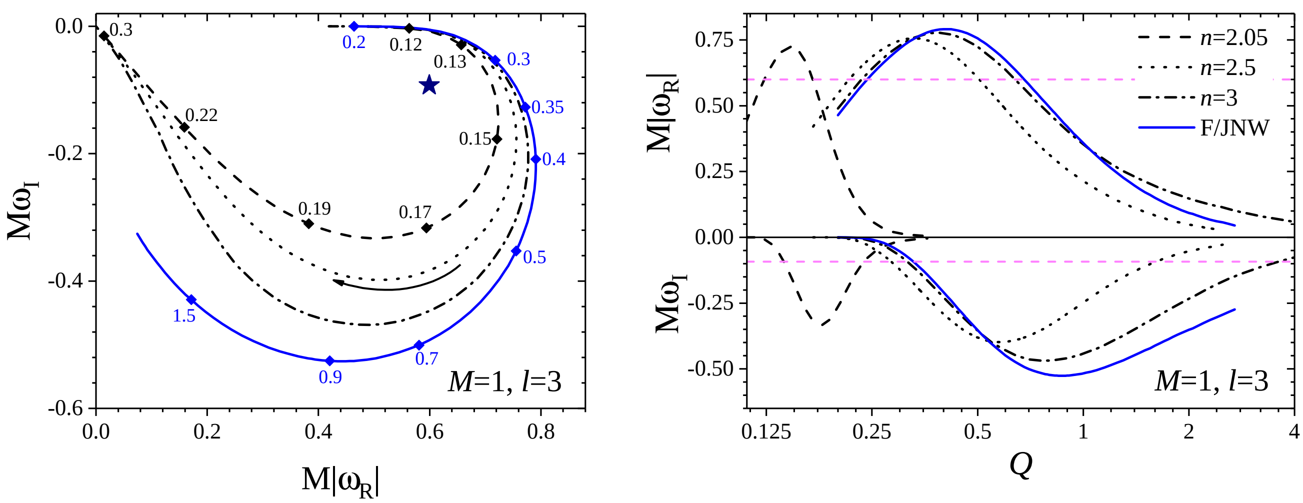

Figure 5.5: The same as in Fig. 5.5 but for $M = 1$, $l = 3$.

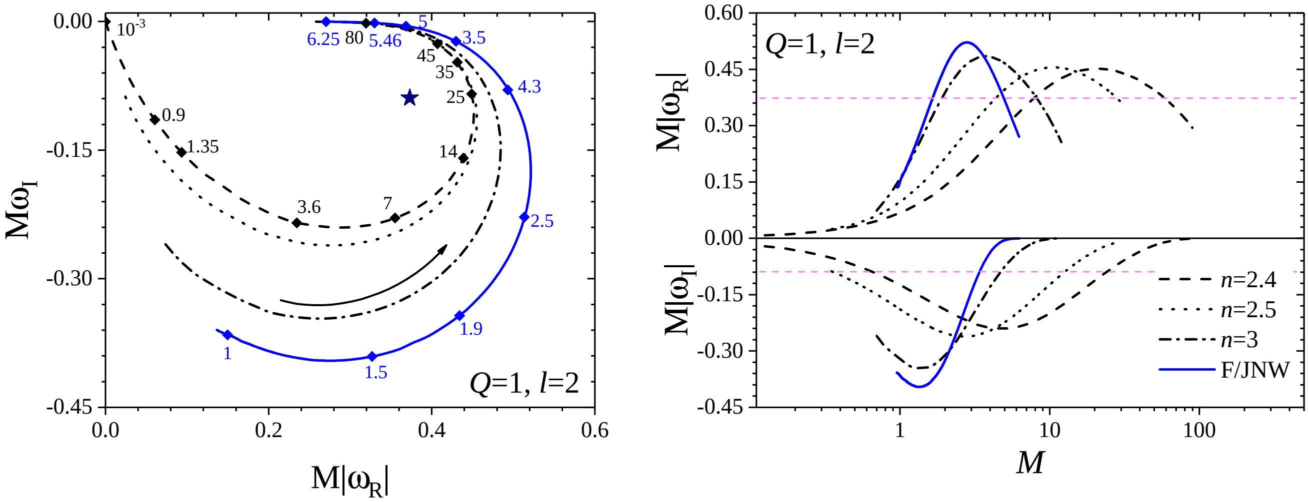

Figure 5.6: Left panel: the trajectories of the fundamental QNM frequencies in the ω plane as functions of M with $l = 2$, $Q = 1$ and various values of n. Black arrows show the direction of increasing M. Right panel: The dependencies ω_R and ω_I as functions of M. The blue star and the horizontal dashed lines relate to the corresponding value of ω in the Schwarzschild black hole case, respectively.

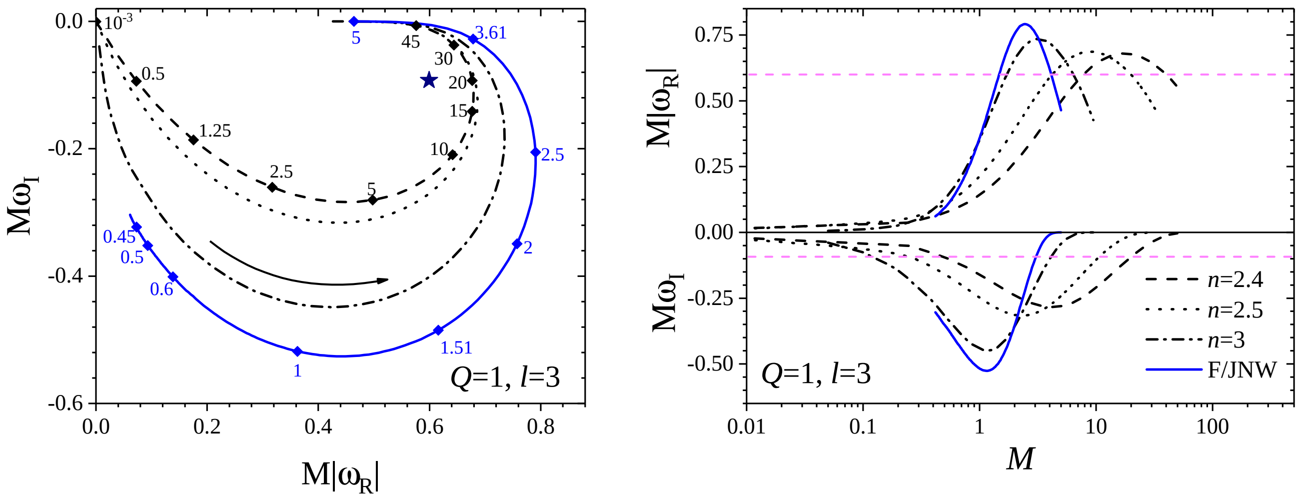

Figure 5.7: The same as in Fig. 5.6 but for $Q = 1$, $l = 3$.

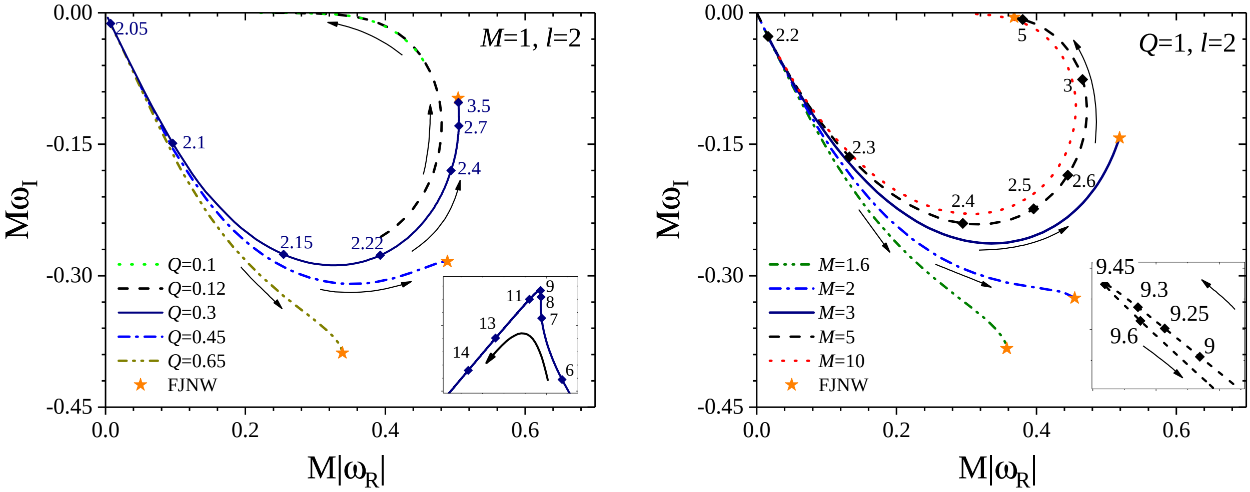

Figure 5.8: The fundamental QNM frequencies for $l = 2$ as functions of n for several fixed M, Q. Left panel: The ω trajectories for $M = 1$ and different Q. Left panel: The ω trajectories for $Q = 1$ and different M. Black arrows show the direction of increasing n.

5.3 $V(\phi) = w \sinh\left(\kappa\phi^{2n}\right)$

5.3.1 Properties of the V_{eff}

Now, we proceed to the strongly nonlinear case, when the spherical singularities are present. Asymptotic properties of solutions near the spherical singularity $r = r_s$ are drastically different from the previously considered case. So we expect some modification in the V_{eff} behaviour.

The behavior of V_{eff} at spatial infinity is defined in the same way as for (5.28). Furthermore, in the domain (r_1, ∞), where $|\phi(r)| < 1$, the corresponding self-interacting potential can be approximated as $V(\phi) = w \sinh\big(\kappa\phi^{2n}\big) \approx w\kappa\phi^{2n}$.

By introducing the tortoise coordinate, we map $r^* : (r_s, \infty) \to (0, \infty)$. Then, taking into account the asymptotic behaviour of α and β near $r = r_s$

$$\alpha \sim \alpha_0, \ \beta \sim -\left(\frac{2\pi r_s}{n(n-1)(r-r_s)}\right)^{\frac{n}{n-1}} - \left(\frac{2n-1}{n-1}\right) \ln\left[\frac{r_s}{(r-r_s)}\right], \tag{5.33}$$

Then, we have

$$r^* \sim \frac{2}{1+2\Delta}\frac{(r-r_s)^{1+\Delta}}{A^{1+2\Delta}} e^{-\frac{1}{2}\{\alpha_0+\beta_0(r)\}}, \quad V_{\text{eff}}(r^*) \sim \frac{2^{\frac{1}{n}}\pi}{n^2(r^*)^2|\ln r^*|^{2-1/n}}. \tag{5.34}$$

Unfortunately, we are unable to derive analytical solutions of (5.30) in this case. But we can use the Weyl's limit point-limit circle criterion.

The difference from the previous case is in presence of $|\ln r^*|^{2-1/n}$ in the denominator, that lead to less repulsion near the singularity. It is evident, that $V_{\text{eff}}(r^*) < \frac{3}{4r^{*2}}$ as $r^* \to 0$. Thus $\mathcal{H}$ (5.30) is in the limit circle near zero and $\mathcal{H}$ is not essentially self-adjoint operator ([135], theorem X.10).

In general, there are no specific preferences in choosing a particular self-adjoint extension. Therefore, we can use the Dirichlet boundary condition at the singularity, as in the previous case.

Consequently, our problem can be partially reduced to the previously considered case, and as we found, the values of QNM are very close in the both cases for the same values of parameters $\kappa = 1$, Q, M, and n. This is demonstrated in Fig. 5.9, where we show the relative difference between ω for these two cases.

We need to note that in both cases, we fix $w = 1$, but in the present case, we have an additional free parameter κ, which we can also vary. The behavior of the time-domain profiles and effective potential are qualitatively similar, and in the case of $\kappa = 1$, they are quantitatively similar as well, so we do not show them.

5.3.2 Quasi-normal modes

The typical dependencies of the fundamental QNM as functions of Q, n, and κ are shown in Figs. 5.10–5.11. Tables 5.5–5.6 list examples of the numerical values of ω.

The behavior of the ω curves as functions of Q, M, and n is qualitatively similar to the previous case, as observed in Figs. 5.10–5.11 (left panel). We can see, that $\kappa > 1$ leads to a shift of the corresponding ω curves towards higher values, while $0 < \kappa < 1$ leads to a shift towards lower values.

The dependencies of ω as functions of κ also exhibit non-monotonic behavior, as illustrated in Fig. 5.11 (right panel).

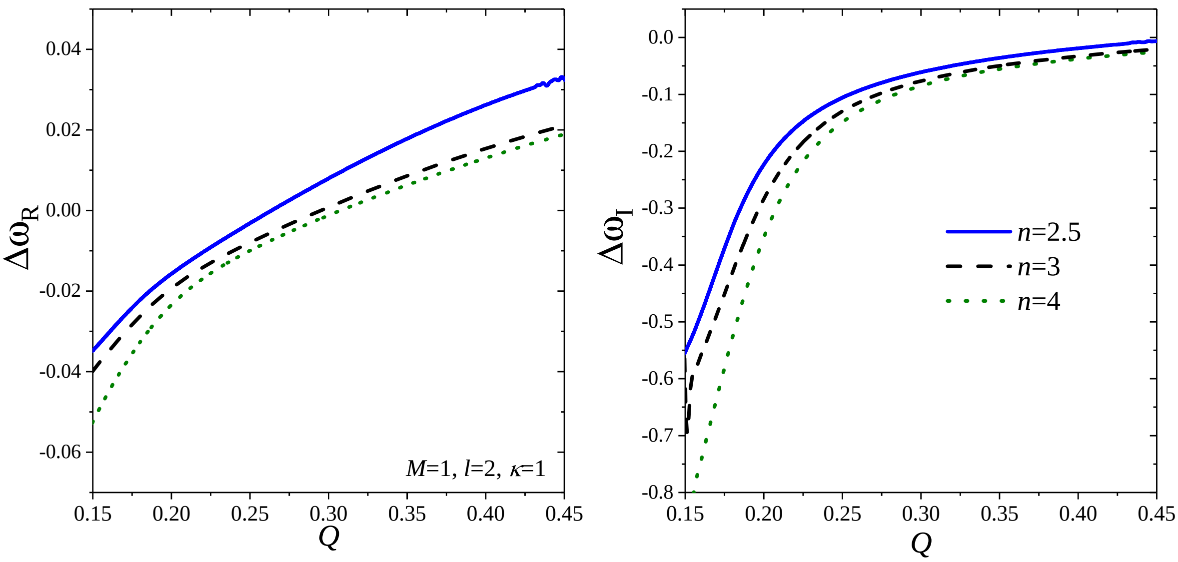

Figure 5.9: The differences $\Delta\omega_i = \left(\omega_i^{\phi^{2n}} - \omega_i^{\sinh\phi^{2n}}\right)/\omega_i^{\phi^{2n}}$, $i = (R, I)$ between the frequencies in the current and the previous cases.

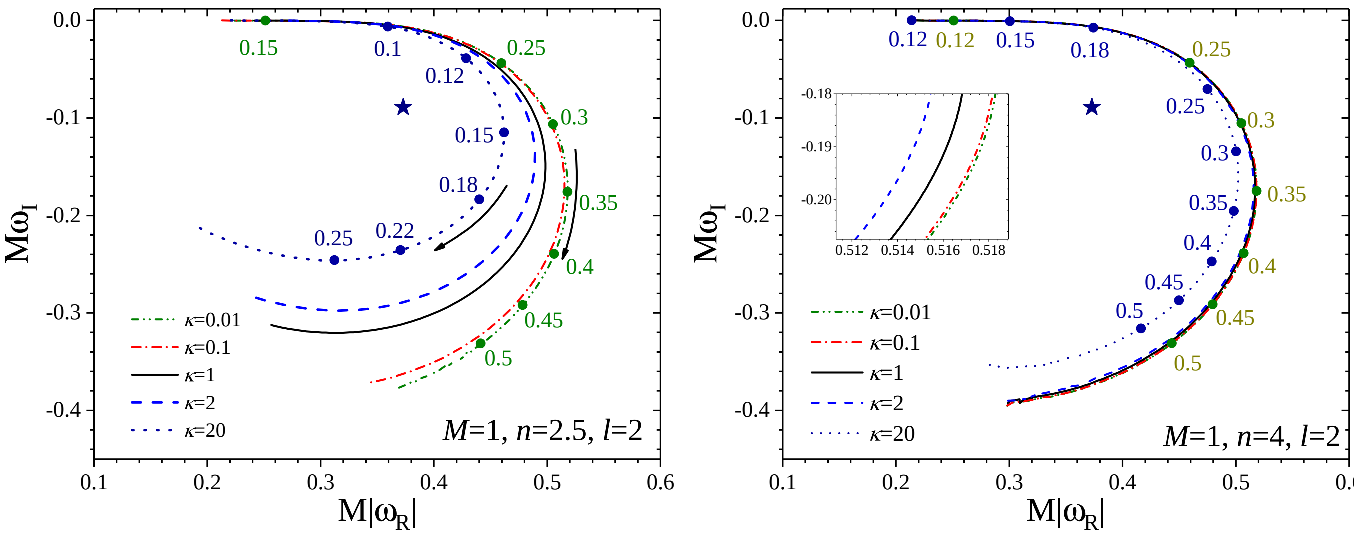

Figure 5.10: The trajectories of the QNM fundamental frequencies in the ω plane with $l = 2$, $M = 1$, and $n = 2.5$ (left panel) $n = 4$ (right panel) as functions of Q for different κ values. Black arrows show the direction of increasing Q. The blue star and colored dots correspond to the Schwarzschild BH case and different values of Q, respectively.

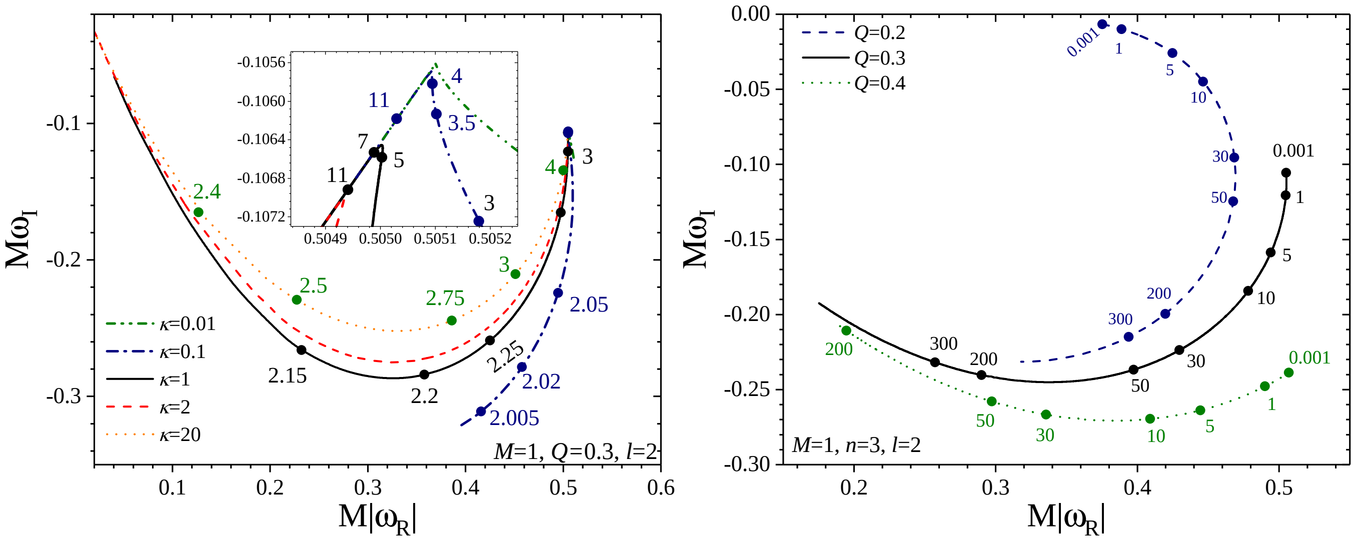

Figure 5.11: Left panel: the trajectories of the fundamental frequencies in the ω plane with $l = 2$, $M = 1$, $Q = 0.3$ as functions of n for different values of κ. Right panel: The trajectories of the fundamental frequencies in the ω plane with $l = 2$, $M = 1$, $n = 3$ as functions of κ for different values of Q . The colored dots correspond to different values of n and κ, respectively.

Table 5.5: The values of the fundamental QNM frequencies $M\omega$ for $M = 1$, $n = 6$, $l = 2$ and different values of κ.

	$Q = 0.15$	$Q = 0.3$	$Q = 0.4$
κ	$M\omega$		
Schwarzschild	$0.3737 - 0.08901i$		
ϕ^{2n}	$0.2532 - 9.5 \cdot 10^{-5}i$	$0.5053 - 0.11204i$	$0.4978 - 0.24i$
0.001	$0.251 - 9 \cdot 10^{-5}i$	$0.5051 - 0.1056i$	$0.507 - 0.2388i$
0.01	$0.2511 - 9.1 \cdot 10^{-5}i$	$0.5051 - 0.10575i$	$0.5069 - 0.2389i$
0.1	$0.2521 - 9.5 \cdot 10^{-5}i$	$0.5052 - 0.1072i$	$0.5052 - 0.2399i$
1	$0.2633 - 0.00015i$	$0.5048 - 0.1206i$	$0.4902 - 0.24787i$
2	$0.2752 - 0.00025i$	$0.503 - 0.1328i$	$0.4762 - 0.2539i$
10	$0.3423 - 0.0031i$	$0.4783 - 0.1843i$	$0.4091 - 0.2696i$
50	$0.433 - 0.041i$	$0.3973 - 0.2368i$	$0.2973 - 0.258i$

Table 5.6: The values of the fundamental QNM frequencies for $M = 1$, $n = 6$, $l = 3$ and various values of κ. The hyphen $(-)$ in a cell indicates a situation where we cannot extract the value of ω due to the presence of echoes.

	$Q = 0.15$	$Q = 0.3$	$Q = 0.4$
κ	$M\omega$		
Schwarzschild	$0.5993 - 0.0927i$		
ϕ^{2n}	$-$	$0.7294 - 0.07i$	$0.7761 - 0.2286i$
0.001	$-$	$0.7234 - 0.0616i$	$0.7864 - 0.2215i$
0.01	$-$	$0.7236 - 0.0618i$	$0.7863 - 0.2218i$
0.1	$-$	$0.7246 - 0.0635i$	$0.7847 - 0.2238i$
1	$0.508 - 0.0004i$	$0.7329 - 0.0795$	$0.7692 - 0.241i$
2	$0.5308 - 0.0009i$	$0.7378 - 0.095i$	$0.7536 - 0.254i$
10	$0.4338 - 0.00004i$	$0.7311 - 0.1686$	$0.6687 - 0.2957i$
50	$0.6142 - 0.0147i$	$0.6398 - 0.2573i$	$0.5081 - 0.3027i$

5.4 Special family of solutions

5.4.1 Properties of $V_{\rm eff}$

Now, we proceed to the our special family of solutions. In quasi-global coordinates ($B(x) = A^{-1}(x)$) the effective potential $V_{\rm eff}(x,l)$ takes the following form

$$V_{\rm eff}(x,l) = \frac{3A^2}{2}\left(\frac{R'}{R}\right)^2 - \frac{A^2}{2}\frac{R''}{R} - \frac{d}{dr}\left(\frac{A^2}{2}\frac{R'}{R}\right) + A\frac{(l-1)(l+2)}{R^2}, \quad (5.35)$$

Near spatial infinity, the behavior of $V_{\rm eff}$ is the same in the NS and BH cases

$$x^* = x + 2M\ln x + O\left(\frac{1}{x}\right), \quad V(x) = \frac{l(l+1)}{x^2} + O\left(\frac{1}{x^3}\right), \quad V(x^*) \sim \frac{l(l+1)}{x^{*2}}. \quad (5.36)$$

However, the asymptotic behavior near the horizon $x = x_h$ in the BH case and near the center $x = x_0$ in the NS case is drastically different.

The BH case.

In the BH case ($x_0 < 3M$), near the horizon $x = x_h$, we have

$$x^* \sim \frac{1}{A'(x_h)}\ln(x - x_h), \quad V_{\rm eff}(x) \sim q(x_h,l)(x - x_h), \quad (5.37)$$

where we denoted $q(x_h,l) = \left[(l^2 - l - 2) - A'(x_h)R'(x_h)R(x_h)\right]$. If $q(x_h,l) < 0$, there exists a domain (x_h, x_1) where $V_{\rm eff}(x,l) < 0$. On the other hand, $V_{\rm eff}$ is increasing function near x_h ($q(x_h,l) > 0$) or x_1 ($q(x_h,l) < 0$) and decreases as $x \to \infty$. Therefore, there always exists at least one maximum of $V_{\rm eff}$.

We have found that $V_{\rm eff}$, for different values of (x_0, N), can have one or two maxima with or without a negative domain near the horizon. Some typical examples are shown in Fig. 5.12. From Fig. 5.12 (b), it can be observed that the value of the left maximum tends to infinity as $x_0 \to 3M - 0$.

When the effective potential $V_{\rm eff} > 0$ for $r^* \in (-\infty, \infty)$, the corresponding solutions are stable under odd-parity perturbations.

In certain cases, the effective potential $V_{\rm eff}$ becomes negative within a small domain near the horizon, which can signal about the presence of instability. To analyze this cases, it is convenient to use the S–deformation method [131, 137, 138]

As in section 5.1, we denote the operator $\mathcal{H}$ on $L^2(x^*, dx^*)$ as

$$\mathcal{H} = -\frac{d^2}{dx^{*2}} + V_{\rm eff}(x^*,l), \;\; \mathcal{H}\psi = \omega^2\psi, \quad (5.38)$$

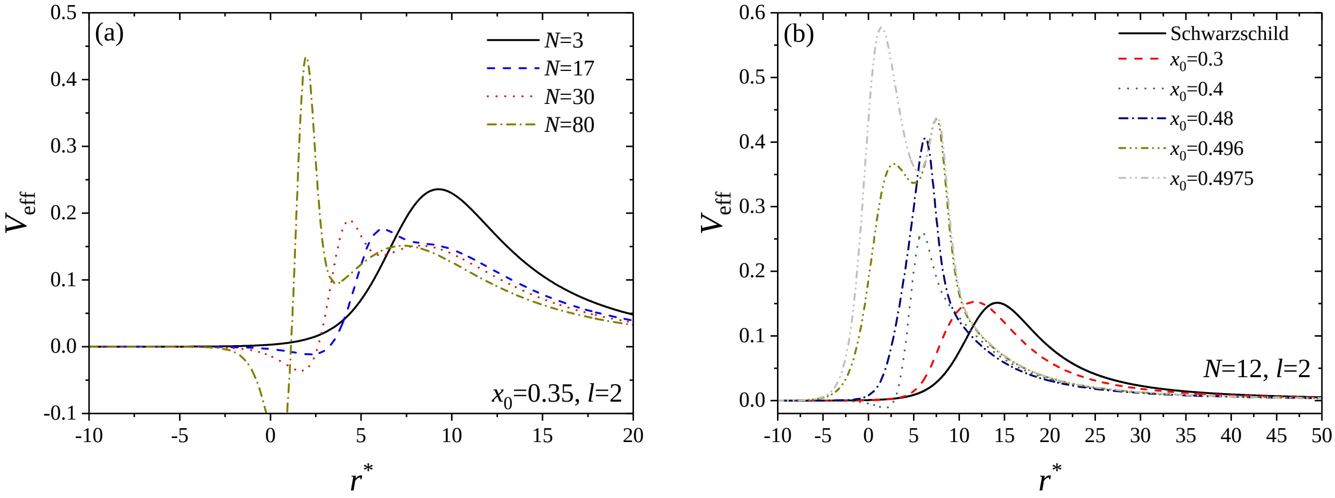

Figure 5.12: The typical behaviour of the effective potentials V_{eff} in the BH case: (a) $x_0 = 0.35$, $l = 2$ for different N (b) $N = 12$, $l = 2$ for different x_0.

where ω is an eigenvalue and ψ is an eigenfunction, respectively.

To prove the stability of our solutions, we need to show that there are no $\omega^2 < 0$ eigenvalues, i.e.,

$$(\psi, \mathcal{H}\psi) = \int_{-\infty}^{\infty} \left[\left| \frac{d\psi}{dx^*} \right|^2 + V_{\text{eff}}(x^*)|\psi|^2 \right] dx^* > 0 \tag{5.39}$$

Then the lowest eigenvalue is $\omega_0 > 0$, implies that solution is stable.

According to the S-deformation method, we can introduce some new smooth function S and deform the derivative and the effective potential terms in the following way

$$(\psi, \mathcal{H}\psi) = \int_{-\infty}^{\infty} \left[|D\psi|^2 + \tilde{V}_{\text{eff}}(x^*)|\psi|^2 \right] dx^*, \tag{5.40}$$

where we denoted

$$D = \frac{d}{dx^*} + S, \;\; \tilde{V}_{\text{eff}} = V_{\text{eff}} + A\frac{dS}{dx} - S^2, \tag{5.41}$$

For convenience, we can regroup terms in (5.35) as

$$V_{\text{eff}} = A^2 \left[\left(\frac{d}{dx} \ln(R) \right)^2 - \frac{d^2}{dx^2} \ln(R) \right] - A'A \left(\frac{d}{dx} \ln(R) \right) + A\frac{(l-1)(l+2)}{R^2}. \tag{5.42}$$

Then, if we select

$$S = A\frac{d}{dx}\ln(R), \tag{5.43}$$

we obtain that

$$\tilde{V}_{\text{eff}}(x) = A(x)\frac{(l-1)(l+2)}{R^2(x)} > 0, \tag{5.44}$$

and

$$(\psi, \mathcal{H}\psi) = \int_{-\infty}^{\infty} |D\psi|^2 dx^* + \int_{x_h}^{\infty} \frac{(l-1)(l+2)}{R^2(x)}|\psi|^2 dx > 0. \tag{5.45}$$

It is evident, that both terms are positive, so $\omega_0^2 > 0$, which implies that our solutions are stable under odd-parity perturbations.

Furthermore, we didn't find any exponentially growing modes in the time-domain profiles $\Psi(t, r^*)$ (see Fig. 5.14).

The NS case. In case of NS ($x_0 \geq 3M$) near the center $x = x_0$, we have that

$$x^* \sim \frac{3R'^2(x-x_0)^2}{4(x_0-3M)}, \quad V_{\text{eff}}(x) \sim \frac{4(x_0-3M)^2}{3R'^4(x-x_0)^4}, \quad V_{\text{eff}}(x^*) \sim \frac{3}{4x^{*2}}. \tag{5.46}$$

and for $x_0 = 3M$

$$x^* \sim R'^2(x_0)(x-x_0), \quad V_{\text{eff}}(x) \sim \frac{l(l+1)}{R'^4(x_0)(x-x_0)^2}, \quad V_{\text{eff}}(x^*) \sim \frac{l(l+1)}{x^{*2}}. \tag{5.47}$$

The solution of the (5.30) near the singularity is given by (5.32) for $x_0 > 3M$. However, for $x_0 = 3M$ we have

$$\psi(x^*) = \sqrt{x^*}\left[C_1 J_{l+\frac{1}{2}}(\omega x^*) + C_2 Y_{l+\frac{1}{2}}(\omega x^*)\right] \sim \tilde{C}_1(x^*)^{l+1} + \tilde{C}_2(x^*)^{-l}. \tag{5.48}$$

The second solution isn't square-integrable near the singularity in the both cases and in order to get a normalized solution we need to require $\tilde{C}_2 = 0$. The operator $\mathcal{H}$ is essentially self-adjoint and there is a unique self-adjoint extension $\mathcal{H}_E$. This extension is defined on the class of functions, that satisfy $\sqrt{x^*}\psi|_{x^*=0} = 0$ for $x_0 > 3M$ and $(x^*)^l\psi|_{x^*=0} = 0$ for $x_0 = 3M$.

The typical examples of the effective potentials are shown in Fig. 5.13. One can observed that these potentials are always positive, and for values of x_0 closer to $x_0 = 3M$, they exhibit the presence of a local maximum. As x_0 increases, this local maximum diminishes, and the profile of the effective potential transforms into a potential wall, which monotonically rises to infinity at the singularity.

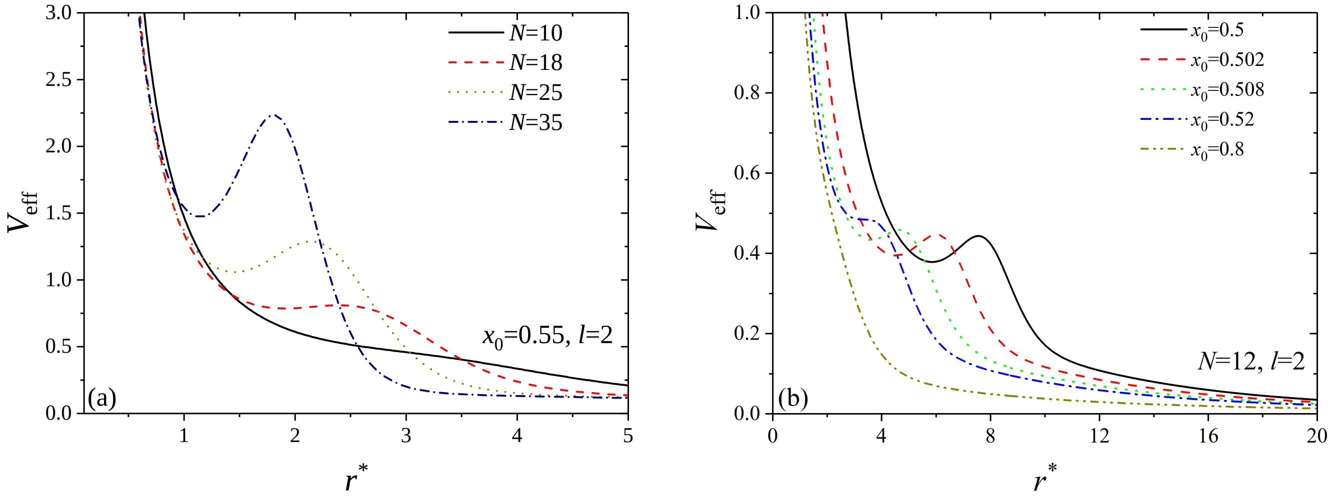

Figure 5.13: The typical behaviour of the effective potentials $V_{\rm eff}$ in the NS case: (a) $x_0 = 0.55$, $l = 2$ for different N (b) $N = 12$, $l = 2$ for different x_0.

5.4.2 Quasi-normal modes

We solve the master wave equation (5.16) for the different sets of parameters, and extract the fundamental quasi-normal frequencies from the obtained time-domain profiles. The typical examples of the time-domain profiles are shown in Figs. 5.14–5.15. The exact values of fundamental QNM frequencies are given in Tabs 5.7–5.10 and in Figs. 5.16–5.17.

One intriguing feature that can be observed in the time-domain profiles in the black hole case is the presence of echoes (see Fig. 5.14 (c)). In [139], it was demonstrated that such echoes appear due to the presence of additional local maxima of the effective potential $V_{\rm eff}$. In the NS case we also can observe echoes (see Fig. 5.15 (c)), but their nature is related to the absence of a horizon.

From 5.14–5.15 we can observe that $\omega(x_0)$ curves in the (ω_R, ω_I) planes exhibit discontinuities as functions of x_0 and can be represented by multiple disjointed branches. Their behavior can be described as follows.

For $x_0 < x_0^{(1)}$, there exists a single branch (labeled as A, Fig. 5.16) in the (ω_R, ω_I) plane, starting from the QNM value of the Schwarzschild BH.

At $x_0 = x_0^{(1)}$, a jump occurs to another branch (labeled as B) with $\omega_I(x_0^{(1)} - 0) = \omega_I(x_0^{(1)} + 0)$ and $\omega_R(x_0^{(1)} - 0) \neq \omega_R(x_0^{(1)} + 0)$. This new branch ($B$) remains continuous for x_0 in the range $(x_0^{(1)}, x_0^{(2)})$ until $x_0 = x_0^{(2)}$, where a similar jump occurs to a new branch (labeled as C).

A similar situation also occurs for the $\omega(N)$ curves, as shown in Fig. 5.17. The presence of these discontinuities is related to the emergence of concurrent frequencies with very close values of $\text{Im}(\omega)$ for the fundamental and first overtones modes, respectively.

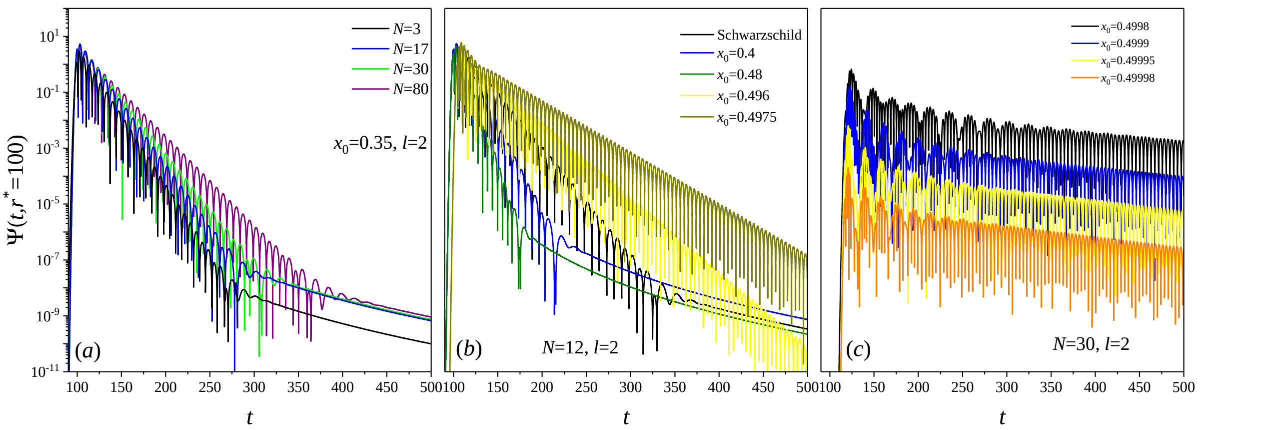

Figure 5.14: The time-domain profiles in the BH case for different values of parameters. In panel (c), we can observe the presence of echoes, which align at later times near critical case $x_0 = 3M - 0$.

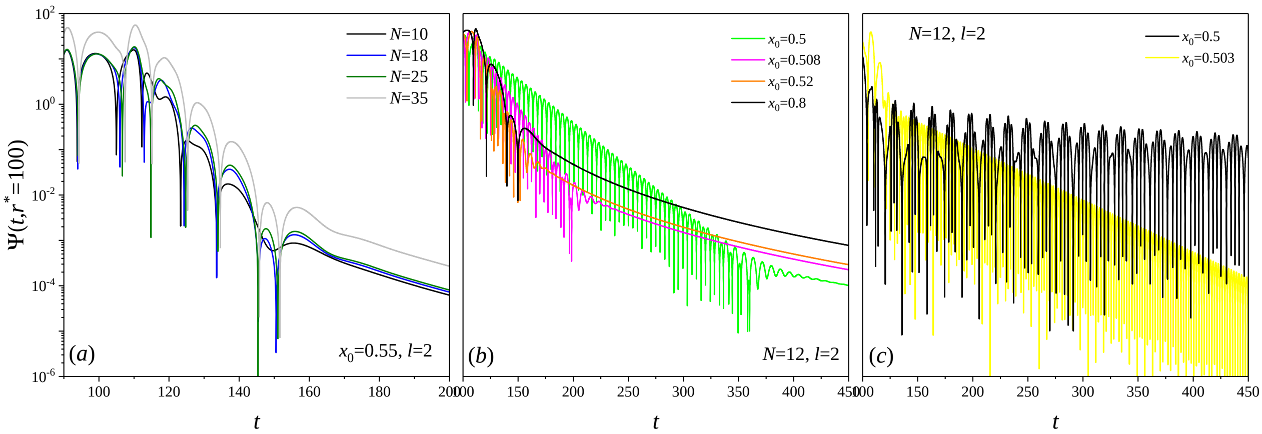

Figure 5.15: The time-domain profiles in the NS case for different values of parameters. In panel (c), we can observe the presence of echoes from the NS near critical value $x_0 = 3M + 0$.

The QNM frequencies remain continuous during the transition from the BH case to NS case in case of the our specific family of solutions. For instance, in the Reissner-Nordström space-time, they are discontinued [140].

Table 5.7: The values of the fundamental QNM frequencies in the BH case with $l = 2$.

N/x_0	0.2	0.35	0.45	0.495
Schwarzschild	$0.3737 - 0.08901i$			
2	$0.4198 - 0.1009i$	$0.586 - 0.1382i$	$1.222 - 0.2849i$	–
3	$0.3883 - 0.0943i$	$0.4655 - 0.1137i$	$0.7389 - 0.1636i$	–
6	$0.3757 - 0.0901i$	$0.4052 - 0.1126i$	$0.5025 - 0.1322i$	$0.7384 - 0.209i$
10	$0.374 - 0.08902i$	$0.4001 - 0.1105i$	$0.4595 - 0.2037i$	$0.6657 - 0.06111i$
15	$0.3737 - 0.08897i$	$0.4037 - 0.105i$	$0.3988 - 0.1978i$	$0.6099 - 0.1381i$
20	$0.3737 - 0.08898i$	$0.4072 - 0.09978i$	$0.3946 - 0.1938i$	$0.3582 - 0.2219i$
30	$0.3737 - 0.08898i$	$0.4119 - 0.09162i$	$0.3937 - 0.1932i$	$0.3622 - 0.216i$
40	$0.3737 - 0.08898i$	$0.415 - 0.08574i$	$0.3941 - 0.1937i$	$0.3626 - 0.2143i$

Table 5.8: The values of the fundamental QNM frequencies in the NS case with $l = 2$.

N/x_0	0.5	0.505	0.51	0.6
Schwarzschild	$0.3737 - 0.08901i$			
2	–	–	–	–
3	–	–	–	–
6	$0.7362 - 0.2425i$	$0.7424 - 0.2601i$	$0.269 - 0.2852i$	–
10	$0.7593 - 0.1028i$	$0.7944 - 0.1432i$	$0.8188 - 0.1756i$	$0.2612 - 0.2342i$
15	$0.7647 - 0.04536i$	$0.8565 - 0.0918i$	$0.9124 - 0.128i$	$0.2796 - 0.2272i$
20	$0.7677 - 0.0233i$	$0.9247 - 0.0702i$	$1.01 - 0.1076i$	$0.2866 - 0.2254i$
30	$0.7704 - 0.0085i$	$1.071 - 0.0521i$	$1.21 - 0.0896i$	$0.2918 - 0.2242i$
40	$0.7711 - 0.0041i$	$1.219 - 0.0444i$	$1.407 - 0.0813i$	$0.2937 - 0.2239i$

Table 5.9: The values of the fundamental QNM frequencies in the BH case with $l = 3$.

N/x_0	0.2	0.35	0.45	0.495
Schwarzschild	$0.5995 - 0.09274i$			
2	$0.6696 - 0.1039i$	$0.9287 - 0.1425i$	$1.948 - 0.2986i$	–
3	$0.6191 - 0.0966i$	$0.7289 - 0.113i$	$1.162 - 0.1742i$	–
6	$0.6012 - 0.0933i$	$0.6325 - 0.1075i$	$0.7422 - 0.1128i$	$0.9348 - 0.2797i$
10	$0.5997 - 0.0927i$	$0.6232 - 0.106i$	$0.6917 - 0.1533i$	$0.9169 - 0.0769i$
15	$0.5995 - 0.0927i$	$0.6245 - 0.0995i$	$0.6587 - 0.2049i$	$0.8201 - 0.08333i$
20	$0.5995 - 0.0927i$	$0.6262 - 0.0929i$	$0.6338 - 0.2061i$	$0.8026 - 0.1676i$
30	$0.5995 - 0.0927i$	$0.6276 - 0.0822i$	$0.626 - 0.2049i$	$0.5826 - 0.2422i$
40	$0.5995 - 0.0927i$	$0.6279 - 0.0742i$	$0.625 - 0.2052i$	$0.5836 - 0.2377i$

Table 5.10: The values of the fundamental QNM frequencies in the NS case with $l = 3$.

N/x_0	0.5	0.505	0.51	0.6
Schwarzschild	$0.5995 - 0.09274i$			
2	–	–	–	–
3	$0.1459 - 0.2998i$	$0.1418 - 0.4282i$	$0.2364 - 0.6414i$	–
6	$0.9237 - 0.3023i$	$0.9223 - 0.3226i$	$0.9154 - 0.3415i$	$0.372 - 0.3471i$
10	$0.9538 - 0.1316i$	$0.974 - 0.1667i$	$0.989 - 0.1961i$	$0.4387 - 0.2904i$
15	$0.9578 - 0.06i$	$1.022 - 0.1027i$	$1.065 - 0.137i$	$0.4662 - 0.27i$
20	$0.96 - 0.0316i$	$1.077 - 0.0763i$	$1.148 - 0.1125i$	$0.477 - 0.2634i$
30	$0.963 - 0.0117i$	$1.202 - 0.0547i$	$1.325 - 0.0916i$	$0.4852 - 0.2593i$
40	$0.9638 - 0.0057i$	$1.335 - 0.0457i$	$1.507 - 0.0824i$	$0.4883 - 0.2581i$

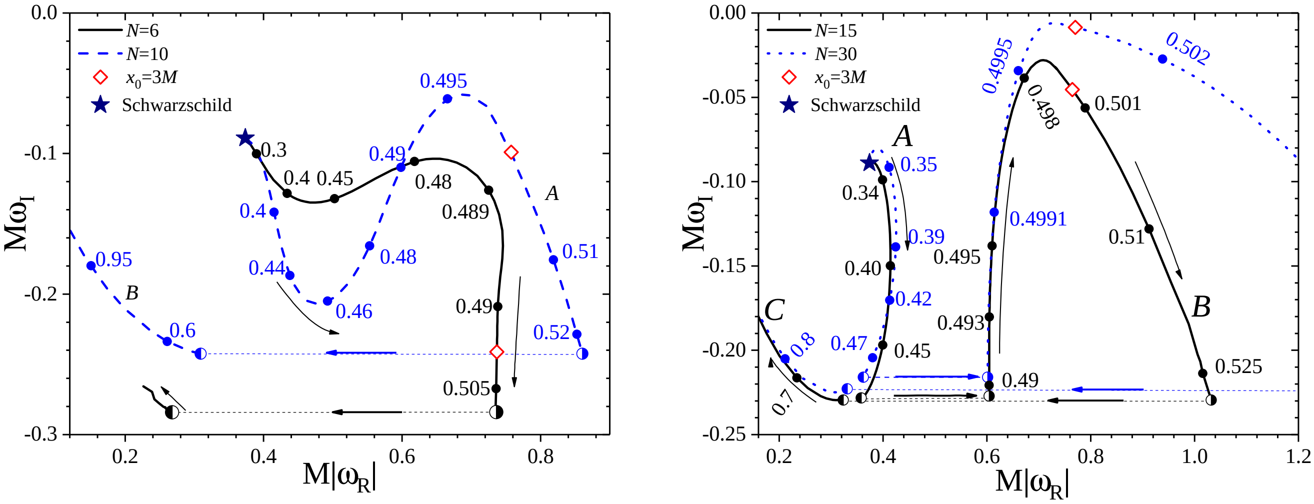

Figure 5.16: The trajectories of the fundamental frequencies with $l = 2$ in the (ω_R, ω_I) plane as functions of x_0 for different values of N. The arrows indicate the direction of increasing x_0.

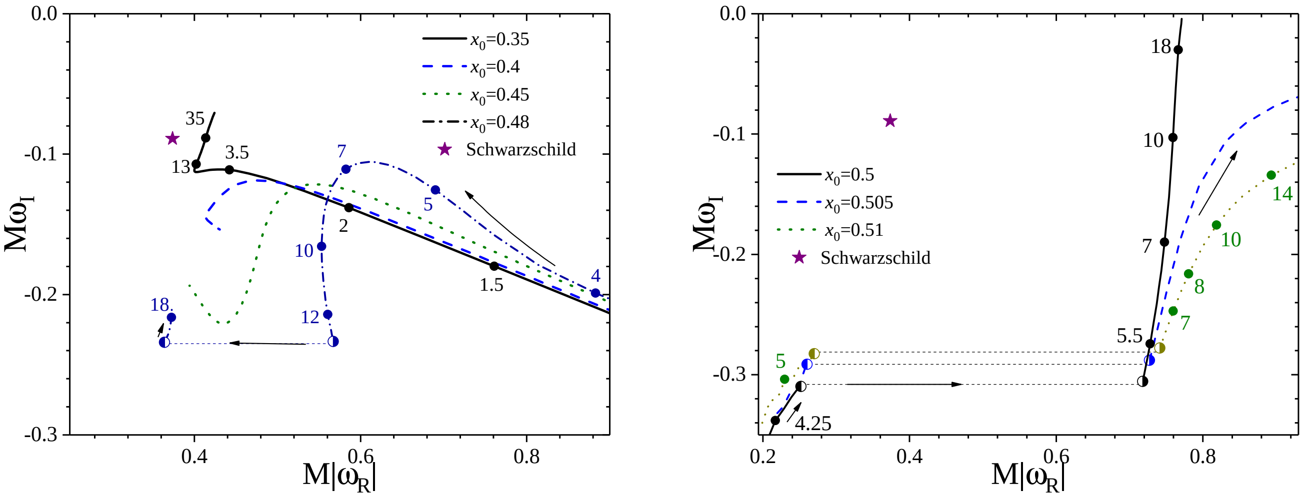

Figure 5.17: The trajectories of the fundamental frequencies with $l = 2$ in the (ω_R, ω_I) plane as functions of N for different values of x_0. The arrows indicate the direction of increasing N.

5.5 Stability and quasi-normal modes of Kehagias-Sfetsos naked singularity

In this section, we study the evolution of scalar, electromagnetic, and Dirac test fields in the background of a naked singularity described by the following metric

$$ds^2 = f(r)dt^2 - \frac{1}{f(r)}dr^2 - r^2 d\Omega^2, \tag{5.49}$$

with

$$f(r) = 1 + \frac{r^2}{2\alpha}\left(1 - \sqrt{1 + \frac{8\alpha M}{r^3}}\right), \tag{5.50}$$

where α is a positive constant and M is a mass of the configuration, respectively. This space-time metric naturally appears in 4D Einstein-Gauss-Bonnet novel gravity [141, 142] and Horava gravity [143] (known as the Kehagias-Sfetsos solution).

We can perform a rescaling $r \to r/M$ and introduce a dimensionless constant $\gamma = \alpha/M^2$. In dependence of value on the value of γ, we have different configuration types. For $\gamma \in (0, 1]$, we have a black hole with horizon radii given by

$$r_{h,\pm} = 1 \pm \sqrt{1 - \gamma}, \tag{5.51}$$

On the other hand, for $\gamma \in (1, \infty)$, we obtain a naked singularity.

The (in)stability and QNM spectrum of the black hole solution have been investigated in [144–147].

As for the naked singularity solution, an earlier analysis was conducted in [148] examining perturbations by scalar, electromagnetic, and Dirac test fields in the linear regime. The authors reported instability of this space-time for multipole numbers l greater than 1. However, we find their results to be erroneous. Therefore, we need to revisit their results and demonstrate that the test fields are stable in all cases.

5.5.1 Equations for test fields

In the general case, the covariant equations of motion for the test fields have the following forms

(a) For a massless scalar field, the equation of motion is given by

$$\frac{1}{\sqrt{-g}}\partial_\mu \left(\sqrt{-g} g^{\mu\nu}\partial_\nu \Psi\right) = 0, \tag{5.52}$$

(b) For an electromagnetic field, the equation of motion is given by

$$\frac{1}{\sqrt{-g}}\partial_\mu\left(F_{\rho\sigma}g^{\rho\nu}g^{\sigma\mu}\sqrt{-g}\right)=0\,, \tag{5.53}$$

where $F_{\rho\sigma}=\partial_\rho A_\sigma-\partial_\sigma A_\rho$ is the electromagnetic tensor and A_μ is the vector potential.

(c) For the Dirac field, we have massless Dirac equation [149]

$$[\gamma^\mu(\partial_\mu-\Gamma_\mu)]\Psi=0, \tag{5.54}$$

where γ^a are noncommutative γ matrices and Γ_μ represent the spin connection in the tetrad formalism.

After separating the angular variables, we can rewrite (5.52, 5.53, 5.54) in the form of the single master wave equation

$$\left(\frac{\partial^2}{\partial t^2}-\frac{\partial^2}{\partial r^{*2}}\right)\Psi_i(t,r^*)+V_{\text{eff}}^{(i)}(r,l)\Psi_i(t,r^*)=0, \tag{5.55}$$

where the index $i=(S,V,D)$ corresponds to scalar, vector, and Dirac fields, respectively. The "tortoise" coordinate r^* is defined as $dr^*=dr/f(r)$, and the effective potentials $V_{\text{eff}}^{(i)}$ are

$$V_{\text{eff}}^{(S)}(r)=f(r)\left(\frac{\ell(\ell+1)}{r^2}+\frac{1}{r}\frac{df(r)}{dr}\right), \tag{5.56}$$

$$V_{\text{eff}}^{(V)}(r)=f(r)\frac{\ell(\ell+1)}{r^2}, \tag{5.57}$$

$$V_{\text{eff}}^{(D)}(r)=f(r)\frac{l+1}{r}\Big(\frac{l+1}{r}\mp\sqrt{f(r)}\pm\frac{d}{dr}\sqrt{f(r)}\Big), \tag{5.58}$$

where $l=0,1,2,...$ is the angular momentum number. For the scalar and Dirac fields, we have $l\geq 0$, and for the vector field, we have $l\geq 1$.

In the case of the Dirac field, the effective potentials with opposite signs are iso-spectral and can be transformed into each other using the Darboux transformation.

The asymptotics of the corresponding functions near the singularity $r=0$ have the following form

$$r^*=r+\frac{2}{3}\sqrt{\frac{2}{\gamma}}r^{3/2}+O(r^2),\quad V_{\text{eff}}^{(i)}(r)=\frac{l(l+1)}{r^2}+O\left(\frac{1}{r^{3/2}}\right),\quad l>0. \tag{5.59}$$

and for $l=0$ we have

$$V_{\text{eff}}^{(S)}(r)=-\frac{1}{\sqrt{2\gamma}r^{3/2}}+O\left(\frac{1}{r}\right),\quad V_{\text{eff}}^{(D)}(r)=\frac{1}{2\sqrt{2\gamma}r^{3/2}}+O\left(\frac{1}{r}\right). \tag{5.60}$$

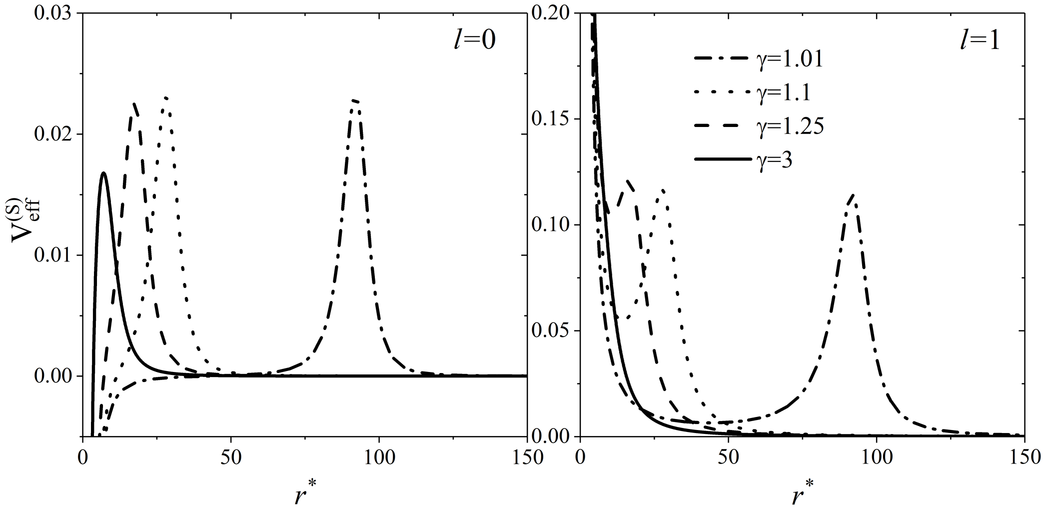

Figure 5.18: The typical behaviour of the effective potentials $V_{\rm eff}^{(S)}$ of the scalar field with $l = 0$ (left panel) and $l = 1$ (right panel) for different values of γ.

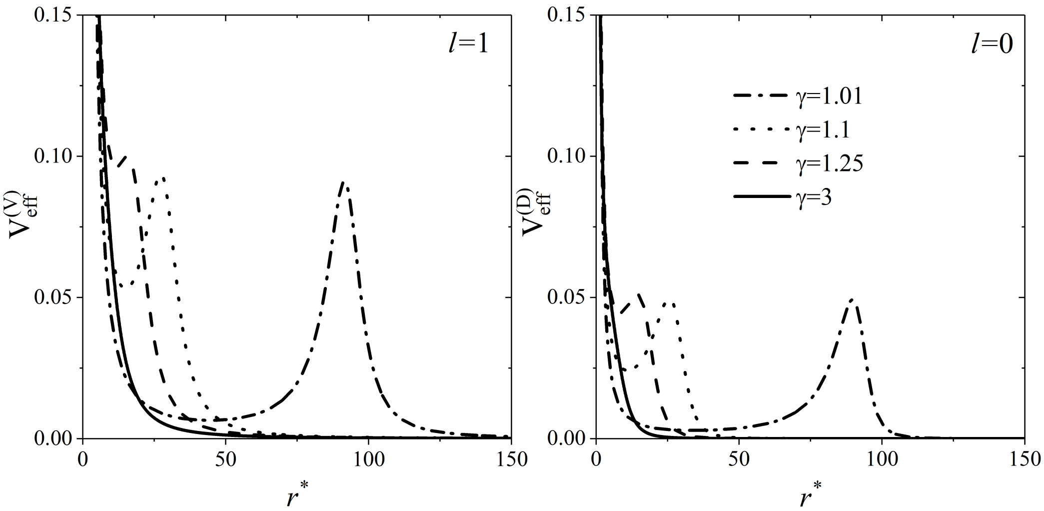

Figure 5.19: The typical behaviour of the effective potentials $V_{\rm eff}^{(V)}$ with $l = 1$ (left panel) and $V_{\rm eff}^{(D)}$ with $l = 0$ of the vector and Dirac fields, respectively.

For arbitrary l, the effective potentials $V_{\rm eff}^{(i)} \to +\infty$ as $r \to 0$, except the case of the scalar field with $l = 0$, where $V_{\rm eff}^{(S)} \to -\infty$. Their behaviour is illustrated in Figs. 5.18, 5.19.

In general, the effective potentials $V_{\rm eff}^{(i)}$ are positive for all cases, except for the scalar field with $l = 0$, where we have a negative gap near the singularity. Additionally, all the effective potentials exhibit a peak that shifts to the left as γ increases, eventually disappearing. In the special case of the scalar field with $l = 0$, the peak is always exists for all values of γ. For $V_{\rm eff}^{(V)}$ the peak exists when $\gamma < 3\sqrt{3}/4$. Unfortunately, the explicit formulas are unattainable in all other cases.

After substituting $\Psi(t, r^*) = \psi(r^*)e^{-i\omega t}$ into equation (5.55), we obtain (5.30) near the singularity for $l \geq 1$

$$\psi_i''(r^*) + \left(\omega^2 - V_{\text{eff}}^{(i)}(r, l)\right)\psi_i(r^*) = 0, \tag{5.61}$$

and the corresponding solution is

$$\psi_i(r^*) \sim \tilde{C}_1(r^*)^{l+1} + \tilde{C}_2(r^*)^{-l}. \tag{5.62}$$

The second solution isn't square-integrable near the singularity for both cases, The operator $\mathcal{H}$ is essentially self-adjoint and there is a unique self-adjoint extension $\mathcal{H}_E$. This extension is defined on the class of functions, that satisfy $(x^*)^l\psi|_{x^*=0} = 0$ for $l > 0$.

In special case with $l = 0$ for the Dirac and scalar fields, we have

$$\psi_i(r^*) \sim \tilde{C}_1 r^* + \tilde{C}_2, \tag{5.63}$$

which means that both modes are regular and square integrable near the singularity. Then due to the Weyl's limit point-limit circle criterion and $\mathcal{H}$ is not essentially self-adjoint.

As previously discussed, the positivity of the effective potentials leads to the stability of the corresponding space-time. However, the scalar field case with $l = 0$ indeed requires some additional investigation.

To study the stability in the case of the scalar field with $l = 0$, we can again apply the S–deformation method that we utilized in the previous section. To rewrite $(\psi, \mathcal{H}\psi)$ in the deformed form, we need to ensure $\tilde{C}_2 = 0$ in (5.63), i.e., $\psi_S \sim r^*$ near the singularity. Then, the deformed effective potential $\tilde{V}_{\text{eff}}$ (5.41) has the form

$$\tilde{V}_{\text{eff}} = \frac{ff'}{r} + f\frac{dS}{dr} - S^2. \tag{5.64}$$

If we choose

$$S = -\frac{f}{r}, \tag{5.65}$$

then, we have

$$(\psi, \mathcal{H}\psi) = \int |D\psi|^2 dr^*. \tag{5.66}$$

Thus, $\omega_0^2 > 0$. We also didn't observe the exponentially-growing modes in the time-domain profiles.

5.5.2 Quasi-normal modes

The typical examples of numerical solutions of the (5.55) are shown in Figs. 5.20, 5.22, 5.24. In each case, we observe the emergence of a series of echoes, when γ is closer to 1. Increasing γ leads to a decrease in the time interval between distinct echoes and the time when the typical ringdown appears. Starting from a specific γ value, the echoes finally disappear from the time-domain profiles. It is difficult find QNM for small values of γ due to very long echoes time, which requires enormous lengthy time interval.

For sufficiently large values of γ, the local peak of the effective potential vanishes, and the number of Ψ oscillations diminishes, transforming the ring-down into a "single-wave" profile with a power-law tail. In such cases, it is difficult, if not impossible, to extract frequencies with adequate accuracy.

The typical dependencies of the fundamental QNM as functions of γ for different values of l are shown in Figs. 5.21, 5.23, 5.25 and the exact values of ω are given in Tabs. 5.11–5.13.

As we can see in Figs. 5.21– 5.25, the ω curves have a crescent-like shape, similar to the curves in sections 5.2, 5.3. The $\omega_R(\gamma)$ and $\omega_I(\gamma)$ dependencies are non-monotonic, consisting of a maximum for the real part and a minimum for the imaginary part of the frequency ω. It should be noted that the maximal value of ω_R in the scalar field case shifts left with increasing l and shifts right in other cases. In all cases, the values of ω differ from the corresponding values in the Schwarzschild black hole case. However, we can also observe an interesting situation, when the ω_{schw} values are close to the ω_{NS} values for different l values. For instance, in the case of the scalar field, we have $M\omega_{schw} = 0.675 - 0.0965i$ for $l = 3$ and $M\omega_{NS} = 0.669 - 0.0963i$ for $l = 2$.

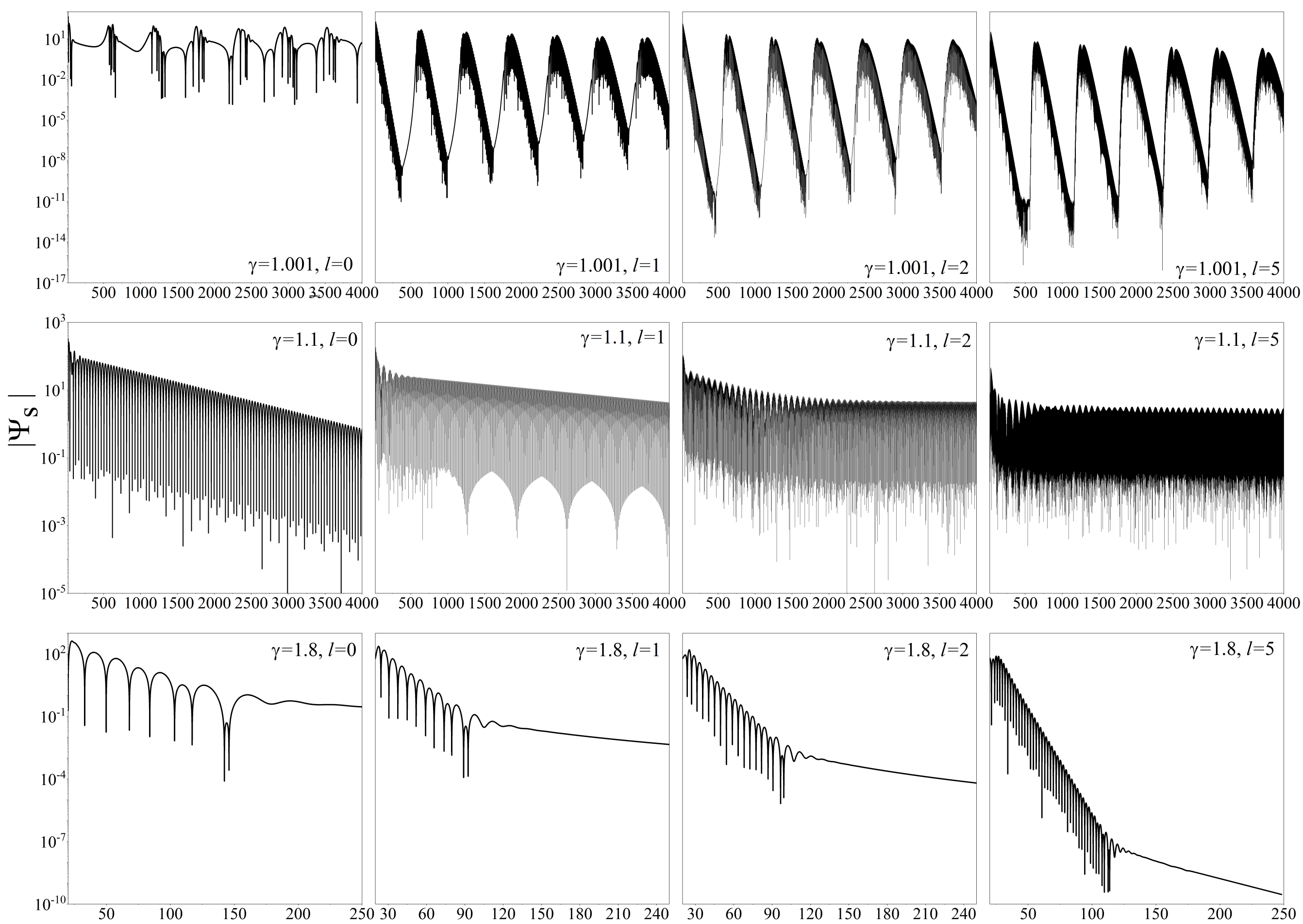

Figure 5.20: The typical examples of the time-domain profiles in the case of the scalar field for different values of l and γ.

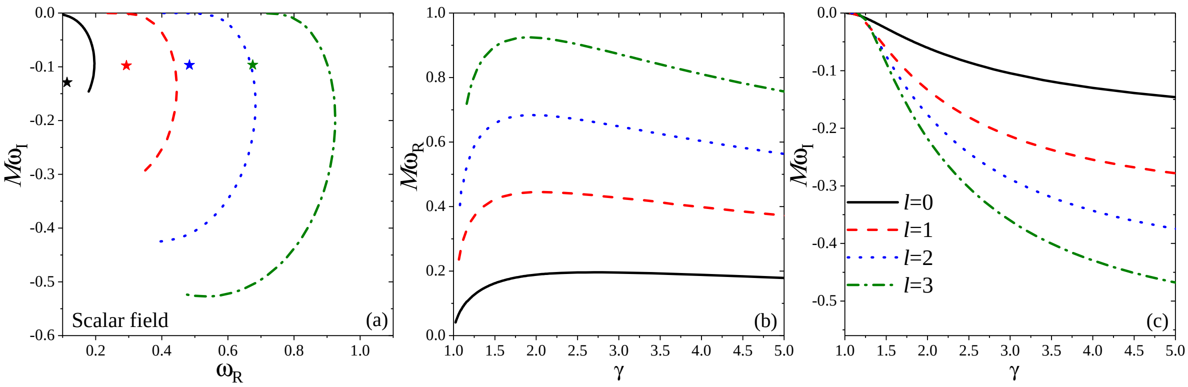

Figure 5.21: The dependencies of the values of the fundamental QNM in the case for the scalar field for different values of l and γ. For $l = 0$, we can observe that $\omega_I < 0$, which corresponds to stability. The colored stars represent the values of ω in the case of a Schwarzschild black hole.

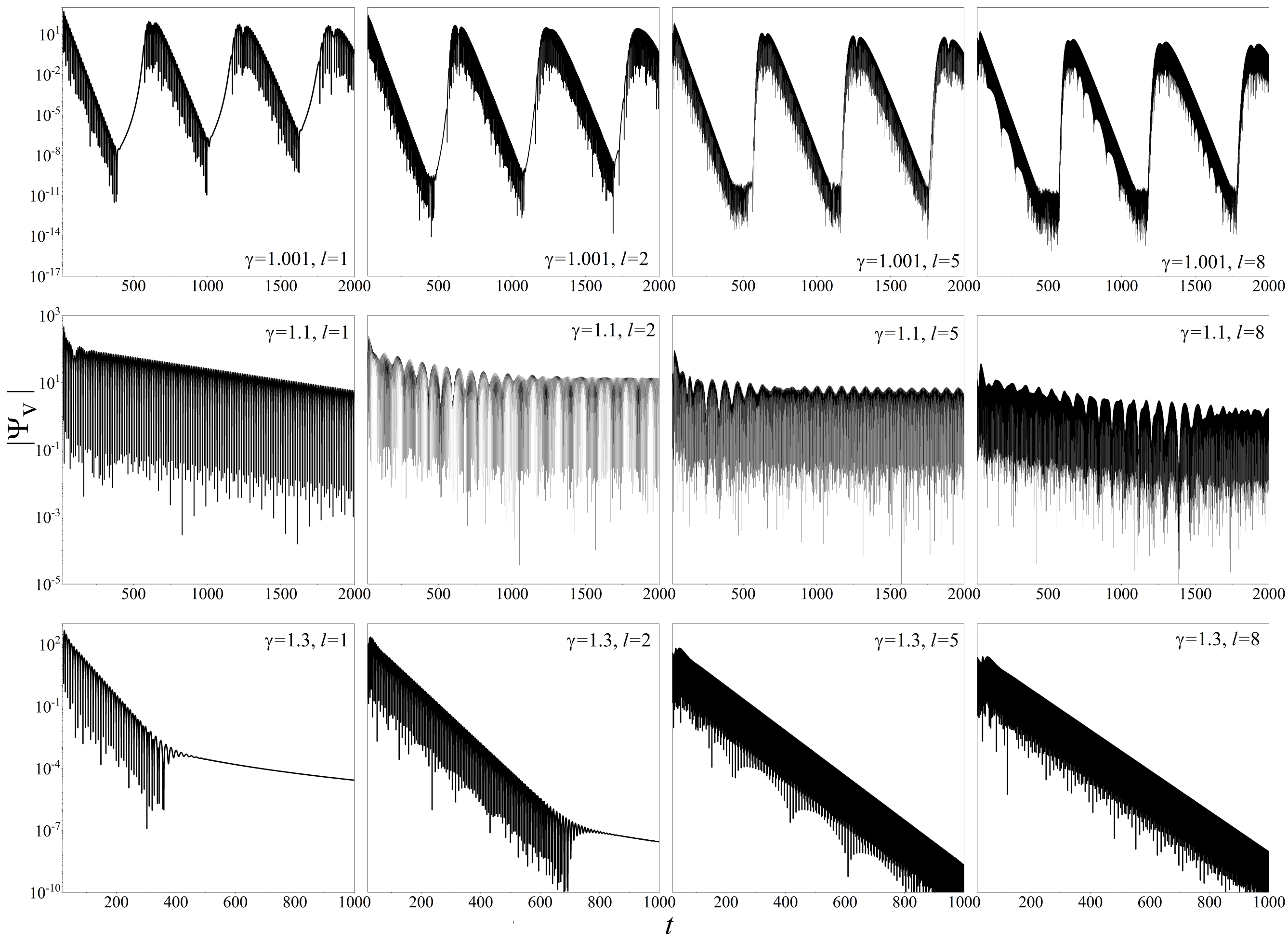

Figure 5.22: The typical examples of the time-domain profiles in the case of the vector field for different values of l and γ.

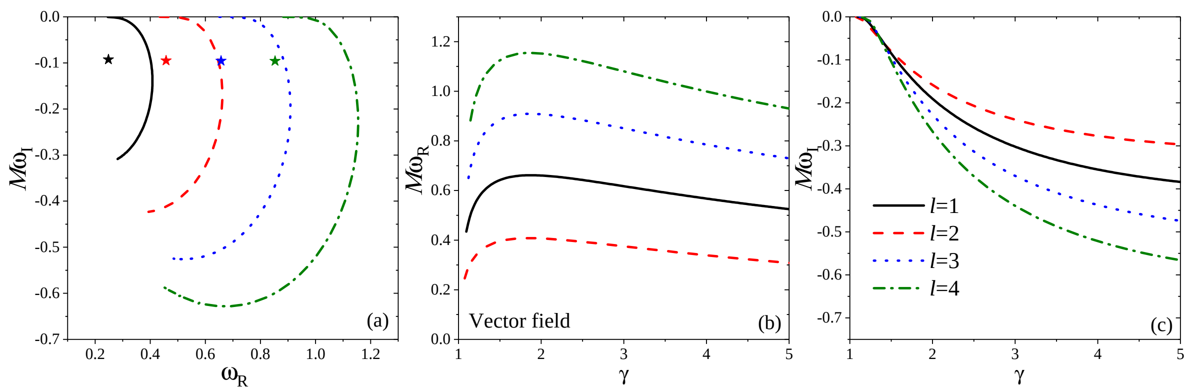

Figure 5.23: The dependencies of the values of the fundamental QNM in the case for the vector field for different values of l and γ. The colored stars represent the values of ω in the case of a Schwarzschild black hole.

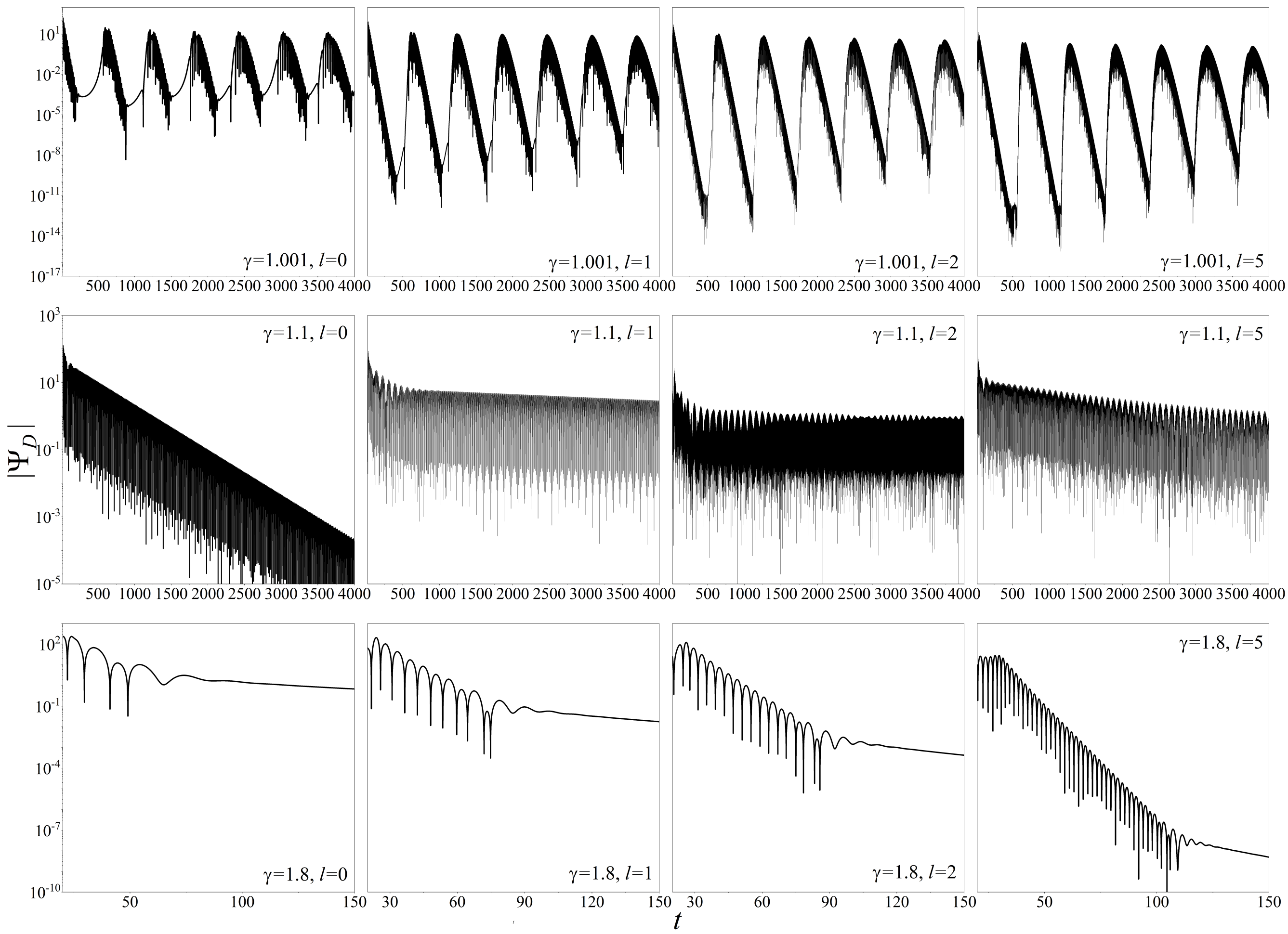

Figure 5.24: The typical examples of the time-domain profiles in the case of the Dirac field for different values of l and γ.

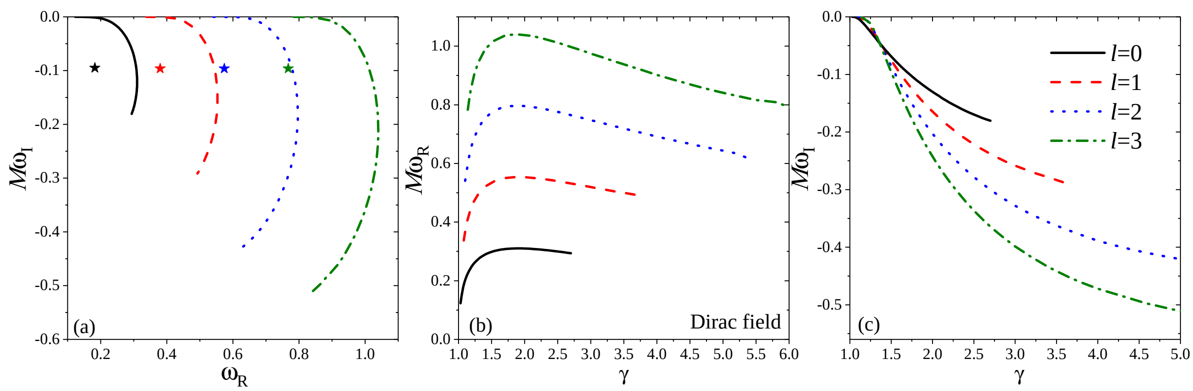

Figure 5.25: The dependencies of the values of the fundamental QNM in the case for the Dirac field for different values of l and γ. The colored stars represent the values of ω in the case of a Schwarzschild black hole.

Table 5.11: The fundamental QNM frequencies in case of the scalar field for different values of γ.

Scalar field				
γ	$l = 0$	$l = 1$	$l = 2$	$l = 3$
Schwarzschild	$0.1105 - 0.1049i$	$0.2929 - 0.0977i$	$0.4836 - 0.0968i$	$0.6754 - 0.0965i$
1.05	$0.059 - 0.0003i$	$0.2107 - 0.00001i$	–	–
1.1	$0.0846 - 0.0014i$	$0.28 - 0.0005i$	$0.4462 - 0.00004i$	–
1.15	$0.1022 - 0.0033i$	$0.3217 - 0.0032i$	$0.5136 - 0.0009i$	$0.7045 - 0.0002i$
1.2	$0.1164 - 0.0058i$	$0.3496 - 0.0088i$	$0.55683 - 0.0054i$	$0.7646 - 0.003i$
1.25	$0.1269 - 0.0087i$	$0.3699 - 0.0164i$	$0.5867 - 0.0138i$	$0.8045 - 0.0114i$
1.35	$0.1443 - 0.0154i$	$0.3977 - 0.034i$	$0.6257 - 0.0368i$	$0.8549 - 0.0389i$
1.5	$0.1623 - 0.0265i$	$0.4219 - 0.0609i$	$0.658 - 0.0744i$	$0.8955 - 0.0865i$
1.65	$0.1741 - 0.0375i$	$0.4349 - 0.0857i$	$0.6742 - 0.1094i$	$0.915 - 0.1316i$
1.8	$0.1821 - 0.0478i$	$0.4416 - 0.1078i$	$0.6815 - 0.1406i$	$0.923 - 0.1717i$
2	$0.1889 - 0.0603i$	$0.4449 - 0.1331i$	$0.6834 - 0.1763i$	$0.9238 - 0.2177i$
2.5	$0.1957 - 0.0858i$	$0.4395 - 0.1809i$	$0.6704 - 0.243i$	$0.9033 - 0.303i$
3	$0.1956 - 0.1046i$	$0.4269 - 0.2138i$	$0.6486 - 0.2881i$	$0.8726 - 0.3601i$

Table 5.12: The fundamental QNM frequencies in case of the vector field for different values of γ.

Vector field				
γ	$l = 1$	$l = 2$	$l = 3$	$l = 4$
Schwarzschild	$0.2483 - 0.0925i$	$0.4576 - 0.095i$	$0.6569 - 0.0956i$	$0.8531 - 0.0959i$
1.05	$0.2084 - 0.00004i$	–	–	–
1.1	$0.273 - 0.0015i$	$0.443 - 0.00008i$	–	–
1.15	$0.3102 - 0.0072i$	$0.5074 - 0.0017i$	$0.7006 - 0.0003i$	$0.892 - 0.000065i$
1.2	$0.3349 - 0.0161i$	$0.5485 - 0.008i$	$0.7585 - 0.0041i$	$0.968 - 0.0021i$
1.25	$0.3528 - 0.0266i$	$0.576 - 0.0184i$	$0.7968 - 0.014i$	$1.017 - 0.0111i$
1.35	$0.3766 - 0.0487i$	$0.6126 - 0.0443i$	$0.8454 - 0.0438i$	$1.0774 - 0.0444i$
1.5	$0.3959 - 0.0801i$	$0.6421 - 0.0847i$	$0.8839 - 0.094i$	$1.1247 - 0.1037i$
1.65	$0.4047 - 0.1077i$	$0.6558 - 0.1216i$	$0.9017 - 0.1399i$	$1.1463 - 0.1598i$
1.8	$0.4078 - 0.1316i$	$0.661 - 0.1538i$	$0.9083 - 0.1809i$	$1.154 - 0.2096I$
2	$0.4068 - 0.1584i$	$0.6604 - 0.1904i$	$0.9073 - 0.2275i$	$1.1522 - 0.2663i$
2.5	$0.3933 - 0.2071i$	$0.6425 - 0.258i$	$0.8834 - 0.3131i$	$1.1217 - 0.3705i$
3	$0.3749 - 0.2391i$	$0.6173 - 0.302i$	$0.8502 - 0.369i$	$1.0802 - 0.4394i$

Table 5.13: The fundamental QNM frequencies in case of the Dirac field for different values of γ.

Dirac field				
γ	$l = 0$	$l = 1$	$l = 2$	$l = 3$
Schwarzschild	$0.183 - 0.097i$	$0.38 - 0.0964i$	$0.5741 - 0.0963i$	$0.7674 - 0.0963i$
1.05	$0.1543 - 0.0003i$	–	–	–
1.1	$0.2016 - 0.0031i$	$0.3672 - 0.0002i$	$0.541 - 0.00002i$	$0.6946 - 0.0000005i$
1.15	$0.2297 - 0.0093i$	$0.42 - 0.0026i$	$0.6109 - 0.0006i$	$0.8012 - 0.0001i$
1.2	$0.249 - 0.0173i$	$0.4539 - 0.0091i$	$0.66114 - 0.005i$	$0.8691 - 0.0026i$
1.25	$0.2632 - 0.0261i$	$0.4778 - 0.0186i$	$0.695 - 0.0144i$	$0.9133 - 0.0115i$
1.35	$0.2825 - 0.0439i$	$0.5093 - 0.0411i$	$0.7383 - 0.0412i$	$0.9683 - 0.0422i$
1.5	$0.2986 - 0.0687i$	$0.5351 - 0.0754i$	$0.7731 - 0.0852i$	$1.0117 - 0.0959i$
1.65	$0.3065 - 0.0904i$	$0.5475 - 0.1065i$	$0.7894 - 0.126i$	$1.0317 - 0.1465i$
1.8	$0.3097 - 0.1092i$	$0.5526 - 0.1337i$	$0.7957 - 0.162i$	$1.0391 - 0.1914i$
2	$0.3099 - 0.1302i$	$0.553 - 0.1645i$	$0.7955 - 0.2029i$	$1.0381 - 0.2425i$
2.5	–	$0.5395 - 0.2212i$	$0.7758 - 0.2781i$	$1.0117 - 0.3364i$
3	–	$0.5195 - 0.2588i$	$0.7477 - 0.328i$	$0.9751 - 0.3985i$

Chapter 6

Test particle motion and observational properties

6.1 Basic relations

An important question dealing with observational properties of the naked singularities is connected with the motion of particles in the vicinity of such objects. One of the problems that arise here concerns the distribution of stable circular orbits (SCOs) that form the thin accretion disk (Keplerian AD). We will assume that the AD is described by the Novikov-Thorne model [150, 151]. According to this model, the AD is a geometrically thin, but optically thick disk composed of gas particles that move along circular orbits without back-reaction on the background metric.

6.1.1 Circular geodesics

The equations of geodesic motion of a test particle can be derived from the action

$$S = \int d\tau \left[g_{\mu\nu} \dot{x^\mu} \dot{x^\nu} \right], \tag{6.1}$$

where τ is a canonical parameter along geodesic and $\dot{x^\mu}$ are corresponding tangent vectors.

We consider static spherically-symmetric space-times with line element,

$$ds^2 = A(r)dt^2 - B(r)dr^2 - R^2(r)(d\theta^2 + \sin^2\theta d\varphi^2). \tag{6.2}$$

Due to the high symmetry of the space-time, we can restrict ourselves to considering particle motion only in the equatorial plane. Therefore, we can fix $\theta = \pi/2$ and $\dot{\theta} = 0$. The space-time described by (6.2) possesses two Killing vectors ξ_t and ξ_ϕ, associated with time translation and rotation, respectively. These vectors provide us two integrals of motion

$$A(r)\left(\frac{dt}{d\tau}\right) = E, \quad R^2(r)\left(\frac{d\varphi}{d\tau}\right) = L, \tag{6.3}$$

where E and L are the energy and angular momentum, respectively. From Eq. (6.1), we can also obtain an additional integral of motion

$$A(r)\left(\frac{dt}{d\tau}\right)^2 - B(r)\left(\frac{dr}{d\tau}\right)^2 - R^2(r)\left(\frac{d\varphi}{d\tau}\right)^2 = S\,, \tag{6.4}$$

where $S = 0$ in case of photons and $S = 1$ for the massive particles.

From (6.3, 6.4) we obtain

$$AB\left(\frac{dr}{d\tau}\right)^2 = E^2 - U_{\text{eff}}(r, L, S),\ U_{\text{eff}}(r, L, S) = A\left(S + \frac{L^2}{R^2}\right). \tag{6.5}$$

Therefore, we reduced our problem to problem of the one-dimensional particle motion in the field of some effective potential U_{eff}. As we noted before, our main interest lies in studying the stable circular orbit distribution (SCOD) around the compact object. The circular orbit can be determined by the conditions

$$\frac{dr}{d\tau} = \frac{d^2r}{d\tau^2} = 0,\ U_{\text{eff}} = E^2,\ \frac{d}{dr}U_{\text{eff}} = 0,$$

The circular orbit at $r = r_c$ is called stable if $d^2U_{\text{eff}}/dr^2 > 0$ and unstable if $d^2U_{\text{eff}}/dr^2 < 0$, respectively.

Using these conditions, we can obtain the dependencies of the specific energy $\tilde{E}(r)$, angular momentum $\tilde{L}(r)$, and angular velocity $\Omega = d\varphi/dt$ as functions of the radius r in the following form

$$\tilde{E}^2(r) = \frac{2A^2R'}{2AR' - A'R},\quad \tilde{L}^2(r) = \frac{R^3A'}{2AR' - A'R},\quad \Omega^2(r) = \frac{A'}{2R'R}. \tag{6.6}$$

In dependence on the properties of U_{eff}, the SCOs can form several disjoint domains, as it shown in Fig. 6.1. This is governed by appearance/disappearance of the local minimums of U_{eff}. To analyze this, it is convenient to use the functions

$$\tilde{L}^2(r) = -\frac{A'(r)}{D(r)},\ F(r) \equiv \frac{d}{dr}\tilde{L}^2(r),\ D(r) = \left(\frac{A(r)}{R^2(r)}\right)',\tag{6.7}$$

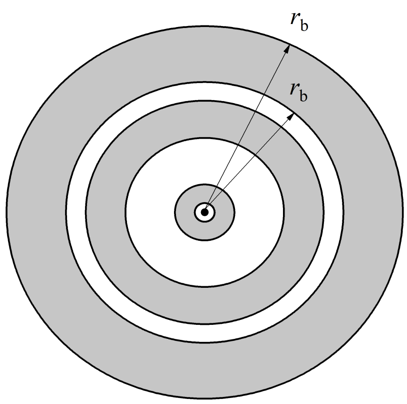

Figure 6.1: The possible schematic example of circular orbits distribution. Where white domains represent SCOs, while grey domains correspond to regions with UCOs or regions where they do not exist.

which is equal to the corresponding angular momentum $L_b^2 = \tilde{L}^2(r_b)$ at the points of bifurcation $r = r_b$. Then, joint conditions for the bifurcation (inflection) point ($U'_{\rm eff} = 0$ and $U''_{\rm eff} = 0$), lead to the necessary condition

$$F(r_b) = R^4 A'' + \tilde{L}^2 \left(R^2 A'' - 4RR'A' - 2RR''A + 6R'^2 A\right) \equiv 0. \tag{6.8}$$

Where the roots r_b of this equation correspond to the radii of bifurcations, which in turn define the boundaries of the SCODs.

The stability of the circular orbit at $r = r_c$ is determined by the next following conditions

$$\tilde{L}^2(r_c) \geq 0, \; -D(r_c)F(r_c) < 0. \tag{6.9}$$

The opposite signs of the first and second inequality correspond to the domain of non-existence of circular orbits (NECO) and unstable circular orbits (UCO), respectively.

For photon geodesics ($S = 0$), the effective potential is given by $U_{\rm eff} = A/R^2$ and the radii of circular photon orbits are determined by solving the equation

$$A'R - 2AR' = 0. \tag{6.10}$$

The maximum and minimum values of $U_{\rm eff}$ correspond to unstable and stable photon orbits, respectively.

6.1.2 Ray-tracing

The procedure for obtaining images of the accretion disk is well-known [152–154] and involves the following steps: (1) We locate the observer plane at the distant point far away from the compact object, where the space-time is already flat; (2) we shoot photons in the direction of the accretion disk and follow their paths until they hit the plane of the accretion disk; (3) we calculate specific values such as frequency shift etc.

The equation of motion for photons can be obtained from the standard variation of the particle action (6.1)

$$\frac{d^2x^\mu}{d\tau^2}+\Gamma^\mu_{\nu\sigma}\frac{dx^\mu}{d\tau}\frac{dx^\nu}{d\tau}=0,$$

For the metric (6.2), in the explicit form they are

$$\ddot{t}+\frac{A'}{A}\dot{r}\dot{t}=0, \tag{6.11}$$

$$\ddot{r}+\frac{B'}{2B}\dot{r}^2+\frac{A'}{2B}\dot{t}^2-\frac{RR'}{B}(\dot{\theta}^2+\sin^2\theta\dot{\varphi}^2)=0, \tag{6.12}$$

$$\ddot{\theta}+\frac{2R'}{R}\dot{r}\dot{\theta}-\dot{\varphi}^2\sin\theta\cos\theta=0, \tag{6.13}$$

$$\ddot{\varphi}+\frac{2R'}{R}\dot{r}\dot{\varphi}+2\dot{\theta}\dot{\phi}\cot\theta=0, \tag{6.14}$$

We place our distant observer at the sufficiently large distance D from the center of the compact object. Then, we fix the Cartesian coordinates (X,Y,Z) at the observer plane and (x,y,z) at the center of the compact object, as illustrated in Fig. 6.2.

It is evident from the Fig. 6.2 that the coordinate systems are related by the combination of rotation and translation coordinate transformations, which can be represented in the final form:

$$x=(D+Z)\sin i-Y\cos i,\ \ y=X,\ \ z=(D+Z)\cos i+Y\sin i,$$

Our background metric is originally written in the spherical coordinates, which means that we need to perform additional transformation from the Cartesian to spherical coordinates

$$r=\sqrt{x^2+y^2+z^2},\ \ \phi=\arctan\left(\frac{y}{x}\right),\ \ \theta=\arccos\left(\frac{z}{r}\right),$$

After that, the initial position $(X_0,Y_0,Z_0=0)$ of the photon at the observer plane will be defined in the compact object's coordinate system as [152, 154]

$$t_0=0,\ \ r_0=\sqrt{X_0^2+Y_0^2+D^2}, \tag{6.15}$$

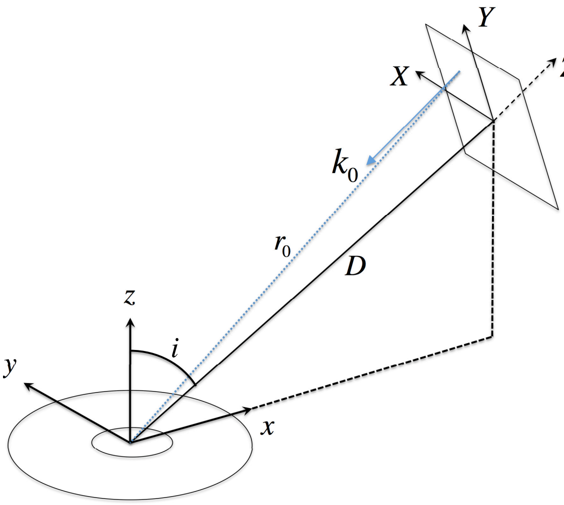

Figure 6.2: The schematic illustration of the system's geometry. The Cartesian coordinates systems (x, y, z) and (X, Y, Z) are centered at the compact object and at the observer plane, respectively. This picture was taken from [155].

$$\theta_0 = \arccos\left(\frac{Y_0 \sin i + D\cos i}{r_0}\right), \ \varphi_0 = \arctan\left(\frac{X_0}{D\sin i - Y_0\cos i}\right),$$

and the initial photon 4-momentum $\tilde{k}^\mu = (1, 0, 0, -1)$ (in the Cartesian coordinates) can be rewritten as $k^\mu = \frac{\partial x^\mu}{\partial x^\nu}\tilde{k}^\nu$ (in the spherical coordinates)

$$k_0^r = -\frac{D}{r_0}, \ k_0^\theta = \frac{\cos i - (Y_0\sin i + D\cos i)D/r_0^2}{\sqrt{X_0^2 + (D\sin i - Y_0\cos i)^2}}, \tag{6.16}$$

$$k_0^\varphi = \frac{X_0 \sin i}{X_0^2 + (D\sin i - Y_0\cos i)^2}, \ k_0^t = \sqrt{(k_0^r)^2 + r_0^2(k_0^\theta)^2 + r_0^2\sin^2\theta_0(k_0^\varphi)^2},$$

We obtain the photon trajectories numerically by integrating (6.11-6.14) with the initial conditions (6.15, 6.16) backward in time up to the moment of intersection of the AD plane.

The frequency ratio g between the point (e) at the AD surface and the static remote observer (o) for the metric (6.2) is

$$g = \frac{k_\mu u^\mu|_o}{k_\mu u^\mu|_e} = \frac{\sqrt{A(r) - R^2(r)\Omega^2(r)}}{1 + \lambda\Omega(r)}, \tag{6.17}$$

where λ is a conserved quantity along the photon geodesic, and can be determined from the initial conditions as $\lambda = -r_0^2 \sin^2\theta_0 k_0^\phi / k_0^t$. The sign of $\lambda\Omega(r)$ is determined by the choice of whether the AD is rotating around the compact object in a clockwise or counterclockwise direction. Further, we will use the normalized redshift factor in our color plots

$$\tilde{g} = \frac{g - g_{\min}}{g_{\max} - g_{\min}}, \tag{6.18}$$

where $g_{\min}$ and $g_{\max}$ is the minimal and maximal frequency values on disk, respectively.

6.2 $V(\phi) = \omega\phi^{2n}$

6.2.1 Stable circular orbits distributions

The effective potential U_{eff} in curvature coordinates (2.11) has the form

$$U_{\text{eff}}(r, L, S) = e^{\alpha}\left(S + L^2/r^2\right) \tag{6.19}$$

Taking into account the asymptotic behavior of the metric functions near the singularity and at the spatial infinity, we can obtain the corresponding asymptotic behavior for the effective potential, when $L \neq 0$.

Specifically, we have

$$U_{\text{eff}} \sim r^{\eta-3},\ r \to 0, \quad U_{\text{eff}} \to S,\ r \to \infty. \tag{6.20}$$

If $\eta < 3$, then for $r \to 0$, we have that $U_{\text{eff}} \to \infty$, which indicates the existence of an infinite potential barrier in vicinity of the singularity that reflects falling particles. On the other hand, if $\eta > 3$, then for $r \to 0$, $U_{\text{eff}} \to 0$, which means that particles can approach the singularity.

The equation (6.8) for the metric (2.11) takes the form

$$F(r) = \tilde{L}^2(r)[r^2\alpha''(r) - 2r\alpha'(r) + 6] + r^4\alpha''(r). \tag{6.21}$$

Solving this equation, we obtain a set of bifurcation values r_b that define radii of circular orbit domains, and related to them values of the specific angular momentum and energy $L_b^2 = \tilde{L}^2(r_b)$ and $E_b^2 = \tilde{E}^2(r_b)$, respectively. Also, we check their signs to make sure that they are positive.

We have carried out numerical investigations for different sets of parameters (M, Q, n) and found at least four possible types of SCOD, which presented in Table 6.1. The $U1, S1, S2$ types exist in the FJNW case, while $S3$ is new one. Here and after, we denote bifurcation radii r_b as $r_b \equiv r_{i(T)}$, where the index i corresponds to the number of the root, and the index T corresponds to the SCOD type.

Now let us briefly describe them. We start with types that correspond to the case with $\eta < 3$.

	Stable	Unstable	$\text{sgn}(\eta - 3)$	Photon sphere
$S1$	$(0, \infty)$	no	$-$	no
$S2$	$(0, r_{1(2)}) \cup (r_{2(2)}, \infty)$	$(r_{1(2)}, r_{2(2)})$	$-$	no
$S3$	$(0, r_{1(3)}) \cup (r_{2(3)}, r_{3(3)}) \cup (r_{4(3)}, \infty)$	$(r_{1(3)}, r_{2(3)}) \cup (r_{3(3)}, r_{4(3)})$	$-$	no
$U1$	$(r_{1(U)}, \infty)$	$(r_{\text{ph}}, r_{1(U)})$	$+$	yes

Table 6.1: Possible types of SCOD

- $S1$: $\tilde{L}^2(r)$ is a monotonically increasing function. There is only one domain of SCO which starts from the singularity and extend to the infinity ($r \in (0, \infty)$).

- $S2$: $\tilde{L}^2(r)$ is a non-monotonic function. The effective potentials U_{eff} have a two minima, which correspond to two disjoint domains of SCOs. The first one form inner disk with SCOs radii $r \in (0, r_{1(2)})$ and second one form outer disk with $r \in (r_{2(2)}, \infty)$. In domain between them we have UCOs with radii $r \in (r_{1(2)}, r_{2(2)})$.

- $S3$: It is a new type of the SCOD which cannot be realized in the FJNW case. $\tilde{L}^2(r)$ is a non-monotonic function, the effective potential U_{eff} can have three minima and two maxima which relate to three disjoint SCOs regions with radii $r \in (0, r_{1(3)}) \cup (r_{2(3)}, r_{3(3)}) \cup (r_{4(3)}, \infty)$. They are separated by two domains of the unstable orbits with radii $r \in (r_{1(3)}, r_{2(3)}) \cup (r_{3(3)}, r_{4(3)})$.

In case of $\eta > 3$ there is only one possibility

- $U1$: $\tilde{L}^2(r)$ is negative at $r \in (0, r_{\text{ph}})$, which means that there are no circular orbits. Also, $\tilde{L}^2(r)$ is a positive and bounded from below function on the interval $r \in (r_{\text{ph}}, \infty)$. The effective potential U_{eff} is bounded from above, $U_{\text{eff}} \to 0$ for $r \to 0$, and only one maximum exists. In this case, we have one domain without circular orbits with radii $r \in (0, r_{\text{ph}})$, one domain of UCOs with $r \in (r_{\text{ph}}, r_{1(U)})$, and one domain of the SCOs with $r \in (r_{1(U)}, \infty)$. This case is qualitatively similar to the SCO distribution in the Schwarzshild BH case.

The typical behavior of $U_{\text{eff}}(r, L)$ and $\tilde{L}(r)$ is shown in Fig. 6.3. The right panel demonstrates examples of $U_{\text{eff}}(r, L)$ in the case when three minima appear for different values of the angular momentum L. It can be observed that the third minimum emerges in the vicinity of the singularity. Also, we need to note that this case corresponds to $\eta < 3$, but very close to the critical value of $\eta = 3$, where the behavior of U_{eff} dramatically changes.

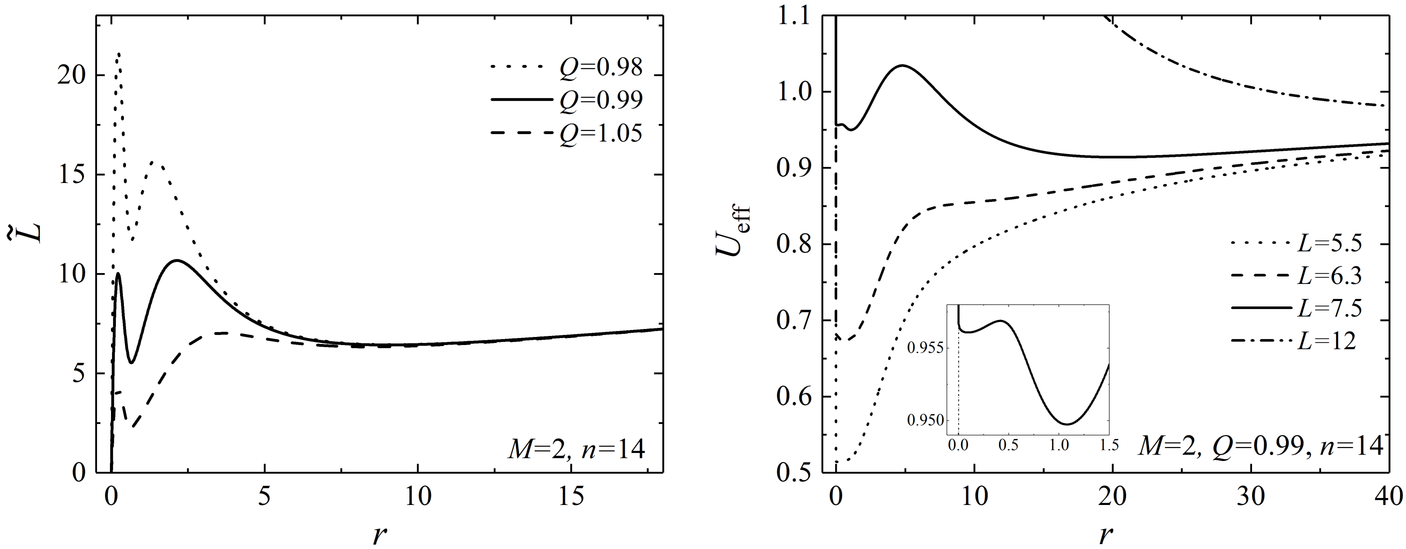

Figure 6.3: Typical dependencies of $\tilde{L}(r)$ and $U_{\text{eff}}(r)$ in case of $S3$ type. The left panel demonstrates that there can be several circular orbits with the same $\tilde{L}(r) = L$. The right panel demonstrates the effective potential with three minima, which is characteristic for the $S3$ type. For $L \sim 6.3$, three different SCOD can exist for fixed values of M, Q, and n.

We have studied in detail the behavior of r_b as a function of M, Q, and n. The results are presented in Figs. 6.4-6.6. Fig. 6.4 illustrates examples of $r_b(Q)$ both in the presence and absence of the $S3$ case. A detailed description is provided below. In Fig. 6.5, we show the dependence of $r_b(Q)$ for different values of n. Fig. 6.6 depicts analogous dependencies, but for $r_b(M)$. These figures highlight significant differences from the FJNW case: (1) There is a disjoint second branch of r_b, and (2) the values of r_b can exceed $r_b^{Schw} = 6M$ in the case of a standard Schwarzschild black hole.

Also, we found the domains of parameters where different cases can be realized. The results are shown in Figs. 6.7-6.12 for various values of M, Q, and n. Unlike to the FJNW solution, the domain with the $S1$ case is finite and bounded, and its size varies non-monotonically. It increases up to $n \sim 7$ and then decreases up to 0. The $S3$ case typically occurs at high values of n, but it can also be obtained for lower n by choosing sufficiently large values of M and Q. We found that the $S3$ region appears roughly at $n \approx 4.32$ (see Fig. 6.7, right).

For any value of M, there exist two separate branches in the $r_b(Q)$ curve. Additionally, there is a sequence of critical values of n, denoted as $n_1^* < n_2^* < n_3^* < n_4^* < n_5^*$, with the following characteristics.

For $2 < n < n_1^*$, both branches are unbounded (like two solid curves on the left panel of Fig. 6.5). At some $n = n_1^*$, they reconnect. For $n \in (n_1^*, n_4^*)$, the left branch approaches the FJNW case, while the right one is stay unbounded (like dashed and dotted curves on the left panel of Fig. 6.5).

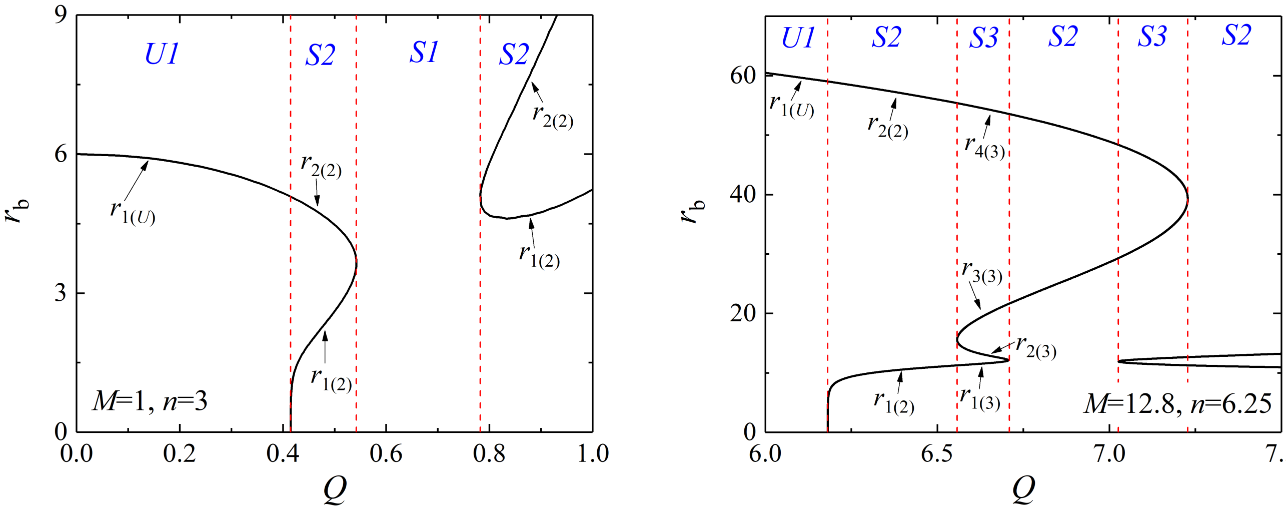

Figure 6.4: Boundary radii of SCO regions as a function of Q for some fixed M, n. Vertical dashed lines separate areas of different SCOD types. In the left panel, we have the $S1$ area between two branches of the $S2$ type and SCO radii lead in $r \in (0, \infty)$. The right panel shows an example with larger values of M, Q, and n, where the $S3$ type is present. The corresponding parameters relate to yellow region in Figs. 6.11 and 6.12.

For $n_1^* < n < n_2^*$, the right branch moves away to the right and then returns for $n > n_2^*$.

At $n = n_3^*$, an additional wedge-like feature in the left branch appears. It is formed by sections $r_{1(3)}$ and $r_{2(3)}$ within the area of $S3$ type, which looks like a "Pinocchio's nose" in the right panel of Fig. 6.5 (solid curve) shown for $n = 13.75$, as the example.

For $n \in (n_4^*, n_5^*)$, the right branch returns closer to the left one, and a new $S3$ area emerges. In the right panel of Fig. 6.4, an additional small $S3$ area is present due to the wedge-like form for $r_b \sim 10, Q \gtrsim 7$.

At $n = n_5^*$, the tips of the two wedges touch each other (as seen in the right panel of Fig. 6.4). The bifurcation curve undergoes a new reshaping, after which the branches reconnect, forming a structure represented by the solid curve on the right panel of Fig. 6.5. For large enough n, the lower branch tends to the abscissa axis.

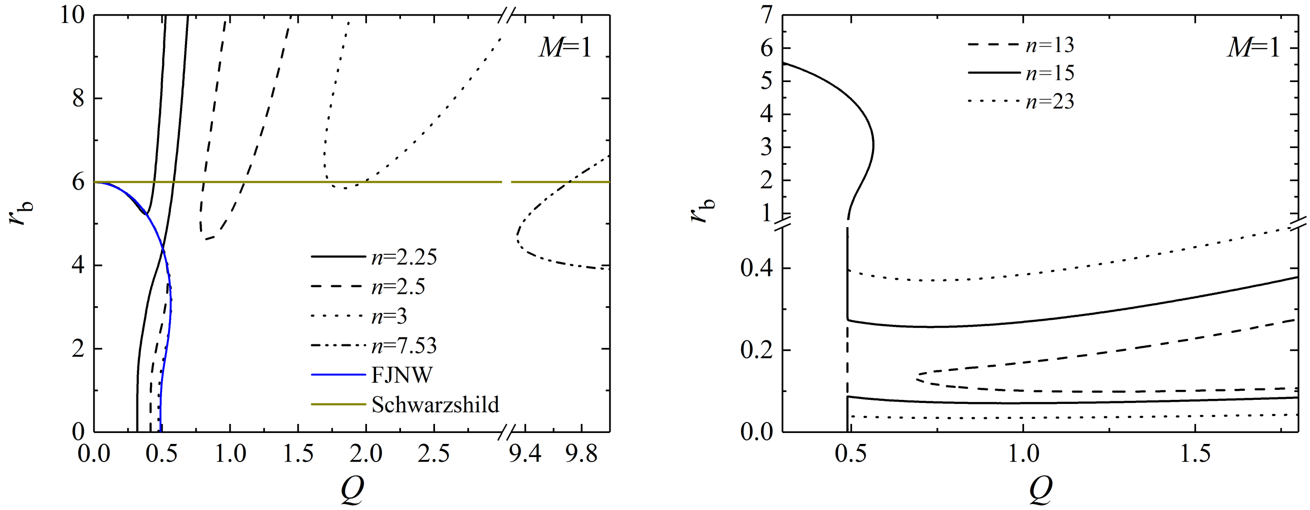

Figure 6.5: Boundary radii r_b of SCO regions as a functions of Q for $M = 1$ and various fixed values of n. The solid blue curve corresponds to the FJNW solution, while the orange horizontal line represents the case of a Schwarzschild black hole with $r_b = 6M$. Also, we found that $n_1^* \approx 2.38$, $n_2^* \approx 7.53$, $n_3^* \approx 13.12$, $n_4^* \approx 13.13$ and $n_5^* \approx 13.15$.

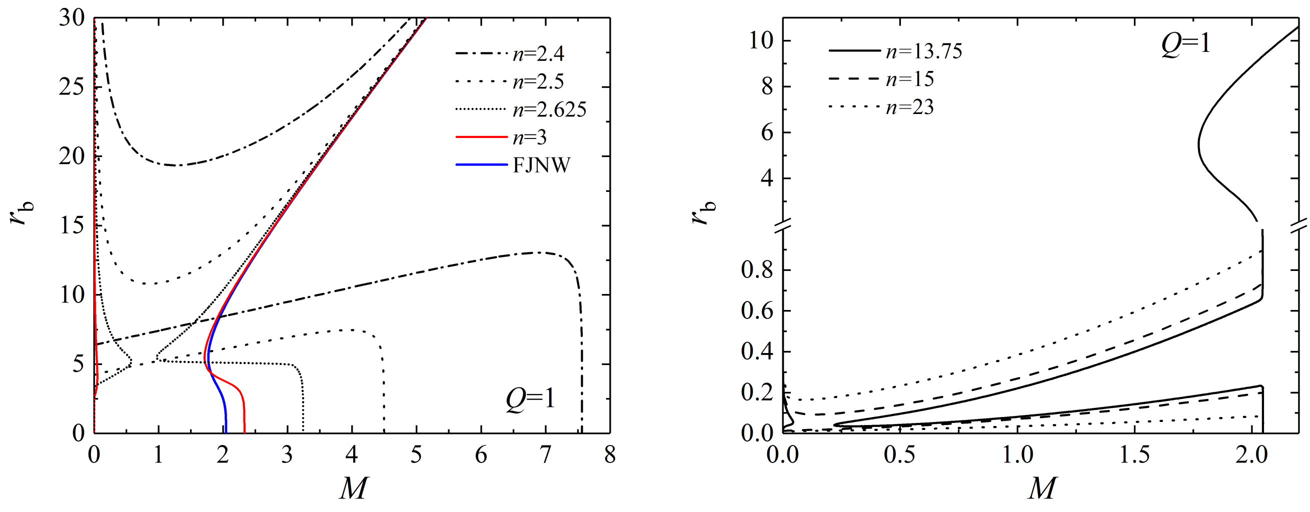

Figure 6.6: Boundary radii r_b of SCO regions as a functions of M for $Q = 1$ and various fixed values of n. The left panel illustrates the behavior of the two branches around the first reconnection, occurring at $n \approx 2.62$. The right panel demonstrates this branches around the second reconnection, which takes place at approximately $n \approx 13.86$.

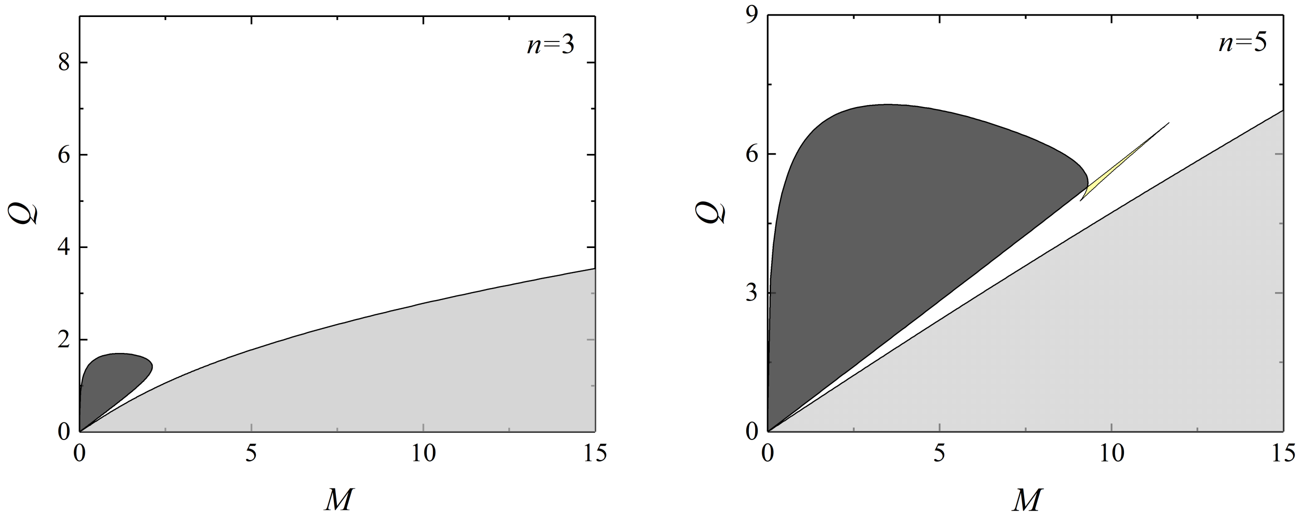

Figure 6.7: Domains of parameters in the (M, Q) plane for different values of n. The regions labeled with white, yellow, light gray, and dark gray correspond to $S2$, $S3$, $U1$, and $S1$ types, respectively. It should be noted that for values of n around 7, the $S1$ area grows.

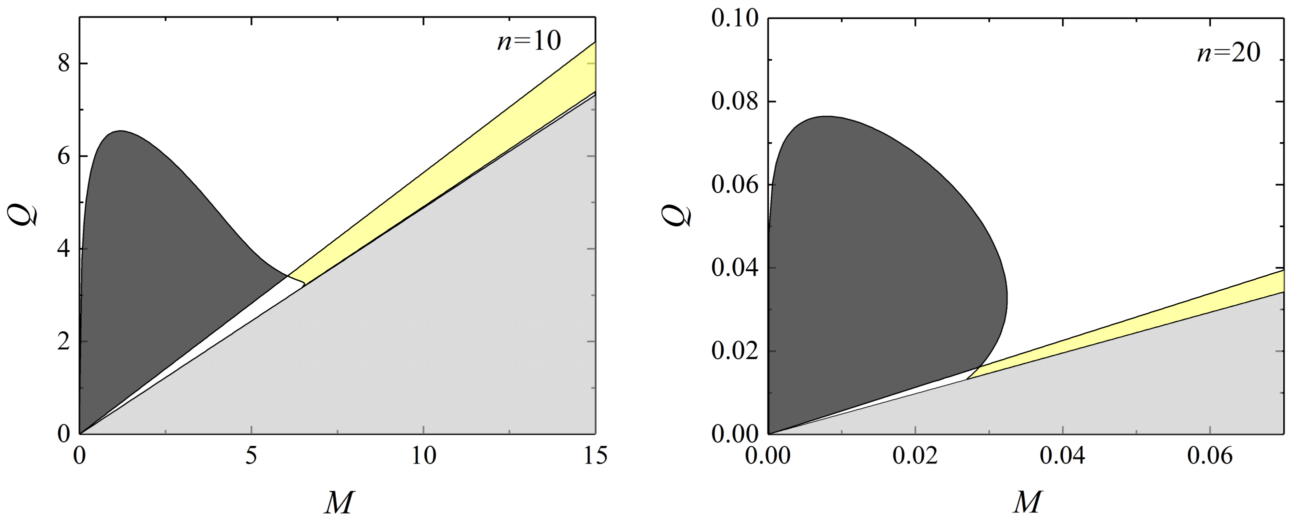

Figure 6.8: The same but for large values of n. For $n \gtrsim 7$ the black region ($S1$) shrinks to the origin.

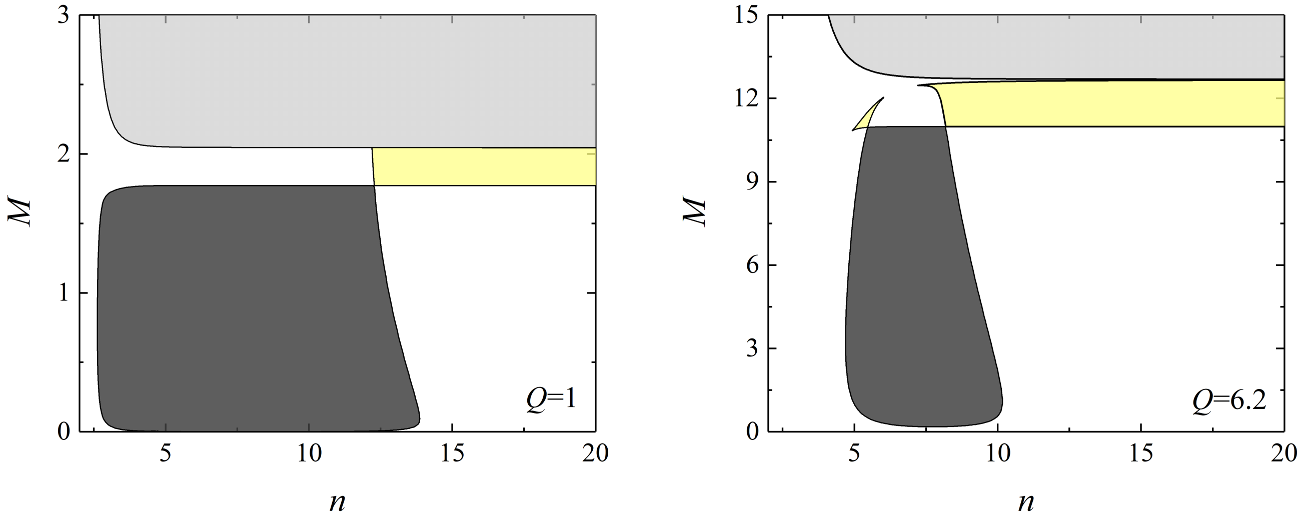

Figure 6.9: Domains of parameters in the (n, M) plane for different values of Q. As in the previous plots the regions labeled with white, yellow, light gray, and dark gray correspond to $S2$, $S3$, $U1$, and $S1$ types, respectively. It can be observed that as the value of Q increases, the required value of n for the appearance of $S3$ decreases.

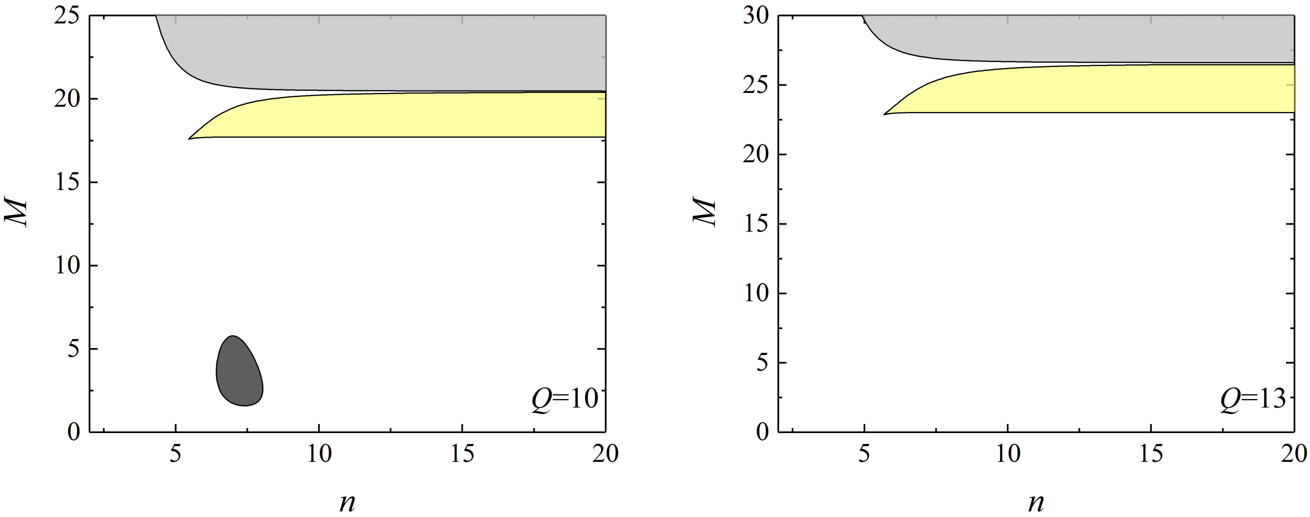

Figure 6.10: The same as in the previous figure, but for larger Q. It can be observed that in the right panel, the $S1$ domain has already disappeared.

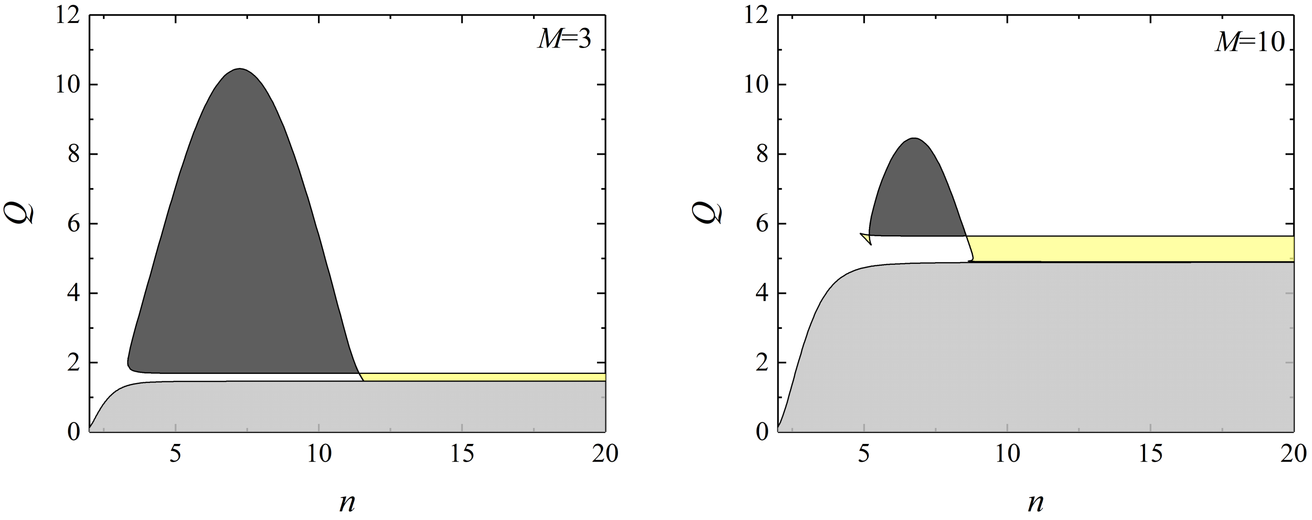

Figure 6.11: Domains of parameters in the (n, Q) plane for different values of M. As in the previous plots the regions labeled with white, yellow, light gray, and dark gray correspond to $S2$, $S3$, $U1$, and $S1$ types, respectively. It can be observed that as the value of M increases, the required value of n for the appearance of $S3$ decreases.

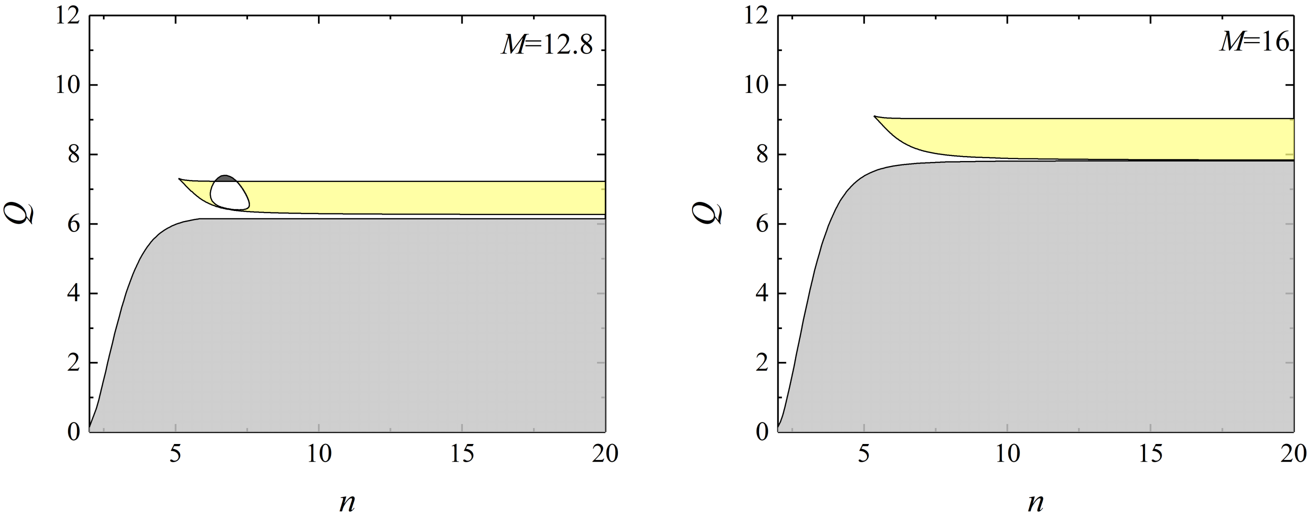

Figure 6.12: The same as in the previous figure, but for larger values of M. It can be observed that in the right panel, the $S1$ domain has already disappeared.

Photon orbits

In case of the photon geodesics, when $S = 0$, the effective potential has very simple form

$$U_{\text{eff}}(r, L, 0) = e^{\alpha} L^2 / r^2.$$

The asymptotic behaviour is the same as for the massive particles (6.20). The radii of the photon orbits can be defined from equation

$$f(r) = r\alpha'(r) - 2. \tag{6.22}$$

We numerically checked that $f(r)$ is a monotonically decreasing function. Furthermore, $f(r) \to -2$ for $r \to \infty$, and as $r \to 0$, $f(r)$ is greater or less than zero if η is greater or less than 3, respectively. Hence, there is a root of $f(r)$ only if $\eta > 3$. This root corresponds to the the point of maximum r_{ph} of the effective potential U_{eff} and represents the radius of the photon sphere.

Typical examples of r_{ph} as a function of scalar charge Q (left panel) and configuration mass M (right panel) for different values of n are presented in Fig. 6.13. It can be observed that the values of r_{ph} are always less then the corresponding values in the FJNW case and tend towards to them as n increases. Furthermore, the r_{ph} radii are always less than $r_{\text{ph}} = 3M$ in the case of the standard Schwarzschild black hole.

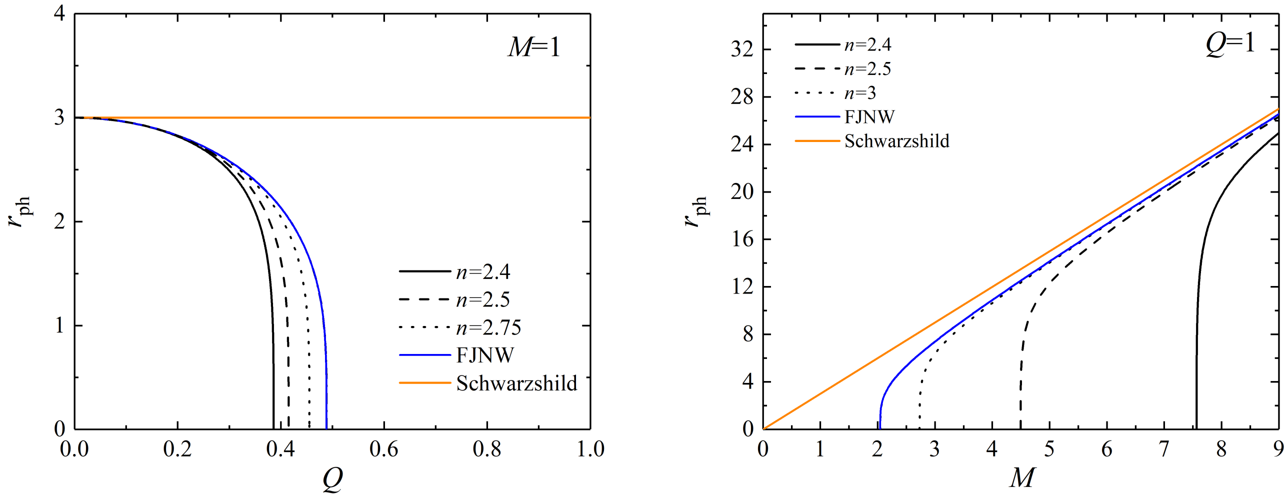

Figure 6.13: The radii of photon orbits as a function of Q (left panel) and M (right panel) are shown for various values of n. The blue and orange curves represent the FJNW and Schwarzschild cases, respectively.

6.2.2 Keplerian AD images

We have generated direct Keplerian AD images for various inclination angles for the $U1$, $S1$, $S2$, and $S3$ cases. These images are displayed in Figs. 6.15–

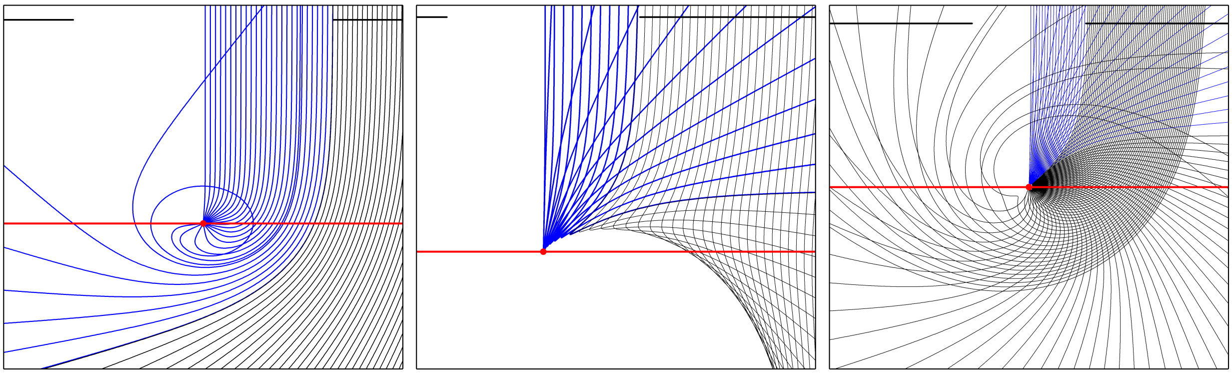

(a) U1 (b) S1 (c) S3

Figure 6.14: Example of the photon geodesics for $U1$, $S1$ and $S3$ case. Example of the photon geodesics for $U1$ (a), $S1$ (b) and $S3$ (c) case. In all cases the red line corresponds the equatorial plane of AD. (a) Trajectories of photons in vicinity of the attracting singularity. (b) The same but with the repulsing singularity. In this case, we also have a dark spot around the center, that imitate a black hole. (c) The intermediate case, when the repulsion is small enough. In small vicinity singularity rays reflect from them and far enough they have similar behaviour as in (a).

6.22, and the normalized frequency shift (6.18) is represented using colors.

One of significant feature common in all images is the presence of a dark spot, which can resembles a shadow of an ordinary black hole. In the case of $U1$, the dark spot is related to the presence of the photon sphere, while in the $S1$, $S2$, and $S3$ cases, it is the result of the repulsive nature of the singularity. As we demonstrated above it depends on the sign of $\eta - 3$ (see Eq. 6.20).

For $\eta > 3$, we have a maximum of $U_{\rm eff}$ and photons with impact parameter $\lambda < [b_{max}]^{-1/2}$, $b_{max} = \exp\{[\alpha(r_{\rm ph})]\}/r_{\rm ph}^2$, can reach the singularity ((a) in Fig. 6.14).

For $\eta < 3$, photons with nonzero angular momentum will be reflected by the effective potential, i.e. they cannot reach the region near the singularity ((b) in Fig. 6.14). Due to the strong bending of the photon geodesics, a scattered photon can hit a point on the AD plane far enough from the center, where another photon with a different trajectory and angular momentum also hits, which means that each such point has two images.

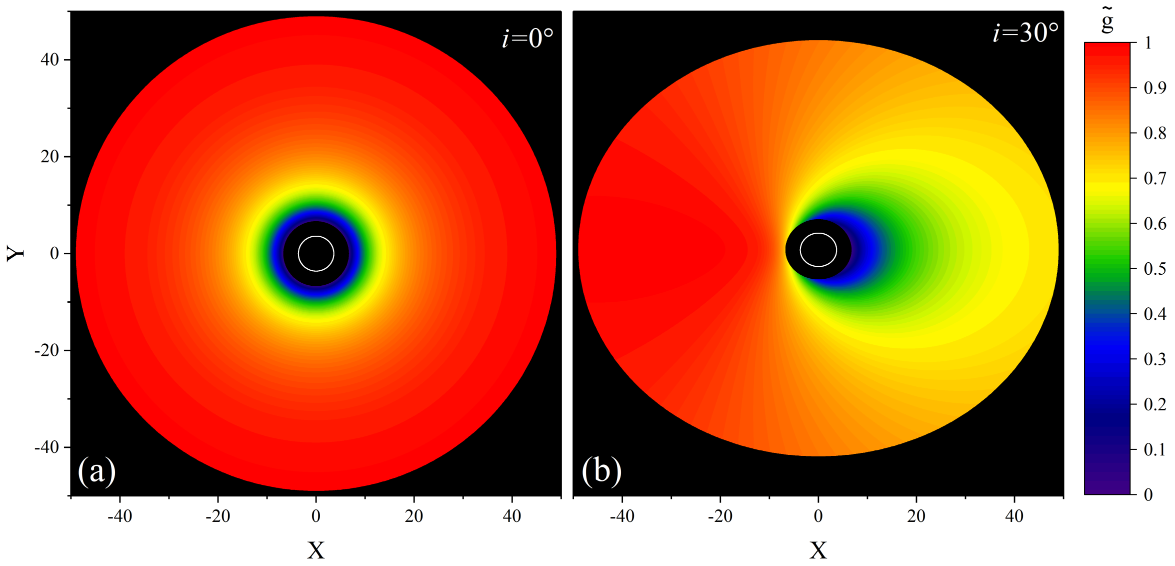

Figure 6.15: Keplerian AD images for the $U1$ type ($M = 1$, $Q = 0.3$, $n = 3$): in full face and for inclination $i = 30^o$. White contour corresponds to the image of photon orbit at $r_{\rm ph} \approx 2.58$. The ISCO placed at $r_{1(U)} \approx 5.56$.

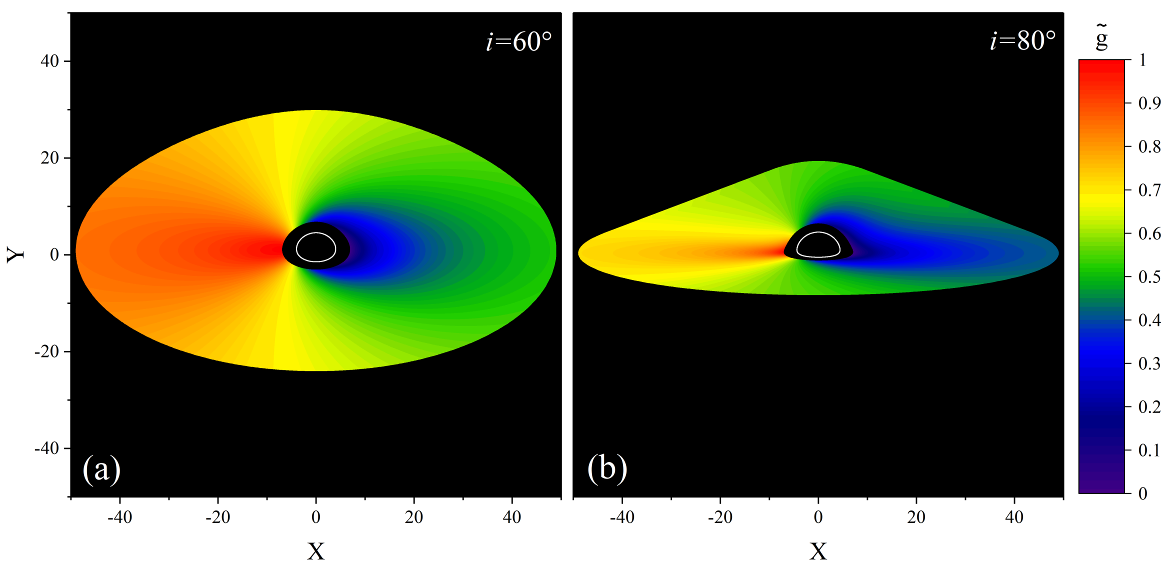

Figure 6.16: The same as on Fig. 6.15 with inclinations 30^o and 60^o.

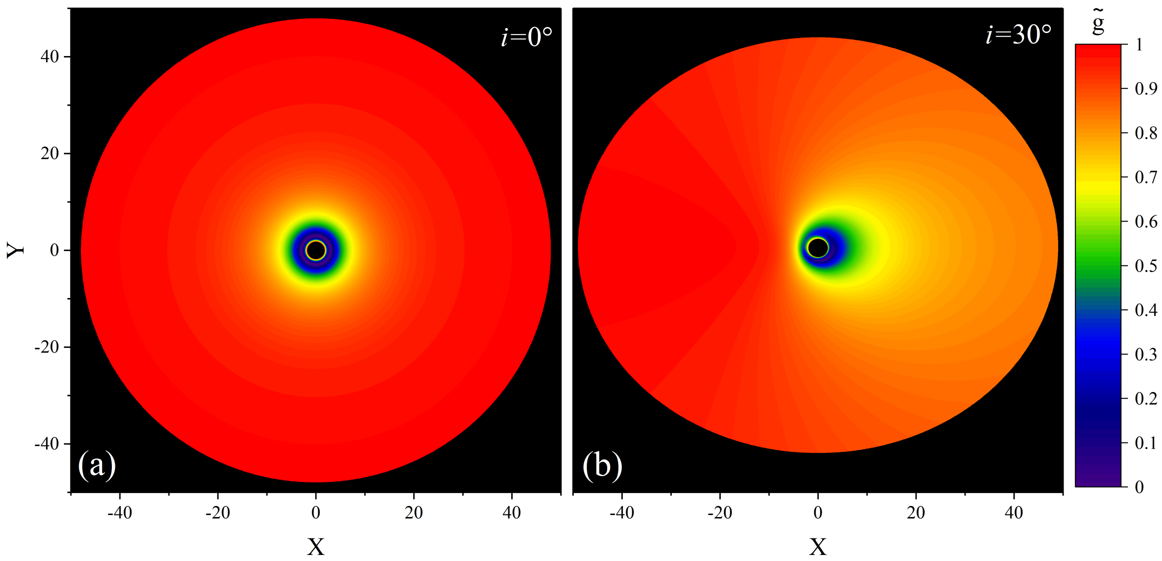

Figure 6.17: AD images for the $S1$ type ($M = 1$, $Q = 0.8$, $n = 3$) for inclinations $i = 0^o$ and $i = 30^o$, respectively. There is a dark spot in the center due to the repulsive character of the naked singularity.

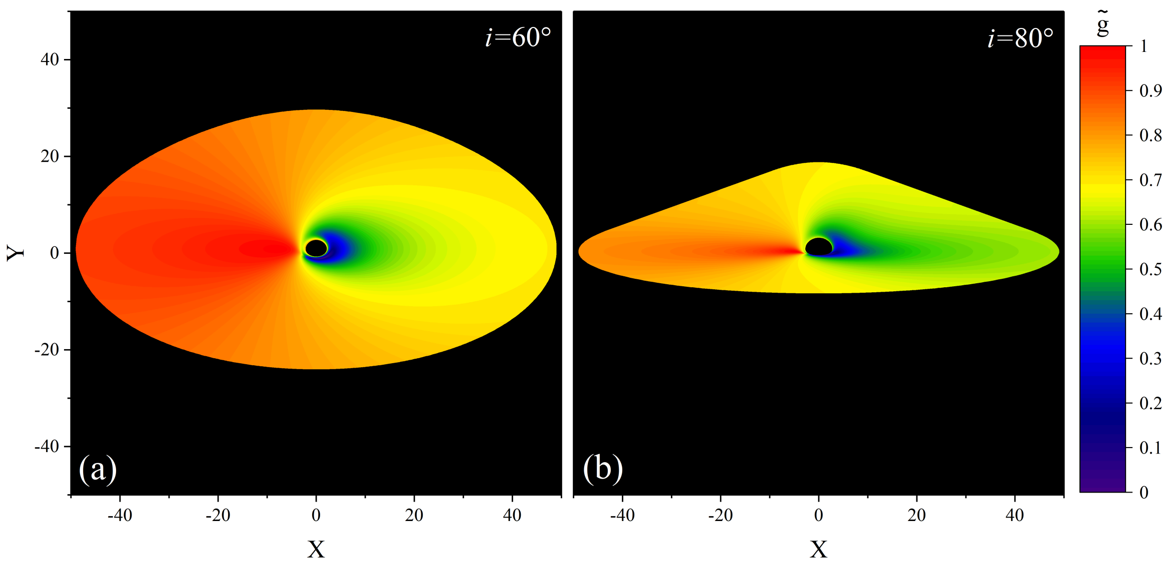

Figure 6.18: The same as on Fig. 6.17 with inclinations 60^o and 80^o.

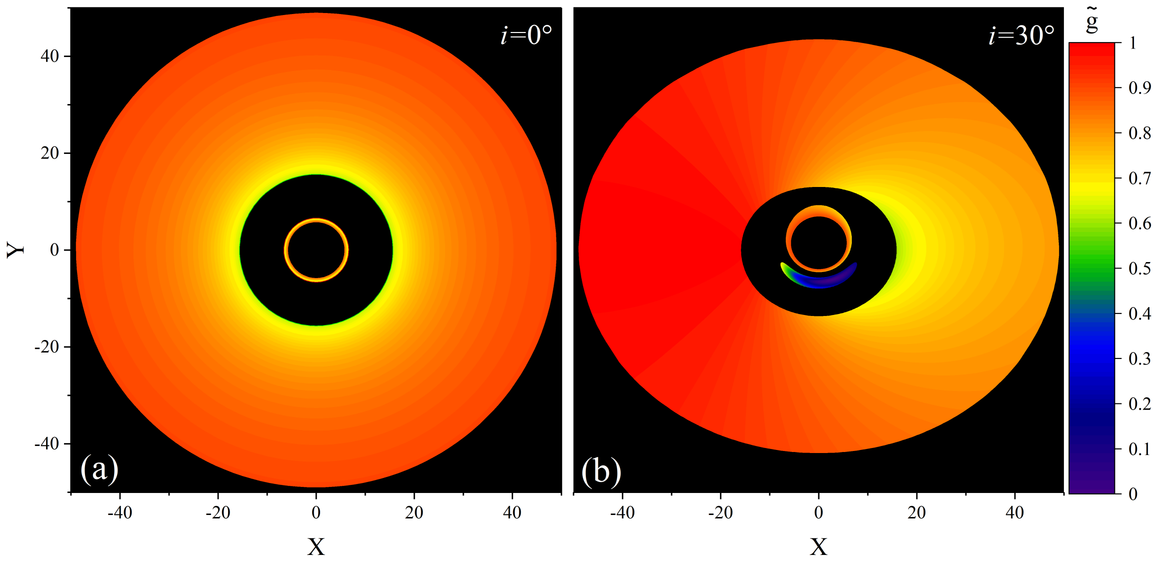

Figure 6.19: AD images for the $S2$ type ($M = 1$, $Q = 2.2$, $n = 3$) in full face and for inclinations $i = 0^o$ and $i = 30^o$, respectively. The SCO radii are divided into two regions: (i) the inner disk with $r \in (0, 6.5)$ and (ii) the outer disk with $r \in (14.5, \infty)$. In panel (a), the inner SCO region cannot be observed due to the repulsive nature of the naked singularity. The thin ring at the center represents the outer part of (ii).

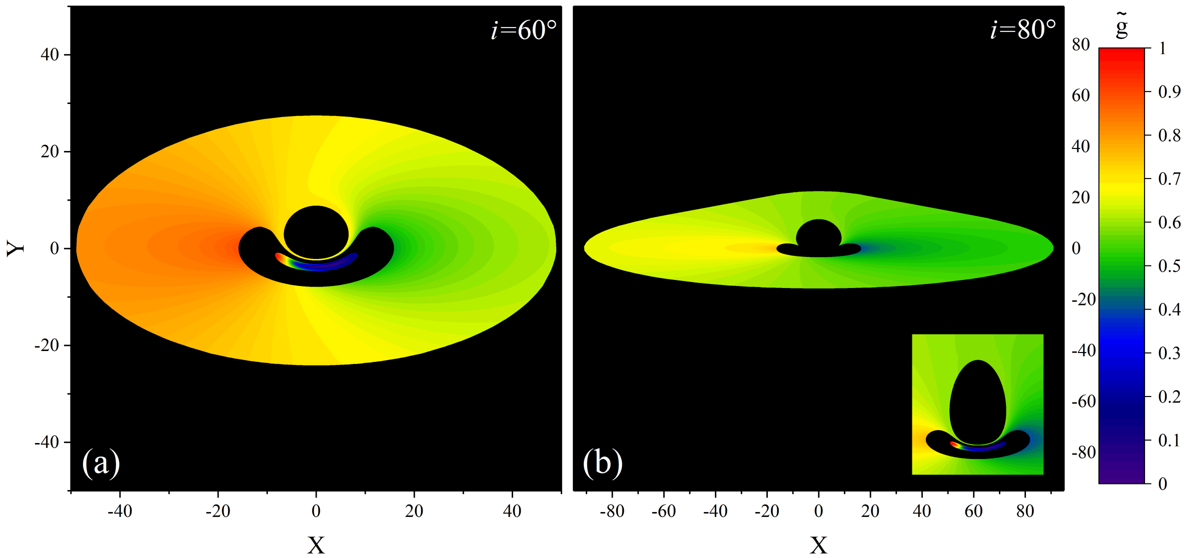

Figure 6.20: The same as on Fig. 6.19 with inclinations 60^o and 80^o.

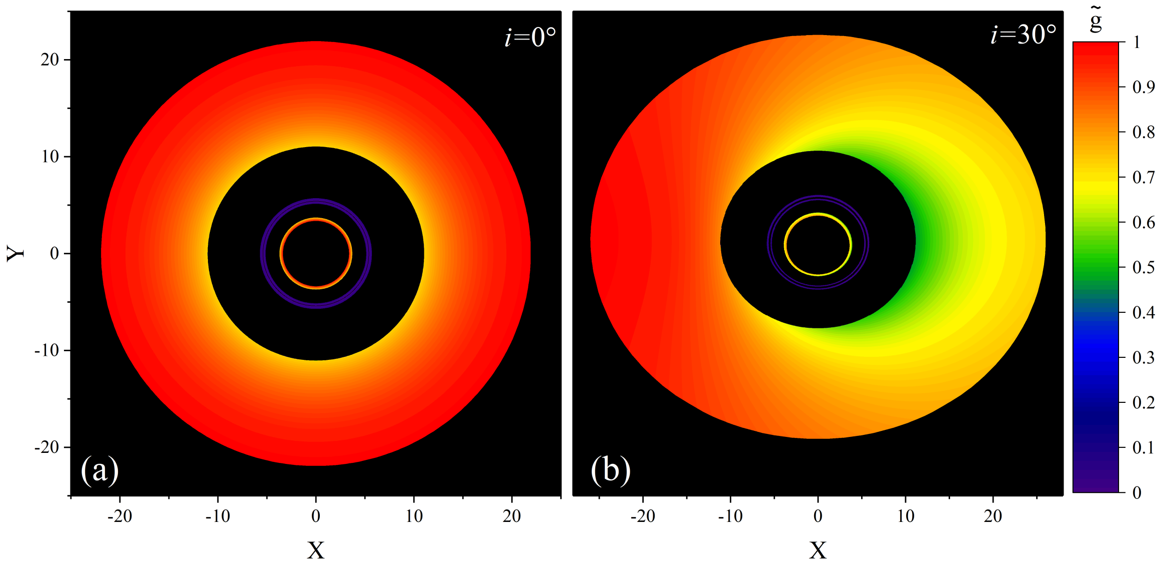

Figure 6.21: The Keplarian AD images for the $S3$ type ($M = 2$, $Q = 0.99$, $n = 14$), $\eta \approx 2.9998$ for inclinations $i = 0^o$ and $i = 30^o$, respectively. The SCO radii intervals are divided into three regions: (i) $r \in (0, 0.22)$ representing the inner SCO region, (ii) $r \in (0.65, 2.14)$ representing the intermediate SCO ring, and (iii) $r \in (9, \infty)$ representing the outer unbounded SCO ring. The bright orange rings at the center represent the image of the outer part of the outer disk, which has a high surface brightness due to strong lensing effect. The intermediate SCO ring (ii) has two images shown as two blue circles that almost merge together. Both panels do not show the inner SCO region (i) as it is invisible.

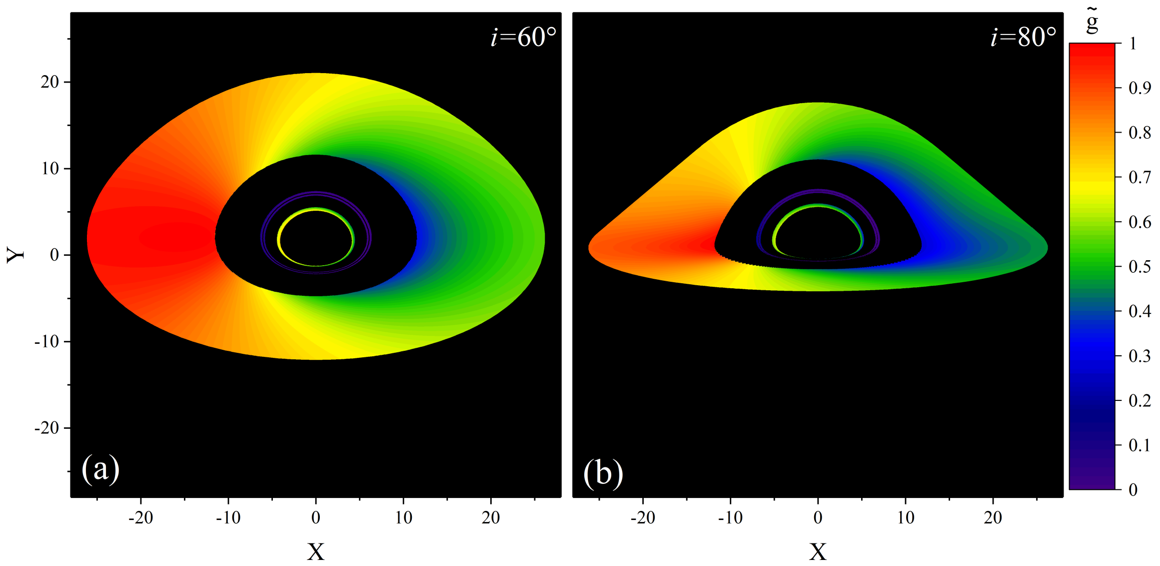

Figure 6.22: The same as on Fig. 6.21 with inclinations 60^o and 80^o.

6.3 $V(\phi) = w \sinh\left(\kappa\phi^{2n}\right)$

6.3.1 SCO distributions

Now, we proceed to the strongly nonlinear case. The one of the main distinction from the previous case lies in the existence of the spherical singularity at some specific value of $r = r_s > 0$. Taking into account the asymptotic behavior of $\alpha(r)$ near the SS and at spatial infinity, we obtain

$$U_{\text{eff}} \sim \frac{e^{\alpha_0}}{r_s^2}, \; r \to r_s + 0, \quad U_{\text{eff}} \to S, \; r \to \infty. \tag{6.23}$$

Thus, we have a finite-height potential barrier near the singularity. After repeating the consideration used in the previous section, we found at least four qualitatively distinct types of SCOD, which are summarized in Tab. 6.2.

Type	r_{stable}	r_{unstable}	Photon sphere
$U_1^{(-)}$	(r_1, ∞)	(r_s, r_1)	$-$
$U_1^{(+)}$	(r_1, ∞)	(r_s, r_1)	$+$
U_2	$(r_1, r_2) \cup (r_3, \infty)$	$(r_s, r_1) \cup (r_2, r_3)$	$-$
U_3	$(r_1, r_2) \cup (r_3, r_4) \cup (r_5, \infty)$	$(r_s, r_1) \cup (r_2, r_3) \cup (r_4, r_5)$	$-$

Table 6.2: Possible types of SCOD

They can be briefly described in the following way.

- $U_1^{(+)}$: This case is qualitatively similar to the distribution of SCOs in Schwarzschild BH case, as well as to the $U1$ case from the previous section.

- $U_1^{(-)}$: This case is similar to $U_1^{(+)}$ case, but it lacks a photon sphere. We have one domain of unstable circular orbits with $r \in (r_{\text{s}}, r_{1(1)})$, and one domain of stable circular orbits with $r \in (r_{1(1)}, \infty)$.

- U_2: $\tilde{L}^2(r)$ is a non-monotonic function. The effective potential U_{eff}, has two minima, which correspond to two disjoint domains of SCOs. The first one forms the inner disk with SCOs radii $r \in (r_{1(2)}, r_{2(2)})$ and second one forms the outer disk with $r \in (r_{3(2)}, \infty)$. We have UCOs with radii $r \in (r_s, r_{1(2)}) \cup (r_{2(2)}, r_{3(2)})$.

- U_3: $\tilde{L}^2(r)$ is a non-monotonic function and the effective potential U_{eff} can have three minima and two maxima, which relate to three disjoint SCOs regions with radii $r \in (0, r_{1(3)})$, $(r_{2(3)}, r_{3(3)})$,$(r_{4(3)}, \infty)$. These regions are separated by two domains of the unstable orbits with radii $r \in (r_s, r_1) \cup (r_{3(3)}, r_{4(3)})$. The typical example of $\tilde{L}$ is shown in Fig. 6.23 (a).

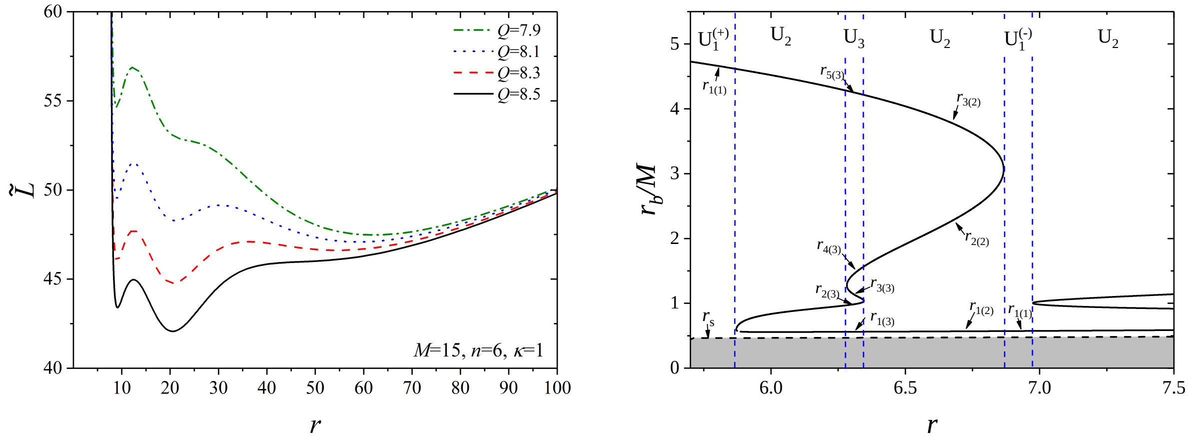

Figure 6.23: Typical behaviour of $\tilde{L}$ for configuration with U_3 SCOD type.

In Figs. 6.23 – 6.26 we present the typical dependencies of the bifurcation radii r_b. We also found the domains of parameters, where this cases can be realized, they are shown in Fig. 6.27 for various values of M, Q, n and κ.

We can observe a few significant features in the SCODs and differences between the current case, FJNW, and $w\phi^{2n}$ cases. The first one notable feature is the constant presence of a ring of UCOs with radii $(r_s, r_{1(T)})$ near the singularity. This UCO ring distinguishes the current situation from the FJNW and $w\phi^{2n}$ cases. The second one feature is related to the bounded size of the $U2$ domain, similar behavior observed in the FJNW case with the S_2 domain. As the parameter κ increases, the size of the U_2 domain decreases. This dependence on κ has a significant impact on the sizes of the parameters domains. Furthermore, the U_3 case, similar to the $S3$ case. However, we did not find examples with the U_3 case for the parameter values approximately around $M \sim 1$ and $Q \sim 1$.

Similarly to the previous consideration, we can briefly describe behaviour of the biffurcation radii r_b for the U_3 case and underline additional difference from $S3$ case.

For instance, if we fix M, κ, then we can define a sequence of critical values of n, denoted as $n_1^* < n_2^*, n_3^* < n_4^* < n_5^*$, with the following characteristics.

For $2 < n < n_1^*$, there are two disjointed branches (represented by two solid curves in Fig. 6.25 (a, $n = 3$). The first one is bounded from below and the second represent a closed curve with a finite length. At some $n = n_1^*$, this branches connect at some $Q = Q^*$ and reshape into one continues curve of complicated form ($n = 4$).

For $n_1^* < n < n_2^*$, the curve starts deforming, and the point which corresponds to the maximal value of the right part of the curve starts moving away to the right until some $n = n_2^*$ and then comes back.

At $n = n_3^*$, similarly to $S3$, an additional wedge-like feature in the left part of the curve ($Q < Q^*$) appears, which leads to the appearance of an additional ring of SCOs with $r \in (r_{2(3)}, r_{3(3)})$ (see Fig. 6.23 (b)).

At $n = n_5^*$, a new reconnection occurs, and the curve transits back into its previous form. Increasing n leads to the disappearance of the second part(closed curve). This is represented in Fig. 6.27, where we can observe the bounded U_2 domain.

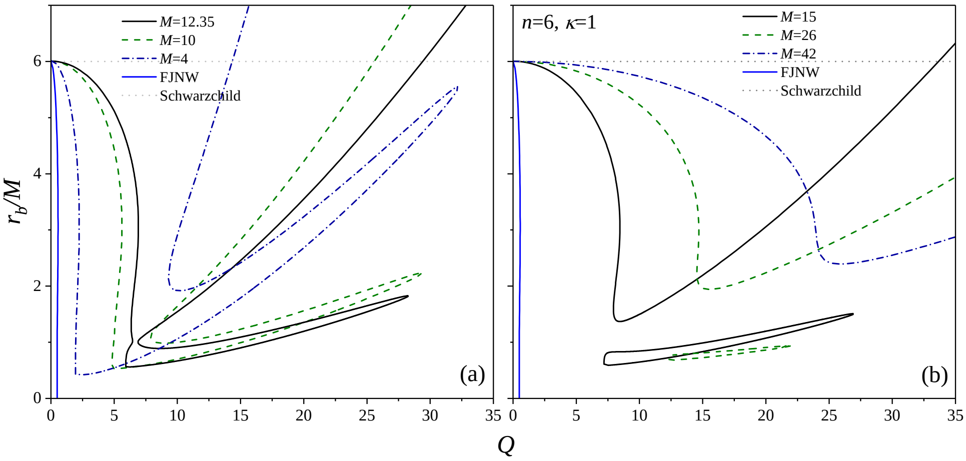

Figure 6.24: Boundary radii r_b/M of SCO regions as functions of Q for several values of M. They corresponds situations after first reconnection (a) and after the second one (b).

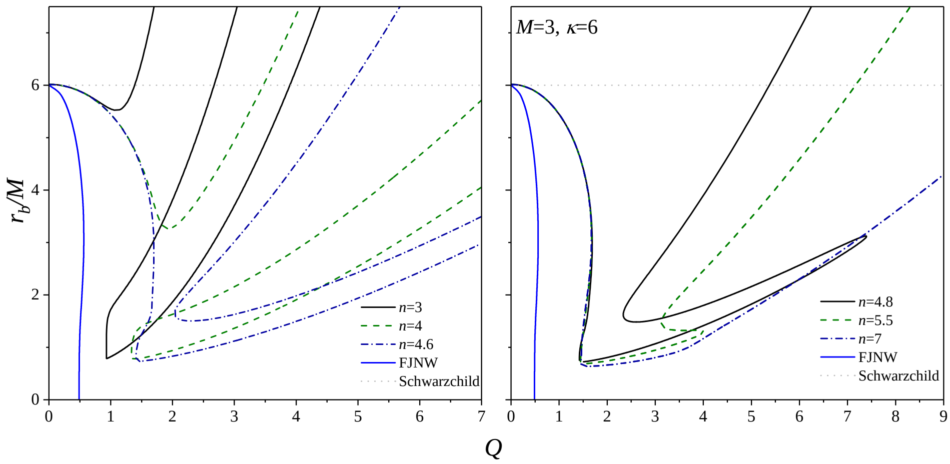

Figure 6.25: Boundary radii r_b/M of SCO regions as functions of Q for several values of n.

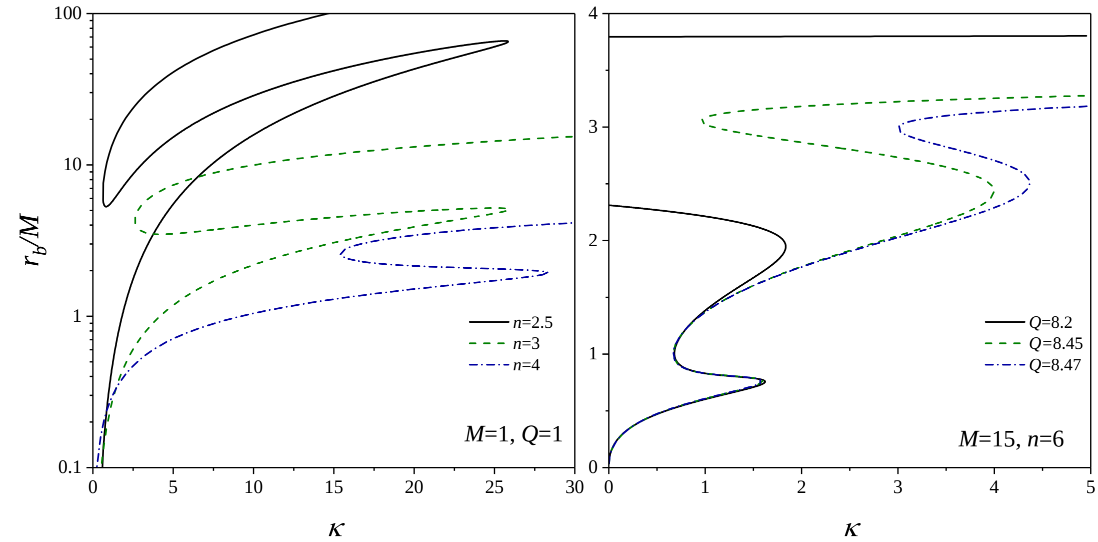

Figure 6.26: Boundary radii r_b/M of SCO regions as functions of κ for several values of n.

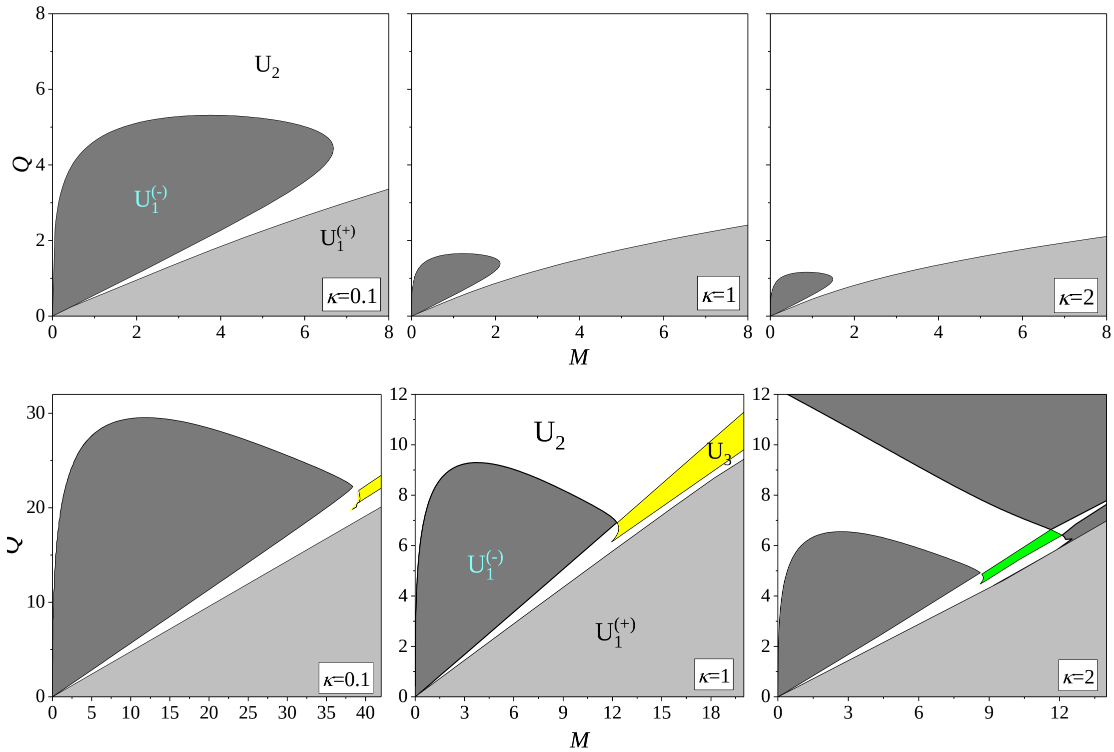

Figure 6.27: Domains of parameters on (M, Q) plane for $n = 3$(up) and $n = 6$(down) for $\kappa = 0.1, 1, 2$. The colors define the SCOD type. Gray, dark gray, white and yellow colors correspond to the $U_1^{(+)}$, $U_1^{(-)}$, U_2 and U_3 type, respectively.

Photon circular orbits

The dependencies of the radii $r_{\rm ph}$ of the photon orbits are quite similar to the case from the previous section. Some typical examples are shown in Fig. 6.28. In all cases, $r_{\rm ph} < 3M$

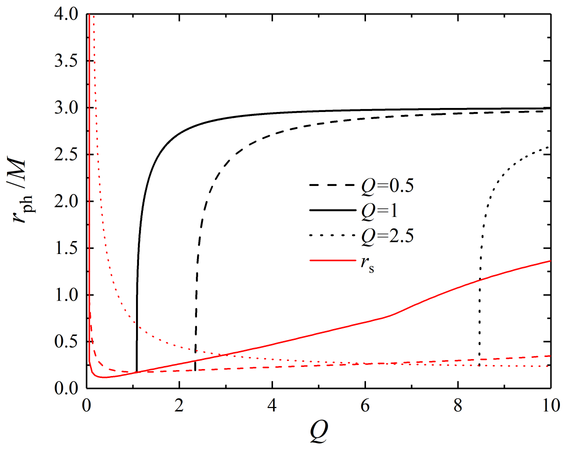

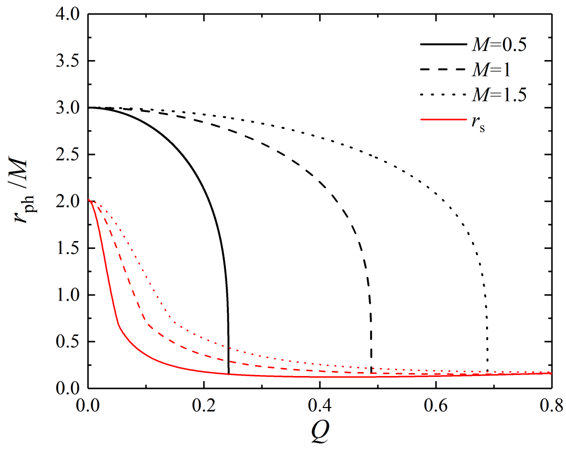

Figure 6.28: Boundary radii of the photon orbits $r_{\rm ph}$ of SCO regions as functions of Q and M for several values of M and Q, respectively.

6.4 Special exact solutions family

6.4.1 SCO distributions

The effective potential $U_{\rm eff}$ in quasi-global coordinates (4.9) is given by the expression

$$U_{\rm eff}(x, L, S) = A(r)\left(S + \frac{L^2}{R^2(x)}\right), \tag{6.24}$$

The behavior of the effective potential near the center ($x = x_0$) and the horizon of the black hole ($x = x_h$) is

$$U_{\rm eff} \sim \frac{2(x_0 - 3M)L^2}{3R'(x_0)R^3(x)}, \; x \to x_0, \quad U_{\rm eff} \to 0, \; x \to x_h, \; U_{\rm eff} \to S, \; x \to \infty. \tag{6.25}$$

In the NS case, the $U_{\rm eff} \to \infty$ for $x \to x_0$, which corresponds to presence of a repulsive barrier at the singularity, which reflect falling particles. In the BH case, particles can reach the horizon.

Similar to the previous cases, we consider the function $\tilde{L}^2$.

$$\tilde{L}^2(x) = R^2(x)\left[\frac{R(x)R'(x)A(x)}{x - 3M} - 1\right],$$

and its derivatives

$$F(x) = \frac{d}{dx}\tilde{L}^2 = \frac{f'(x)A(x)}{2R^2(x)} - 4R(x)R'(x)\,, \tag{6.26}$$

where $f(x) \equiv 2R^5(x)R'(x)/(x-3M)$.

Near the center, for $x \to x_0 + 0$, we have the following asymptotic relation

$$\tilde{L}^2 \sim -\frac{1}{3}r^2(x). \tag{6.27}$$

For $x \to \infty$, using (4.10), we obtain

$$\tilde{L}^2(x) \sim M\,x, \quad F(x) \sim M. \tag{6.28}$$

Then, if $x_0 \geq 3M$, then $\tilde{L}^2$ changes sign at some point x_m and $\tilde{L}^2 \to +\infty$ for $x \to \infty$. Therefore, there exists at least one root of $\tilde{L}^2 = L^2$, where L is the value of angular momentum.

If $x_0 < 3M$, then the radius of the horizon x_h is always $x_h < 3M$ and $\tilde{L}^2(x) \to \pm\infty$ for $x \to 3M \pm 0$. For $x \in (x_h, x_{\rm ph} = 3M)$, we have that $\tilde{L}^2(x) < 0$, which means that there are no circular orbits. On other hand, it is evident that there exists at least one minimum of $\tilde{L}^2(x)$ for $x \in (3M, \infty)$.

Also, we need to distinguish two different types of bifurcation radii. Specifically,

Type I: Bifurcation radii of SCOD are defined by the roots x_b of $F(x) = 0$.

Type II: The bifurcation radius x_m is defined by a root of $\tilde{L}^2(x) = 0$. This case corresponds to a minimum of $U_{\rm eff}$ (or $A(x)$) with $L = 0$ and can be thought of as an "antigravity" sphere [39,41], which demonstrate the repulsive character of gravity. In this case stationary particles can hang at rest over the singularity at this sphere. Below $x < x_m$, we have NECO domain.

For numerical consideration it is convenient to choose $M = 1/6$. Then we have the BH for $x_0 < 0.5$ and the NS for $x_0 \geq 0.5$, respectively. We found four possible cases, which are presented in the Tab. 6.3 and discussed in details below.

	Type	$r_{\rm stable}$	$r_{\rm unstable}$	Photon sphere
$U1$	BH	(x_1, ∞)	$(x_{\rm ph}, x_1)$	$+$
$U2$	BH	$(x_1, x_2) \cup (x_3, \infty)$	$(x_{\rm ph}, x_1) \cup (x_2, x_3)$	$+$
$S1$	NS	(x_m, ∞)	no	$-$
$S2$	NS	$(x_m, x_1) \cup (r_3, \infty)$	(x_2, r_3)	$-$

Table 6.3: Possible types of SCOD.

The results are shown in Fig. 6.29–6.32. Fig. 6.29 illustrates the effective potentials for different values of L, Fig. 6.30 illustrates typical examples of $\tilde{L}^2$

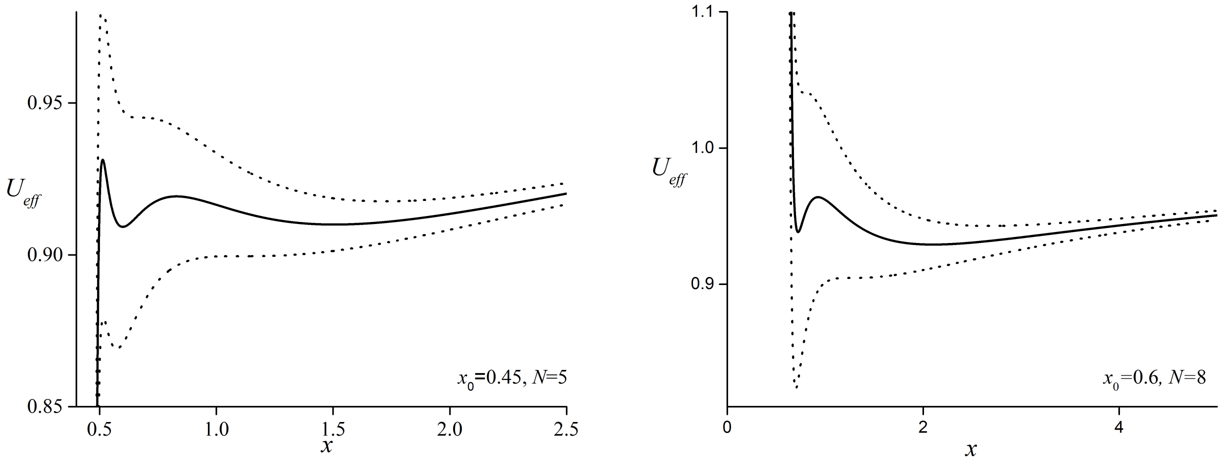

Figure 6.29: The typical examples of U_{eff} in presence of two minima for certain values of L (solid lines) in the BH case (left panel) and in the NS case (right panel) respectively.

for various values of N. The dependence of the boundary radii $r_b = R(x_b)$ on N and x_0 are shown in Figs. 6.31 and 6.32 (left panel). Additionally, in Fig. 6.32 demonstrated the parameter domains where disjoint SCODs exist. Also we need to note that in the plots we transform our quasi-global coordinate x_b to r_b (curvature coordinates).

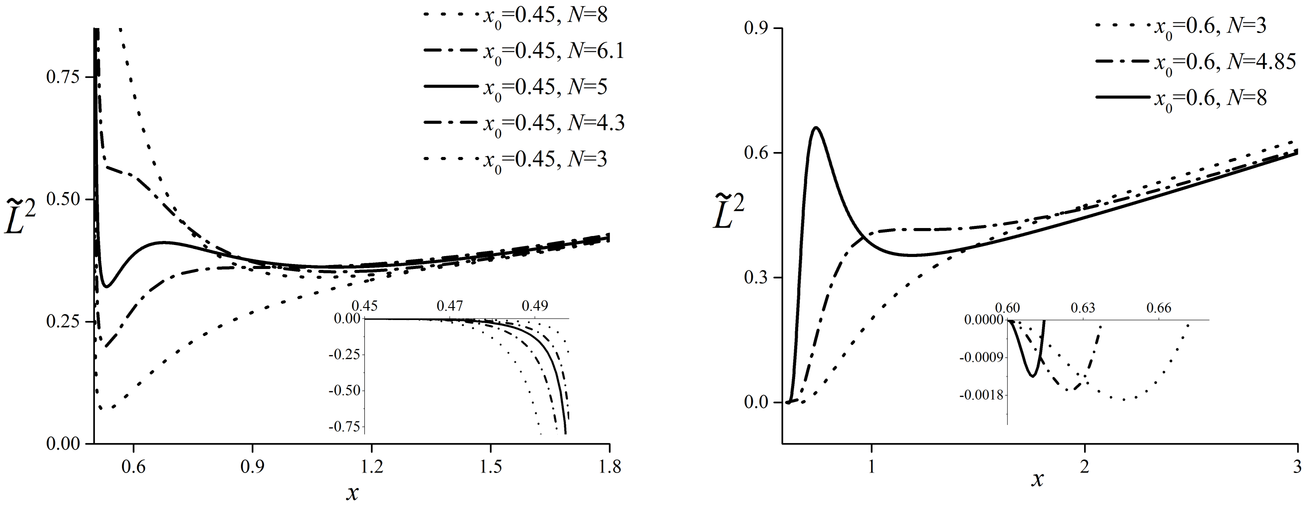

Figure 6.30: The typical examples of $\tilde{L}^2$ in the BH case (left panel) and in the NS case (right panel) respectively. In the NS case, $\tilde{L}^2 < 0$ in the small domain near the center.

Let us first consider the BH case ($x_0 < 0.5$). In this case, U_{eff} is equal to zero at the horizon and increases in the vicinity of x_h.

For the $U1$ case, which corresponds to sufficiently small x_0, the correspond-

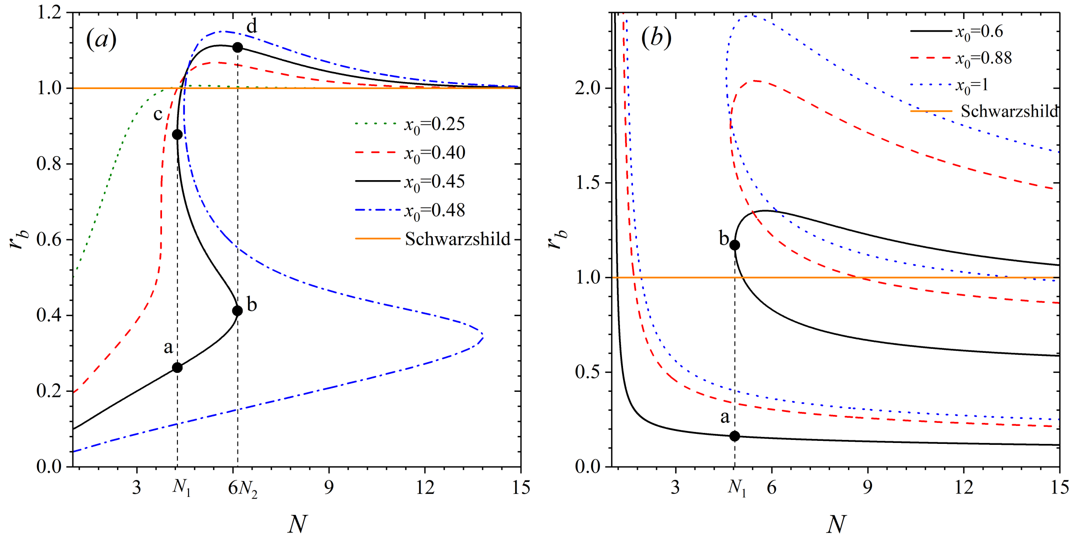

Figure 6.31: Boundary radii of SCO regions as a functions of N. (a) The BH case. In the the case of $x_0 = 0.45$ (solid) critical values of N are $N_1 = 4.3$, $N_2 = 6.1$. (b) The NS case, the lower curves corresponds to r_m (type II) radii. Two upper curves correspond to type I radii. For example, for $x_0 = 0.6$, we have $N_1 = 4.85$.

ing dependence r_b (below we use $r_b = R(x_b)$) is a single-valued. We have only one SCO domain with radii $r \in (r_1, \infty)$, similar to the case of the standard Schwarzschild BH case

In the $U2$ case, which occurs for larger values of x_0, the dependence of r_b becomes three-valued between some N_1 and N_2. For $N_1 < N < N_2$, there are two SCO domains with radii $r_b \in (r_1(N), r_2(N)) \cup (r_3(N), \infty)$ and two domains of UCO with radii $r \in (3M, r_1(N)) \cup (r_2(N), r_3(N))$.

For $N > N_2$, there is again only one root $r_3(N)$ of $F(x) = 0$. Also, it is interesting to note that $r_b \to 6M$ for $N \to \infty$.

In the NS case ($x_0 \geq 0.5$), we also have two possibilities. From Fig. 6.32 (right panel), in the $S1$ case, one can see that there exists N_1 such that for $N < N_1$, we have only one SCO domain with radii $r \in (r_m, \infty)$. The r_m corresponds to the radius of the "antigravity" sphere.

In the $S2$ case, for $N > N_1$, two additional curves r_2 and r_3 appear. We have two disjoint SCO domains with $r \in (r_m, r_1) \cup (r_2, \infty)$ and one domain of UCO with $r \in (r_1, r_2)$.

Photon circular orbits

The effective potential U_{eff} in quasi-global coordinates (6.5) for photons ($S = 0$) has following form

$$U_{\text{eff}}(x, L, S) = A(r)\frac{L^2}{R^2(x)},$$

From the condition $U'_{\text{eff}} = 0$ and (4.15), it can be seen that the radius of the

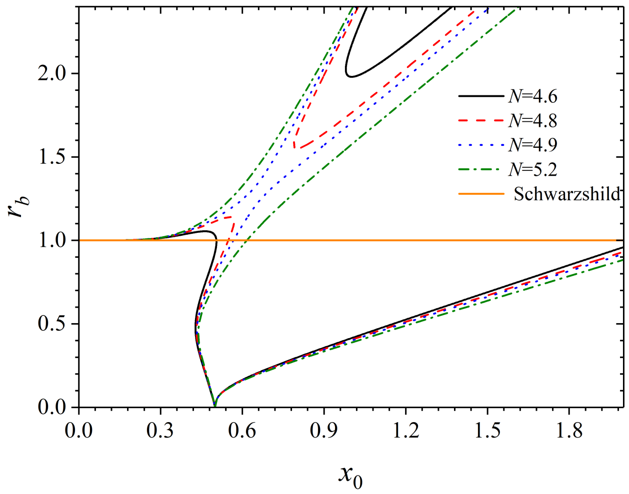

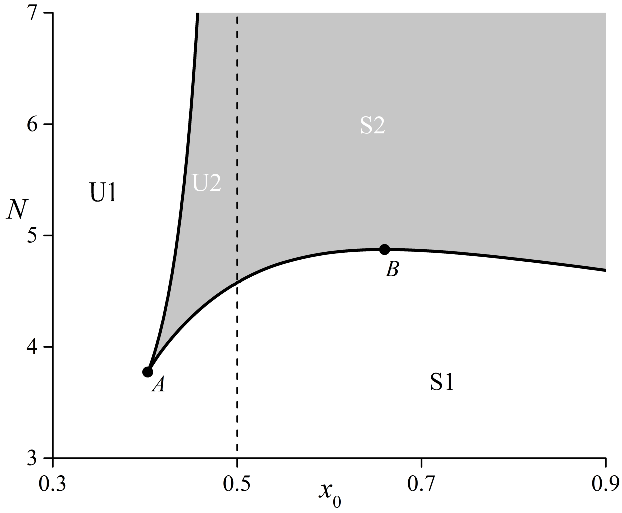

Figure 6.32: Left panel: Typical dependencies of boundary radii r_b as functions of x_0 for different values of N. The curves reshape around the critical value $N(B) = 4.87$ (see right panel). The lower parts of the curves correspond to the radii r_m (type II) for $x_0 \geq 0.5$, while the other parts correspond to type I. Right panel: The gray region shows the parameters space in which disjoint ring-like regions of SCO exist. The cusp-point A is located at $N(A) = 3.77$, $x_0(A) = 0.40$, while the maximum on the lower branch of the solid curve is at $N(B) = 4.87$, $x_0(B) = 0.66$. The vertical dashed line separates the BH and NS cases.

photon sphere determined by

$$2x - 6M = 0, \tag{6.29}$$

This leads to $x_{\text{ph}} = 3M$, and this expression doesn't depend on any parameters or on the partial choice of $R(x)$ in quasi-global coordinates. Also, it is evident that the photon sphere only exists when $x_0 < 3M$, i.e., in the BH case.

However, the corresponding radius r_{ph} in curvature coordinates, $r_{\text{ph}} = R(x_{\text{ph}})$, depends on N and x_0. This is illustrated in Fig. 6.33.

6.4.2 Keplerian AD images

We obtained Keplerian AD images for various inclination angles for the $U1$, $U2$, $S1$, and $S2$ cases. These images are shown in Figs. 6.34–6.41, where colors correspond to the normalized frequency shift (6.18).

As in previous cases, the common feature of all of these images is the presence of a dark spot in the center, which resembles the shadow of an ordinary black hole in the NS case. In the $U1$ and $U2$ cases, the dark spot corresponds to the the photon sphere, which is shown by the dashed white

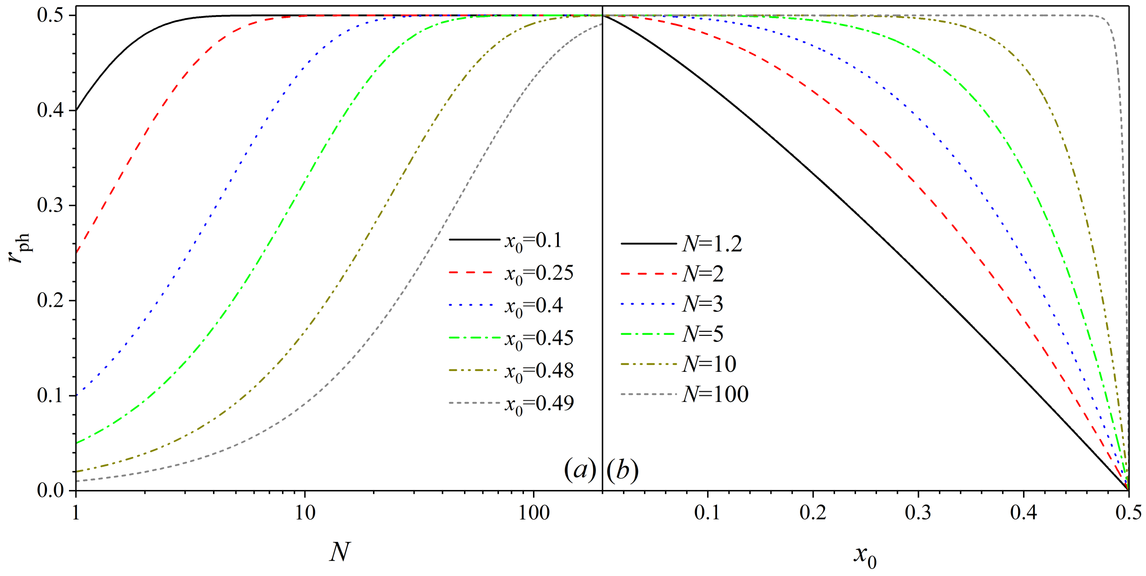

Figure 6.33: The photon orbits radii in Schwarzschild-like coordinates as a functions of (a) N and (b) x_0.

line. In the $S1$ and $S2$ cases, we also have a dark spot in the center, but it results from the repulsive nature of the naked singularity.

We need to note that for small inclination angles, the $S1$ case can look similar to the $U2$ case with the same inclination due to the existing of the inner ring, which corresponds to the outer edge of the disk. For large enough inclination, they can be recognized by the presence or absence of the crescent-like dark spot.

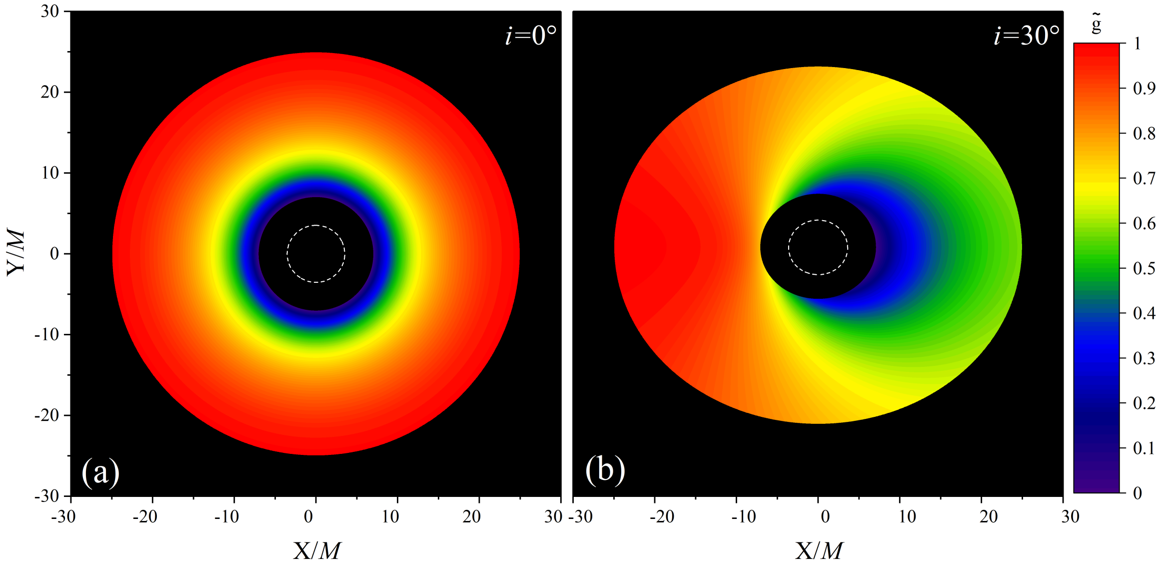

Figure 6.34: Direct Keplerian disk images for the $U1$ type ($x_0 = 0.48$, $N = 15$) in full face and for inclination $i = 30^o$. The dashed white line corresponds to the image of the photon sphere at $r_{\rm ph}/M = 1.37$. The ISCO located at $r_{\rm b}/M = 6.03$

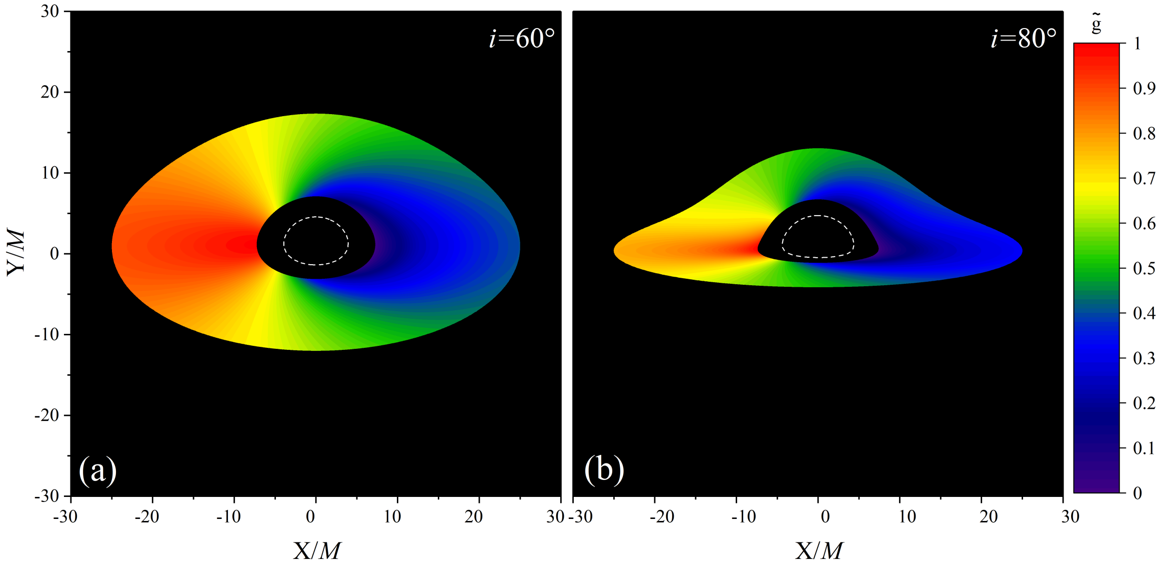

Figure 6.35: The same as in Fig. 6.34 but for 60° and 80° inclination angles.

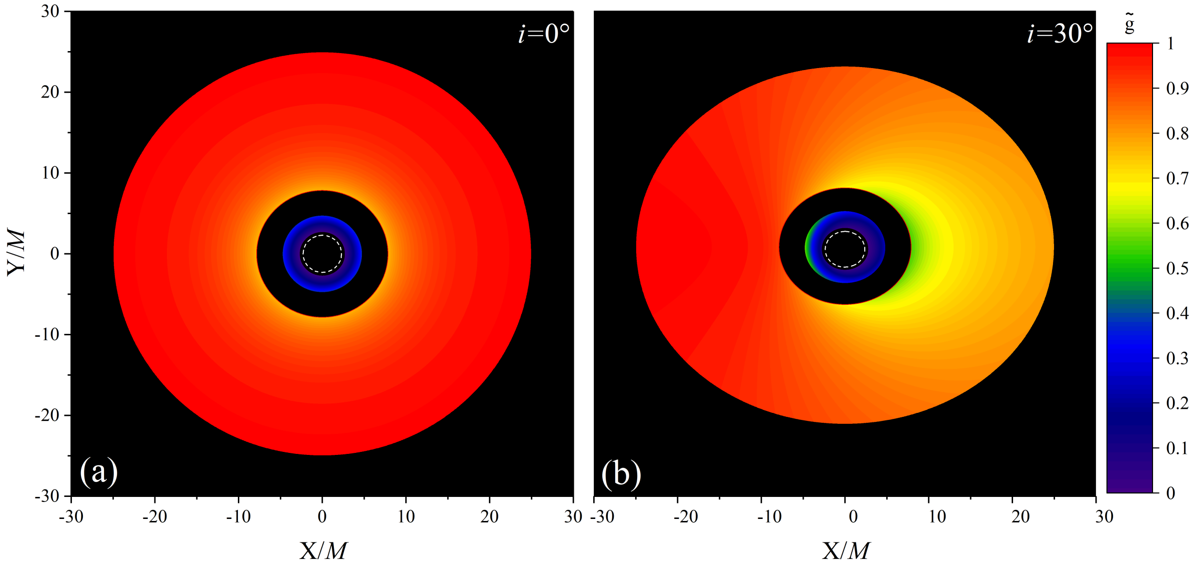

Figure 6.36: Direct Keplerian AD images for the $U2$ type ($x_0 = 0.48$, $N = 6$) in full face and for inclination $i = 30°$. The dashed white line corresponds to the image of the photon sphere at $r_{\rm ph}/M = 0.65$. The SCOs form two disjoint domain with radii of the inner part $r/M \in (0.89, 3.54)$ and for the outer part $r \in (6.88, \infty)$.

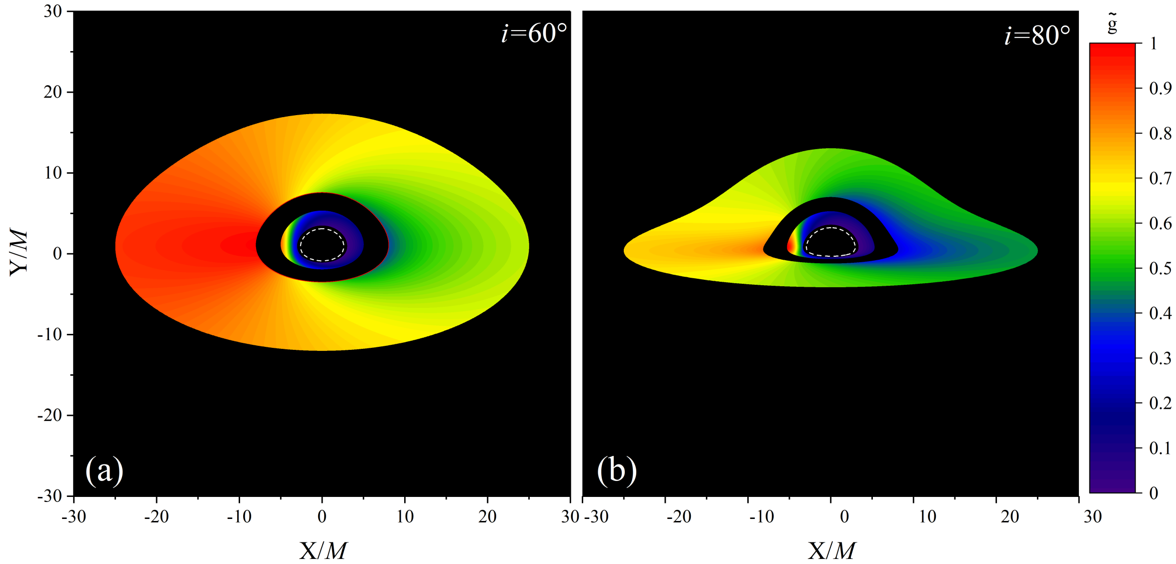

Figure 6.37: The same as in Fig. 6.36 but for 60° and 80° inclination angles.

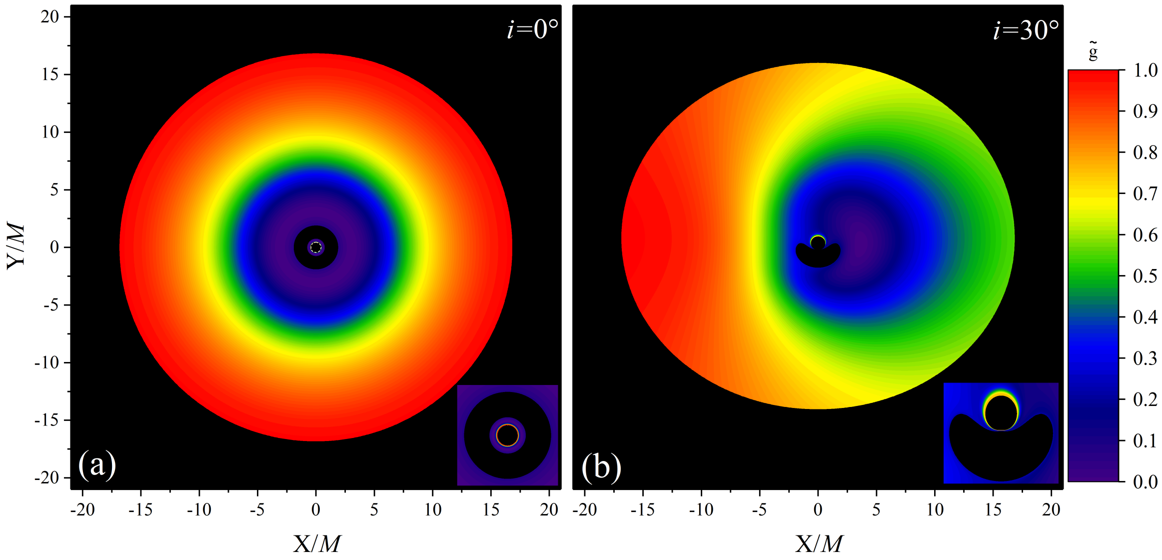

Figure 6.38: Direct Keplerian AD images for the $S1$ type ($x_0 = 0.6$, $N = 3$) in full face and for inclination $i = 30^o$. The dark spot in the center appears due to the repulsive character of the singularity.

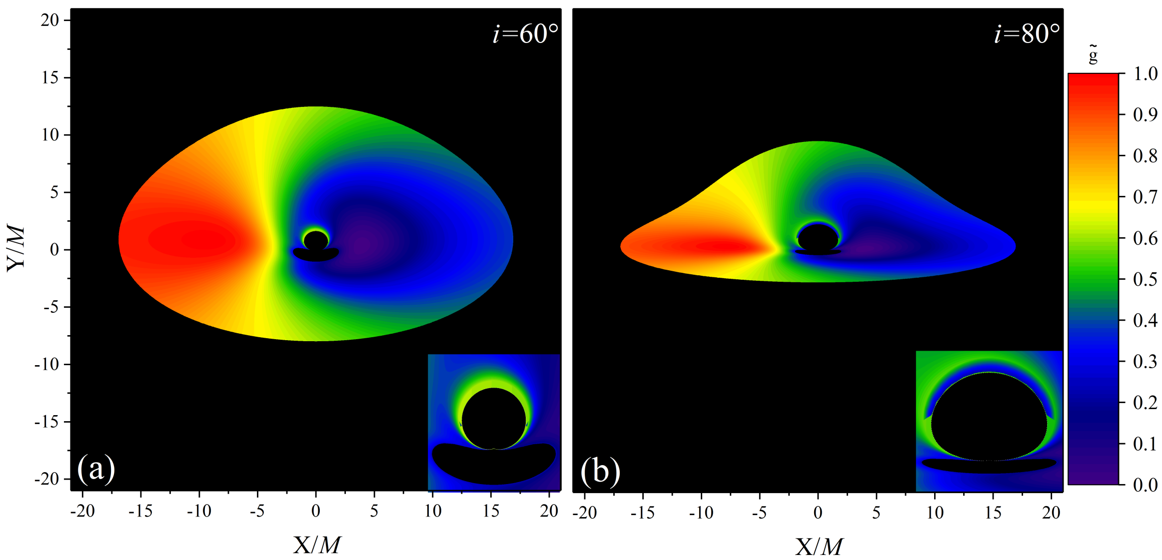

Figure 6.39: The same as in Fig. 6.38 but for 60° and 80° inclination angles.

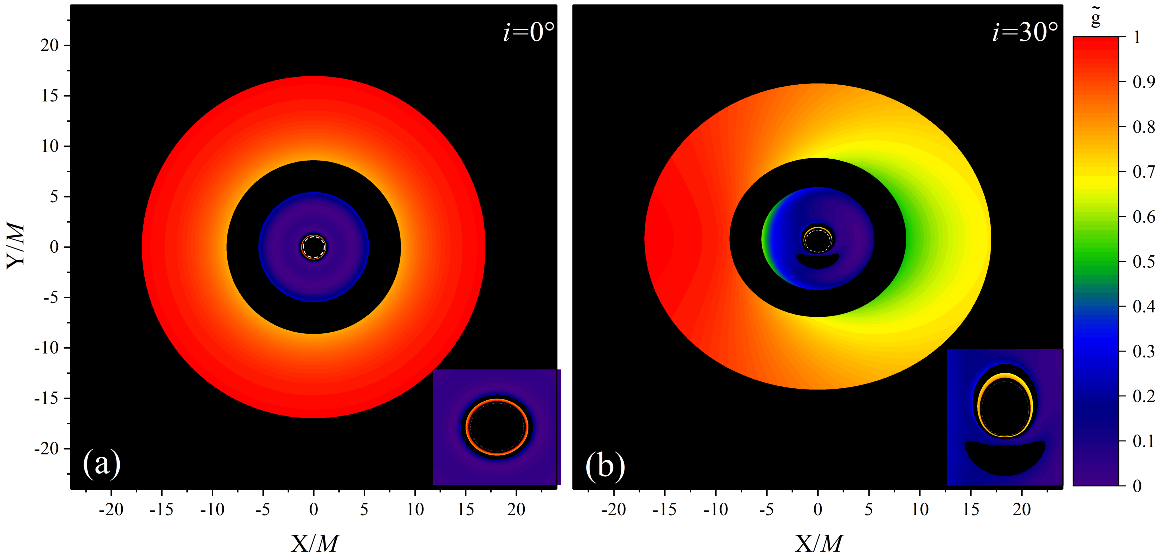

Figure 6.40: Direct Keplerian AD images for the $S2$ type ($x_0 = 0.6$, $N = 8$) in full face and for inclination $i = 30°$. The SCOs form two disjoint domain with radii of the inner part $r/M \in (0.84, 4.21)$ and for the outer part $r \in (7.62, \infty)$.

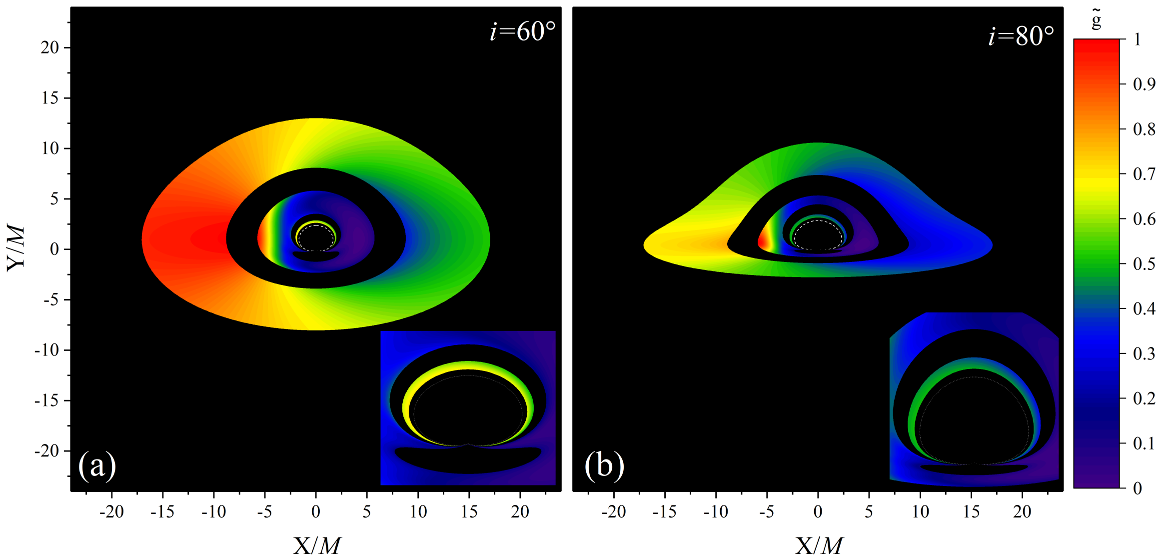

Figure 6.41: The same as in Fig. 6.40 but for 60° and 80° inclination angles.

Chapter 7

Conclusions

In this thesis we presented a detailed consideration of both qualitative and quantitative properties of static spherically-symmetric solutions of the Einstein equations with self-interacting scalar fields. Our focus was placed on solutions with naked singularities.

In Chapter 2, we studied the qualitative properties of the solutions of the Einstein equations with real static self-interacting N scalar fields. We assumed that the self-interaction potential is positive-defined, monotonic, and exponentially-bounded. Under these conditions, we provided a rigorous proof that the corresponding solutions will be regular up to $r = 0$. Also we found the rigorous form of asymptotic solutions near the singularity. Then a specific case of a self-interaction potential in the form $V(\phi) = w\phi^{2n}$ was numerically studied to illustrate our results. Further, we demonstrated the convergence to the unique solution of the iterative procedure of solving the Einstein–SF equations with inital conditions in form of asymptotic solutions at spatial infinity.

In Chapter 3 we provided some examples, where spherical singularities arise at $r = r_s \neq 0$ in the curvature coordinates. First, we demonstrated the possibility of such solutions for static spherically-symmetric scalar field with a self-interaction potential $V(\phi) = w\phi^{2n}$ on the Minkowski background. This outcome does not contradict to the results of Chapter 2, where such singularities were suppressed by gravity, but shows that these can be violated in a more general case. In the section 3.2, we relinquished the assumption of exponential boundedness for $V(\phi)$ and constructed an exact example where the spherical singularities can arise in the solutions to the Einstein-SF equations. We derived the asymptotical solutions near the singularity and then confirmed it numerically. Additionally, we explored the dependencies of the singularity radii r_s on different configuration parameters.

In Chapter 3, we considered some exact solutions of the Einstein-SF equations. We found a generalization of the Fisher-Janis-Newmann-Winicour solution in the case of N scalar fields. The form of the metric is absolutely the same as in the case of a single scalar field, but now the scalar charge is equal to the sum of scalar charges of the separate scalar fields. In Section 4.2, we constructed an exact "toy-model" solution which represents a two-parameter family, which includes naked singularities and hairy black holes.

In Chapter 5, we studied the stability of the previously considered solutions against odd-parity gravitational perturbations and also found the fundamental quasi-normal modes frequencies. We demonstrated that these solutions are stable. Our numerical study in case of the scalar field with the power-law self-interaction potential shows that the fundamental QNMs frequencies differ from the standard Schwarzschild black hole case. The same situation is in case of the exponentially unbounded self-interaction potentials. However, they can be close to corresponding values in the linear massless SF case, but without converging to them for lower values of l.

We studied special exact examples of the scalar field potential in a form of Mexican hat, describing black holes that can be negative near the horizon. However, we did not find any exponentially growing modes in the time-domain profiles. For these examples, the the fundamental quasinormal mode frequencies have an intriguing behaviour corresponding to the occurrence of discontinuities in the ω-trajectories in the complex plane, both in the case of a black hole and a naked singularity.

In Section 5.5, we revisited the stability of the test fields in the background of a Kehagias-Sfetsos naked singularity. Previous studies by other authors contained erroneous statements, and required a revision of their results. In this regard, we demonstrated absence of exponentially growing modes in time-domain profiles for $l > 1$ and found correct values for the fundamental QNM frequencies for scalar, vector, and Dirac test fields.

Finally, in Chapter 6, we studied in details particles motion in vicinity of previously considered solutions. Mainly we were interested in considering properties of the distribution of stable circular orbits around the corresponding configurations and images of the accretion disk for a distant observer. For all cases we found possible types of stable circular orbit distributions and domains of parameters where they are realized.

We also demonstrated that the presence of self-interaction can lead to a new type of circular orbit distributions, which is absent in the linear massless scalar field case. We built the Keplerian disk images in the plane of a distant observer and demonstrated the possibility to mimic the black holes shadows.

Bibliography

[1] Robert M. Wald. Dynamics in nonglobally hyperbolic, static spacetimes. *Journal of Mathematical Physics*, 21(12):2802–2805, December 1980.

[2] Avijit Chowdhury, Saraswati Devi, and Sayan Chakrabarti. Naked singularity in 4d einstein-gauss-bonnet novel gravity: Echoes and instability. *Phys. Rev. D*, 106:024023, Jul 2022.

[3] Clifford M. Will. The confrontation between general relativity and experiment. *Living Reviews in Relativity*, 17(1), jun 2014.

[4] Emanuele Berti, Enrico Barausse, Vitor Cardoso, and et al. Testing general relativity with present and future astrophysical observations. *Classical and Quantum Gravity*, 32(24):243001, dec 2015.

[5] M. Kramer, I. H. Stairs, R. N. Manchester, Wex, and et al. Strong-field gravity tests with the double pulsar. *Phys. Rev. X*, 11:041050, Dec 2021.

[6] Sourabh Nampalliwar. Strong field tests of gravity with electromagnetic and gravitational waves, 2021.

[7] Sebastian H Völkel, Enrico Barausse, Nicola Franchini, and Avery E Broderick. EHT tests of the strong-field regime of general relativity. *Classical and Quantum Gravity*, 38(21):21LT01, oct 2021.

[8] B. P. Abbott, R. Abbott, T. D. Abbott, and M. et al. Observation of gravitational waves from a binary black hole merger. *Physical Review Letters*, 116(6), feb 2016.

[9] Event Horizon Telescope Collaboration. First M87 Event Horizon Telescope Results. I. The Shadow of the Supermassive Black Hole. *The Astrophysical Journal*, 875(1):L1, apr 2019.

[10] Event Horizon Telescope Collaboration. First Sagittarius A* Event Horizon Telescope Results. I. The Shadow of the Supermassive Black Hole in the Center of the Milky Way. *ApJL*, 930(2):L12, May 2022.

[11] Event Horizon Telescope Collaboration. *ApJL*, 930(2):L14, May 2022.

[12] Elcio Abdalla, Guillermo Franco Abellán, and Amin Aboubrahim et al. Cosmology intertwined: A review of the particle physics, astrophysics, and cosmology associated with the cosmological tensions and anomalies. *Journal of High Energy Astrophysics*, 34:49–211, jun 2022.

[13] Ivan Debono and George F. Smoot. General relativity and cosmology: Unsolved questions and future directions. *Universe*, 2(4), 2016.

[14] Timothy Clifton, Pedro G. Ferreira, Antonio Padilla, and Constantinos Skordis. Modified gravity and cosmology. *Physics Reports*, 513(1-3):1–189, mar 2012.

[15] Salvatore Capozziello and Mariafelicia De Laurentis. Extended theories of gravity. *Physics Reports*, 509(4):167–321, 2011.

[16] Emmanuel N. Saridakis, Ruth Lazkoz, Vincenzo Salzano, Paulo Vargas Moniz, Salvatore Capozziello, and et al. Modified gravity and cosmology: An update by the cantata network. 2023.

[17] I. Z. Fisher. Scalar mesostatic field with regard for gravitational effects. *Zh. Exp. Theor. Phys.*, 18:636–640, 1948.

[18] Eric G. Gimon and Petr Hořava. Astrophysical violations of the kerr bound as a possible signature of string theory. *Physics Letters B*, 672(3):299–302, feb 2009.

[19] Cosimo Bambi and Dejan Stojkovic. Astrophysical wormholes. *Universe*, 7(5):136, may 2021.

[20] Steven L. Liebling and Carlos Palenzuela. Dynamical boson stars. *Living Reviews in Relativity*, 26(1), feb 2023.

[21] Luca Visinelli. Boson stars and oscillatons: A review. *International Journal of Modern Physics D*, 30(15), nov 2021.

[22] Felix Finster, Joel Smoller, and Shing-Tung Yau. Particlelike solutions of the einstein-dirac equations. *Physical Review D*, 59(10), apr 1999.

[23] Jose Luis Blázquez-Salcedo, Christian Knoll, and Eugen Radu. Boson and dirac stars in d4 dimensions. *Physics Letters B*, 793:161–168, 2019.

[24] Pawel O. Mazur and Emil Mottola. Gravitational condensate stars: An alternative to black holes. *Universe*, 9(2):88, feb 2023.

[25] Vitor Cardoso and Paolo Pani. Testing the nature of dark compact objects: a status report. *Living Reviews in Relativity*, 22(1), jul 2019.

[26] Hector Olivares, Ziri Younsi, Christian M Fromm, Mariafelicia De Laurentis, Oliver Porth, Yosuke Mizuno, Heino Falcke, Michael Kramer, and Luciano Rezzolla. How to tell an accreting boson star from a black hole. *Monthly Notices of the Royal Astronomical Society*, 497(1):521–535, Jul 2020.

[27] Karim Van Aelst, Eric Gourgoulhon, and Frederic H. Vincent. Orbits and images of cubic galileon black holes. 2021.

[28] Carlos A.R. Herdeiro, Alexandre M. Pombo, Eugen Radu, Pedro V.P. Cunha, and Nicolas Sanchis-Gual. The imitation game: Proca stars that can mimic the schwarzschild shadow. *Journal of Cosmology and Astroparticle Physics*, 2021(04):051, Apr 2021.

[29] Askar B. Abdikamalov, Ahmadjon A. Abdujabbarov, Dimitry Ayzenberg, Daniele Malafarina, Cosimo Bambi, and Bobomurat Ahmedov. Black hole mimicker hiding in the shadow: Optical properties of the metric. *Physical Review D*, 100(2), Jul 2019.

[30] Indrani Banerjee, Sumanta Chakraborty, and Soumitra SenGupta. Silhouette of m87*: A new window to peek into the world of hidden dimensions. *Physical Review D*, 101(4), Feb 2020.

[31] Indrani Banerjee, Subhadip Sau, and Soumitra SenGupta. Implications of axionic hair on the shadow of m87*. *Physical Review D*, 101(10), May 2020.

[32] Subhadip Sau, Indrani Banerjee, and Soumitra SenGupta. Imprints of the janis-newman-winicour spacetime on observations related to shadow and accretion. *Physical Review D*, 102(6), Sep 2020.

[33] F. H. Vincent, M. Wielgus, M. A. Abramowicz, E. Gourgoulhon, J.-P. Lasota, T. Paumard, and G. Perrin. Geometric modeling of m87* as a kerr black hole or a non-kerr compact object. *Astronomy & Astrophysics*, 646:A37, Feb 2021.

[34] Prashant Kocherlakota, Luciano Rezzolla, Heino Falcke, and Christian M. Fromm et al. Constraints on black-hole charges with the 2017 EHT observations of m87$*. Physical Review D, 103(10), may$2021.

[35] Sunny Vagnozzi and Luca Visinelli. Hunting for extra dimensions in the shadow of $m87^*$. *Phys. Rev. D*, 100:024020, Jul 2019.

[36] Daniela Pugliese, Hernando Quevedo, and Remo Ruffini. Circular motion of neutral test particles in reissner-nordström spacetime. *Physical Review D*, 83(2), Jan 2011.

[37] Daniela Pugliese, Hernando Quevedo, and Remo Ruffini. Equatorial circular orbits of neutral test particles in the kerr-newman spacetime. *Physical Review D*, 88(2), Jul 2013.

[38] Petr Slaný and Zdeněk Stuchlík. Equatorial circular orbits in Kerr-Newman-de Sitter spacetimes. *European Physical Journal C*, 80(6):587, June 2020.

[39] Zdeněk Stuchlík and Jan Schee. Circular geodesic of bardeen and ayon–beato–garcia regular black-hole and no-horizon spacetimes. *International Journal of Modern Physics D*, 24(02):1550020, Feb 2015.

[40] Irina Dymnikova and Anna Poszwa. Classification and basic properties of circular orbits around regular black holes and solitons with the de sitter center. *Classical and Quantum Gravity*, 36(10):105002, apr 2019.

[41] Ronaldo S.S. Vieira, Jan Schee, Włodek Kluźniak, Zdeněk Stuchlík, and Marek Abramowicz. Circular geodesics of naked singularities in the kehagias-sfetsos metric of hořava's gravity. *Physical Review D*, 90(2), Jul 2014.

[42] Allah Ditta, Xia Tiecheng, Saadia Mumtaz, Farruh Atamurotov, G. Mustafa, and Ahmadjon Abdujabbarov. Testing metric-affine gravity using particle dynamics and photon motion. *Physics of the Dark Universe*, 41:101248, August 2023.

[43] Sanjar Shaymatov, Pankaj Sheoran, and Sanjay Siwach. Motion of charged and spinning particles influenced by dark matter field surrounding a charged dyonic black hole. *Phys. Rev. D*, 105(10):104059, May 2022.

[44] Bobir Toshmatov. Circular orbits of particles around parameterized black hole. *Physics of the Dark Universe*, 35:100992, March 2022.

[45] João Luís Rosa. Observational properties of relativistic fluid spheres with thin accretion disks. *Phys. Rev. D*, 107:084048, Apr 2023.

[46] A. M. Al Zahrani. Circular orbits of charged particles around a weakly charged and magnetized Schwarzschild black hole. *Phys. Rev. D*, 103(8):084008, April 2021.

[47] Sunny Vagnozzi, Rittick Roy, Yu-Dai Tsai, Luca Visinelli, Misba Afrin, and et al Allahyari. Horizon-scale tests of gravity theories and fundamental physics from the Event Horizon Telescope image of Sagittarius A*. *arXiv e-prints*, page arXiv:2205.07787, May 2022.

[48] O. S. Stashko and V. I. Zhdanov. Black hole mimickers in astrophysical configurations with scalar fields. *Ukrainian Journal of Physics*, 64(11):1078, Nov. 2019.

[49] O. Stashko and V. Zhdanov. Spherically symmetric configurations in general relativity in the presence of a linear massive scalar field: Separation of a distribution of test body circular orbits. *Ukrainian Journal of Physics*, 64(3):189, Apr. 2019.

[50] Jan Schee and Zdeněk Stuchlík. Profiled spectral lines generated by keplerian discs orbiting in the bardeen and ayòn-beato–garcìa spacetimes. *Classical and Quantum Gravity*, 33(8):085004, Mar 2016.

[51] Galin Gyulchev, Petya Nedkova, Tsvetan Vetsov, and Stoytcho Yazadjiev. Image of the janis-newman-winicour naked singularity with a thin accretion disk. *Physical Review D*, 100(2), Jul 2019.

[52] Galin Gyulchev, Jutta Kunz, Petya Nedkova, Tsvetan Vetsov, and Stoytcho Yazadjiev. Observational signatures of strongly naked singularities: image of the thin accretion disk. *The European Physical Journal C*, 80(11), Nov 2020.

[53] Yu-Xiang Huang, Sen Guo, Yu-Hao Cui, Qing-Quan Jiang, and Kai Lin. Influence of accretion disk on the optical appearance of the kazakov-solodukhin black hole. *Phys. Rev. D*, 107:123009, Jun 2023.

[54] Akhil Uniyal, Reggie C. Pantig, and Ali Övgün. Probing a non-linear electrodynamics black hole with thin accretion disk, shadow, and deflection angle with M87* and Sgr A* from EHT. *Physics of the Dark Universe*, 40:101178, May 2023.

[55] Igor Bogush, Dmitri Gal'tsov, Galin Gyulchev, Kirill Kobialko, Petya Nedkova, and Tsvetan Vetsov. Photon surfaces, shadows, and accretion disks in gravity with minimally coupled scalar field. *Phys. Rev. D*, 106(2):024034, July 2022.

[56] Suvankar Paul, Rajibul Shaikh, Pritam Banerjee, and Tapobrata Sarkar. Observational signatures of wormholes with thin accretion disks. *JCAP*, 2020(3):055, March 2020.

[57] Xi-Jing Wang, Xiao-Mei Kuang, Yuan Meng, Bin Wang, and Jian-Pin Wu. Rings and images of Horndeski hairy black hole illuminated by various thin accretions. *Phys. Rev. D*, 107(12):124052, June 2023.

[58] Qingyu Gan, Peng Wang, Houwen Wu, and Haitang Yang. Photon spheres and spherical accretion image of a hairy black hole. *Phys. Rev. D*, 104(2):024003, July 2021.

[59] Temurbek Mirzaev, Song Li, Bakhtiyor Narzilloev, Ibrar Hussain, Ahmadjon Abdujabbarov, and Bobomurat Ahmedov. Simulated image of the shadow of the Kerr-Newman-NUT-Kiselev black hole in the Rastall gravity with a thin accretion disk. *European Physical Journal Plus*, 138(1):47, January 2023.

[60] Jun-Qi Guo, Pankaj S. Joshi, Ramesh Narayan, and Lin Zhang. Accretion disks around naked singularities. *Classical and Quantum Gravity*, 38(3):035012, February 2021.

[61] Kourosh Nozari, Sara Saghafi, and Fateme Aliyan. Accretion onto a static spherically symmetric regular MOG dark compact object. *European Physical Journal C*, 83(5):449, May 2023.

[62] Kaushik Bhattacharya, Dipanjan Dey, Arindam Mazumdar, and Tapobrata Sarkar. New class of naked singularities and their observational signatures. *Phys. Rev. D*, 101:043005, Feb 2020.

[63] Z. Kovács and T. Harko. Can accretion disk properties observationally distinguish black holes from naked singularities? *Phys. Rev. D*, 82(12):124047, December 2010.

[64] C. S. J. Pun, Z. Kovács, and T. Harko. Thin accretion disks onto brane world black holes. *Phys. Rev. D*, 78(8):084015, October 2008.

[65] Tiberiu Harko, Zoltán Kovács, and Francisco S. N. Lobo. Testing Hořava-Lifshitz gravity using thin accretion disk properties. *Phys. Rev. D*, 80(4):044021, August 2009.

[66] Shokoufe Faraji and Eva Hackmann. Thin accretion disk around the distorted Schwarzschild black hole. *Phys. Rev. D*, 101(2):023002, January 2020.

[67] Lucas G. Collodel, Daniela D. Doneva, and Stoytcho S. Yazadjiev. Circular Orbit Structure and Thin Accretion Disks around Kerr Black Holes with Scalar Hair. *ApJ*, 910(1):52, March 2021.

[68] Mohaddese Heydari-Fard and Hamid Reza Sepangi. Thin accretion disk signatures of scalarized black holes in Einstein-scalar-Gauss-Bonnet gravity. *Physics Letters B*, 816:136276, May 2021.

[69] Zheng Cao, Alejandro Cárdenas-Avendaño, Menglei Zhou, Cosimo Bambi, Carlos A. R. Herdeiro, and Eugen Radu. Iron Kα line of boson stars. *JCAP*, 2016(10):003, October 2016.

[70] Honghui Liu, Menglei Zhou, and Cosimo Bambi. Distinguishing black holes and naked singularities with iron line spectroscopy. *JCAP*, 2018(8):044, August 2018.

[71] Jinye Yang, Dimitry Ayzenberg, and Cosimo Bambi. Iron line spectroscopy of black holes in vector-tensor Galileon modified gravity. *Phys. Rev. D*, 98(4):044024, August 2018.

[72] Niccolò Bucciantini and Jacopo Soldateschi. Iron line from neutron star accretion discs in scalar tensor theories. , 495(1):L56–L60, June 2020.

[73] Tianling Shen, Menglei Zhou, Cosimo Bambi, Carlos A. R. Herdeiro, and Eugen Radu. Iron Kα line of Proca stars. *JCAP*, 2017(8):014, August 2017.

[74] Menglei Zhou, Cosimo Bambi, Carlos A. R. Herdeiro, and Eugen Radu. Iron K α line of Kerr black holes with Proca hair. *Phys. Rev. D*, 95(10):104035, May 2017.

[75] Hao Zhang, Menglei Zhou, Cosimo Bambi, Burkhard Kleihaus, Jutta Kunz, and Eugen Radu. Testing Einstein-dilaton-Gauss-Bonnet gravity with the reflection spectrum of accreting black holes. *Phys. Rev. D*, 95(10):104043, May 2017.

[76] Pedro V. P. Cunha, José A. Font, Carlos Herdeiro, Eugen Radu, Nicolas Sanchis-Gual, and Miguel Zilhão. Lensing and dynamics of ultracompact bosonic stars. *Phys. Rev. D*, 96(10):104040, November 2017.

[77] Yiqian Chen, Peng Wang, Houwen Wu, and Haitang Yang. Gravitational Lensing by Born-Infeld Naked Singularities. *arXiv e-prints*, page arXiv:2305.17411, May 2023.

[78] Farruh Atamurotov and Sushant G. Ghosh. Gravitational weak lensing by a naked singularity in plasma. *European Physical Journal Plus*, 137(6):662, June 2022.

[79] Naoki Tsukamoto. Gravitational lensing by a photon sphere in a Reissner-Nordström naked singularity spacetime in strong deflection limits. *Phys. Rev. D*, 104(12):124016, December 2021.

[80] Gulmina Zaman Babar, Farruh Atamurotov, Abdullah Zaman Babar, and Yen-Kheng Lim. Retrolensing by a spherically symmetric naked singularity. *arXiv e-prints*, page arXiv:2104.01340, April 2021.

[81] Suvankar Paul. Strong gravitational lensing by a strongly naked null singularity. *Phys. Rev. D*, 102(6):064045, September 2020.

[82] Shangyun Wang, Songbai Chen, and Jiliang Jing. Strong gravitational lensing by a Konoplya-Zhidenko rotating non-Kerr compact object. *JCAP*, 2016(11):020, November 2016.

[83] Hossein Ghaffarnejad and Hassan niad. Weak Gravitational Lensing from Regular Bardeen Black Holes. *International Journal of Theoretical Physics*, 55(3):1492–1505, March 2016.

[84] Songbai Chen and Jiliang Jing. Strong gravitational lensing by a rotating non-Kerr compact object. *Phys. Rev. D*, 85(12):124029, June 2012.

[85] Hans-Peter Nollert. TOPICAL REVIEW: Quasinormal modes: the characteristic 'sound' of black holes and neutron stars. *Classical and Quantum Gravity*, 16(12):R159–R216, December 1999.

[86] Emanuele Berti, Vitor Cardoso, and Andrei O. Starinets. TOPICAL REVIEW: Quasinormal modes of black holes and black branes. *Classical and Quantum Gravity*, 26(16):163001, August 2009.

[87] R. A. Konoplya and Alexander Zhidenko. Quasinormal modes of black holes: From astrophysics to string theory. *Rev. Mod. Phys.*, 83:793–836, Jul 2011.

[88] Zachary Mark, Aaron Zimmerman, Song Ming Du, and Yanbei Chen. A recipe for echoes from exotic compact objects. *Physical Review D*, 96(8), oct 2017.

[89] Aaron Zimmerman, Richard N. George, and Yanbei Chen. Rogue echoes from exotic compact objects. *arXiv e-prints*, page arXiv:2306.11166, June 2023.

[90] Randy S. Conklin, Bob Holdom, and Jing Ren. Gravitational wave echoes through new windows. *Phys. Rev. D*, 98(4):044021, August 2018.

[91] Vitor Cardoso and Paolo Pani. Tests for the existence of horizons through gravitational wave echoes. *arXiv e-prints*, page arXiv:1709.01525, September 2017.

[92] K. G. Arun, Enis Belgacem, Robert Benkel, and Laura Bernard et al. New horizons for fundamental physics with LISA. *Living Reviews in Relativity*, 25(1), jun 2022.

[93] Y. Fujii and K. Maeda. *The scalar-tensor theory of gravitation*. Cambridge Monographs on Mathematical Physics. Cambridge University Press, 7 2007.

[94] Israel Quiros. Selected topics in scalar–tensor theories and beyond. *International Journal of Modern Physics D*, 28(07):1930012, may 2019.

[95] Thomas P. Sotiriou. Gravity and scalar fields. In *Modifications of Einstein's Theory of Gravity at Large Distances*, pages 3–24. Springer International Publishing, oct 2014.

[96] Shinji Tsujikawa. Quintessence: a review. *Classical and Quantum Gravity*, 30(21):214003, oct 2013.

[97] L. Arturo Ureña-López. Brief review on scalar field dark matter models. *Frontiers in Astronomy and Space Sciences*, 6:47, July 2019.

[98] Andrei Linde. Inflationary cosmology after planck 2013. 2014.

[99] Jerome Martin, Christophe Ringeval, and Vincent Vennin. Encyclopaedia inflationaris. 2023.

[100] Roger Penrose. Gravitational Collapse and Space-Time Singularities. *Physical Review Letters*, 14(3):57–59, jan 1965.

[101] R. Penrose. "Golden Oldie": Gravitational Collapse: The Role of General Relativity. *General Relativity and Gravitation*, 34(7):1141–1165, jul 2002.

[102] Demetrios Christodoulou. Violation of cosmic censorship in the gravitational collapse of a dust cloud. *Communications in Mathematical Physics*, 93(2):171–195, jun 1984.

[103] Amos Ori and Tsvi Piran. Naked singularities in self-similar spherical gravitational collapse. *Physical Review Letters*, 59(19):2137–2140, nov 1987.

[104] P. S. Joshi and I. H. Dwivedi. Naked singularities in spherically symmetric inhomogeneous Tolman-Bondi dust cloud collapse. *Physical Review D*, 47(12):5357–5369, jun 1993.

[105] Tomohiro Harada. Gravitational collapse and naked singularities. *Pramana*, 63(4):741–753, oct 2004.

[106] Allen I. Janis, Ezra T. Newman, and Jeffrey Winicour. Reality of the Schwarzschild Singularity. *PRL*, 20(16):878–880, April 1968.

[107] Max Wyman. Static spherically symmetric scalar fields in general relativity. *Phys. Rev. D*, 24:839–841, Aug 1981.

[108] K. S. Virbhadra. Janis–newman–winicour and wyman solutions are the same. *International Journal of Modern Physics A*, 12(27):4831–4835, Oct 1997.

[109] Parth Bambhaniya, Ashok B. Joshi, Dipanjan Dey, and Pankaj S. Joshi. Timelike geodesics in naked singularity and black hole spacetimes. *Physical Review D*, 100(12), Dec 2019.

[110] Rajibul Shaikh and Pankaj S. Joshi. Can we distinguish black holes from naked singularities by the images of their accretion disks? *Journal of Cosmology and Astroparticle Physics*, 2019(10):064–064, oct 2019.

[111] Anirban N. Chowdhury, Mandar Patil, Daniele Malafarina, and Pankaj S. Joshi. Circular geodesics and accretion disks in the janis-newman-winicour and gamma metric spacetimes. *Physical Review D*, 85(10), May 2012.

[112] Sheng Zhou, Ruanjing Zhang, Juhua Chen, and Yongjiu Wang. Geodesic structure of janis-newman-winicour space-time. *International Journal of Theoretical Physics*, 54(8):2905–2920, Jan 2015.

[113] Avijit Chowdhury and Narayan Banerjee. Echoes from a singularity. *Phys. Rev. D*, 102:124051, Dec 2020.

[114] Shohreh Abdolrahimi and Andrey A. Shoom. Analysis of the fisher solution. *Physical Review D*, 81(2), jan 2010.

[115] K. A. Bronnikov and G. N. Shikin. Spherically symmetric scalar vacuum: no-go theorems, black holes and solitons, 2001.

[116] K. A. Bronnikov and J. C. Fabris. Regular phantom black holes. *Phys. Rev. Lett.*, 96:251101, 2006.

[117] Mariano Cadoni and Edgardo Franzin. Asymptotically flat black holes sourced by a massless scalar field. *Phys. Rev. D*, 91:104011, May 2015.

[118] Athanasios Bakopoulos and Theodoros Nakas. Novel exact ultracompact and ultrasparse hairy black holes emanating from regular and phantom scalar fields. *Phys. Rev. D*, 107:124035, Jun 2023.

[119] Mariano Cadoni, Edgardo Franzin, Federico Masella, and Matteo Tuveri. A Solution-Generating Method in Einstein-Scalar Gravity. *Acta Appl. Math.*, 162(1):33–45, 2018.

[120] Jacob D. Bekenstein. Transcendence of the Law of Baryon-Number Conservation in Black-Hole Physics. *Physical Review Letters*, 28(7):452–455, feb 1972.

[121] Jacob D. Bekenstein. Nonexistence of baryon number for static black holes. *Physical Review D*, 5(6):1239–1246, 1972.

[122] K. A. Bronnikov, S. B. Fadeev, and A. V. Michtchenko. Scalar fields in multidimensional gravity. no-hair and other no-go theorems. *General Relativity and Gravitation*, 35(4):505–525, apr 2003.

[123] Shahar Hod. No-go theorem for static boson stars. *Physics Letters B*, 778:239–241, mar 2018.

[124] Mustapha Azreg-Aïnou. Selection criteria for two-parameter solutions to scalar-tensor gravity. *General Relativity and Gravitation*, 42(6):1427–1456, June 2010.

[125] Tullio Regge and John A. Wheeler. Stability of a schwarzschild singularity. *Phys. Rev. D*, 108:1063–1069, Nov 1957.

[126] S. Chandrasekhar. *The Mathematical Theory of Black Holes*. International series of monographs on physics. Clarendon Press, 1998.

[127] Hayato Motohashi and Teruaki Suyama. Black hole perturbation in parity violating gravitational theories. *Phys. Rev. D*, 84:084041, Oct 2011.

[128] Tsutomu Kobayashi, Hayato Motohashi, and Teruaki Suyama. Black hole perturbation in the most general scalar-tensor theory with second-order field equations: The odd-parity sector. *Physical Review D*, 85(8), apr 2012.

[129] Carsten Gundlach, Richard H. Price, and Jorge Pullin. Late-time behavior of stellar collapse and explosions. i. linearized perturbations. *Phys. Rev. D*, 49:883–889, Jan 1994.

[130] Cecilia B M H Chirenti and Luciano Rezzolla. How to tell a gravastar from a black hole. *Classical and Quantum Gravity*, 24(16):4191, jul 2007.

[131] Akihiro Ishibashi and Robert M Wald. Dynamics in non-globally-hyperbolic static spacetimes: II. general analysis of prescriptions for dynamics. *Classical and Quantum Gravity*, 20(16):3815–3826, jul 2003.

[132] Gary T. Horowitz and Donald Marolf. Quantum probes of spacetime singularities. *Physical Review D*, 52(10):5670–5675, nov 1995.

[133] Joã O Paulo M. Pitelli and Patricio S. Letelier. Quantum singularities in static spacetimes. *International Journal of Modern Physics D*, 20(05):729–743, may 2011.

[134] B. Waugh and Kayll Lake. Strengths of shell-focusing singularities in marginally bound collapsing self-similar Tolman spacetimes. *Phys. Rev. D*, 38(4):1315–1316, August 1988.

[135] M. Reed and B. Simon. *Methods of Modern Mathematical Physics. II Fourier Analysis, Self-adjointness.* Academic Press, New York, 1975.

[136] Emanuele Berti, Vitor Cardoso, José A. González, and Ulrich Sperhake. Mining information from binary black hole mergers: A comparison of estimation methods for complex exponentials in noise. *Phys. Rev. D*, 75:124017, Jun 2007.

[137] H. Kodama and A. Ishibashi. A master equation for gravitational perturbations of maximally symmetric black holes in higher dimensions. *Progress of Theoretical Physics*, 110(4):701–722, oct 2003.

[138] Masashi Kimura. A simple test for the stability of a black hole by S-deformation. *Classical and Quantum Gravity*, 34(23):235007, December 2017.

[139] Hyat Huang, Min-Yan Ou, Meng-Yun Lai, and H. Lü. Echoes from classical black holes. *Physical Review D*, 105(10), may 2022.

[140] Cecilia Chirenti, Alberto Saa, and Jozef Skákala. Quasinormal modes for the scattering on a naked Reissner-Nordström singularity. *Phys. Rev. D*, 86(12):124008, December 2012.

[141] Dra žen Glavan and Chunshan Lin. Einstein-gauss-bonnet gravity in four-dimensional spacetime. *Phys. Rev. Lett.*, 124:081301, Feb 2020.

[142] Pedro G. S. Fernandes, Pedro Carrilho, Timothy Clifton, and David J. Mulryne. Black holes in the scalar-tensor formulation of 4d einstein-gauss-bonnet gravity: Uniqueness of solutions, and a new candidate for dark matter. *Phys. Rev. D*, 104:044029, Aug 2021.

[143] Alex Kehagias and Konstadinos Sfetsos. The black hole and FRW geometries of non-relativistic gravity. *Physics Letters B*, 678(1):123–126, jul 2009.

[144] Nijo Varghese and V C Kuriakose. Stability of black holes in horava gravity: Gravitational quasinormal modes. 2009.

[145] Nijo Varghese and V. C. Kuriakose. Evolution of electromagnetic and dirac perturbations around a black hole in horava gravity. *Modern Physics Letters A*, 26(22):1645–1656, jul 2011.

[146] Kai Lin, Nan Yang, and Jin Li. Electromagnetic quasinormal modes in Horava-Lifshitz gravity. *Int. J. Theor. Phys.*, 50:48–55, 2011.

[147] R.A. Konoplya and A. Zhidenko. (in)stability of black holes in the $d > 4$ einstein–gauss–bonnet and einstein–lovelock gravities. *Physics of the Dark Universe*, 30:100697, dec 2020.

[148] Avijit Chowdhury, Saraswati Devi, and Sayan Chakrabarti. Naked singularity in 4d einstein-gauss-bonnet novel gravity: Echoes and instability. *Phys. Rev. D*, 106:024023, Jul 2022.

[149] Dieter R. Brill and John A. Wheeler. Interaction of neutrinos and gravitational fields. *Rev. Mod. Phys.*, 29:465–479, Jul 1957.

[150] Don N. Page and Kip S. Thorne. Disk-Accretion onto a Black Hole. Time-Averaged Structure of Accretion Disk. *ApJ*, 191:499–506, July 1974.

[151] I. D. Novikov and K. S. Thorne. Astrophysics of black holes. In *Black Holes (Les Astres Occlus)*, pages 343–450, January 1973.

[152] Dimitrios Psaltis and Tim Johannsen. A ray-tracing algorithm for spinning compact object spacetimes with arbitrary quadrupole moments. i. quasi-kerr black holes. *The Astrophysical Journal*, 745(1):1, Dec 2011.

[153] Tim Johannsen and Dimitrios Psaltis. Testing the No-hair Theorem with Observations in the Electromagnetic Spectrum. II. Black Hole Images. *ApJ*, 718(1):446–454, July 2010.

[154] Cosimo Bambi. A code to compute the emission of thin accretion disks in non-kerr spacetimes and test the nature of black hole candidates. *The Astrophysical Journal*, 761(2):174, Dec 2012.

[155] Cosimo Bambi, Alejandro Cá rdenas-Avendaño, Thomas Dauser, Javier A. García, and Sourabh Nampalliwar. Testing the kerr black hole hypothesis using x-ray reflection spectroscopy. *The Astrophysical Journal*, 842(2):76, jun 2017.

Oleksandr Stashko

Curriculum Vitae

Department of Physics
Princeton University
+1(609)917-6861
alexander.stashko@gmail.com

Research interests

Relativistic astrophysics	Exotic compact objects, space-time singularities, particles motion, modified gravity
HEP	Bose-Einstein condensation, EoS of strongly interacting matter

Education

2018–2023: (expected) **PhD student**, *Goethe University*, Frankfurt am Main, Germany.
Taras Shevchenko National University of Kyiv, Kyiv, Ukraine
Supervisor: Prof. Dr. Luciano Rezzolla, Prof. Dr. Valery Zhdanov

2016–2018 : **M.Sc. (diploma with honors), Theoretical physics**, *Taras Shevchenko National University of Kyiv*, Kyiv, Ukraine.
Supervisor: Prof. Dr. Valery Zhdanov

2012–2016 : **B.Sc. (diploma with honors), Theoretical physics**, *Taras Shevchenko National University of Kyiv*, Kyiv, Ukraine.
Supervisor: Prof. Dr. Valery Zhdanov

Research Experience

Dec., 2022 – Dec., 2023 **Visiting student research collaborator**, Princeton University, Princeton, USA.

Sept., 2022 – Nov., 2023 **Visiting researcher**, *CERN TH*, Geneva, Switzerland.

Apr., 2022 – Sept., 2022 **Visiting researcher**, *Frankfurt Institute for Advanced Studies*, Frankfurt am Main, Germany.

May, 2017 – Nov., 2022 **Research assistant**, *Taras Shevchenko National University of Kyiv*, Kyiv, Ukraine

Teaching experience

Fall, 2019 **Teaching asistant** of the course "Theory of solitons", Physics Department, Taras Shevchenko National University of Kyiv

Fall, 2017 **Teaching asistant** of the course "Mathematical analysis I", Physics Department, Taras Shevchenko National University of Kyiv

Fall, 2016 **Teaching asistant** of the course "Mathematical analysis I", Physics Department, Taras Shevchenko National University of Kyiv

Skills

Programming Mathematica, Python, Julia

Languages English, Ukrainian, Russian.

Awards

2019-2021 Ukrainian government academic scholarship named after M. Hrushevsky.

List of papers

1. **O. Stashko**, O. Savchuk, and V. Zhdanov. Quasinormal modes of naked singularities in presence of nonlinear scalar fields. ***Phys. Rev. D***, 109:024012, Jan 2024.
2. **O. Stashko**, O. Savchuk, L. Satarov, I. Mishustin, M. Gorenstein, and V. Zhdanov. Pion stars embedded in neutrino clouds. ***Phys. Rev. D***, 107(11), jun 2023.
3. **O. Stashko** and V. Zhdanov. Circular orbits of test particles interacting with massless linear scalar field of the naked singularity. ***Phys. Rev. D***, 106(10), nov 2022.
4. V. Kuznietsov, O. Savchuk, **O. Stashko**, and M. Gorenstein. Critical point influenced by Bose-Einstein condensation. ***Phys. Rev. C***, 106(3), sep 2022.
5. **O. Stashko** and V. Zhdanov. Singularities in static spherically symmetric configurations of general relativity with strongly nonlinear scalar fields. ***Galaxies***, 9(4), Sep 2021.
6. V. A. Kuznietsov, **O. Stashko**, O. Savchuk, and M. Gorenstein. Critical point and bose-einstein condensation in pion matter. ***Phys. Rev. C***, 104(5), Nov 2021.
7. **O. Stashko**, V. Zhdanov, and A. N. Alexandrov. Thin accretion discs around spherically symmetric configurations with nonlinear scalar fields. ***Phys. Rev. D***, 104(10), Nov 2021.
8. **O. Stashko**, O. Savchuk, R. Poberezhnyuk, V. Vovchenko, and M. Gorenstein. Phase diagram of interacting pion matter and isospin charge fluctuations. ***Phys. Rev. C***, 103(6), Jun 2021.
9. **O. Stashko**, D. Anchishkin, O. Savchuk, and M. Gorenstein. Thermodynamic properties of interacting bosons with zero chemical potential. ***Journal of Physics G: Nuclear and Particle Physics***, 48(5):055106, Apr 2021.
10. O. Savchuk, Y. Bondar, **O. Stashko**, R. Poberezhnyuk, V. Vovchenko, M. Gorenstein, and H. Stoecker. Bose-einstein condensation phenomenology in systems with repulsive interactions. ***Phys. Rev. C***, 102(3), Sep 2020.
11. **O. Stashko** and V. Zhdanov. Spherically symmetric configurations in general relativity in the presence of a linear massive scalar field: Separation of a distribution of test body circular orbits. *Ukrainian Journal of Physics*, 64(3):189, Apr. 2019.
12. D. Anchishkin, I. Mishustin, **O. Stashko**, D. Zhuravel, and H. Stoecker. Finite-temperature Bose-Einstein condensation in interacting boson system. *Ukrainian Journal of Physics*, 64(12):1118, Dec. 2019.
13. V. Zhdanov and **O. Stashko**. Static spherically symmetric configurations with N nonlinear scalar fields: Global and asymptotic properties. ***Phys. Rev. D***, 101(6):064064, March 2020.
14. **O. Stashko** and V. Zhdanov. Black hole mimickers in astrophysical configurations with scalar fields. *Ukrainian Journal of Physics*, 64(11):1078, Nov. 2019.
15. I. Mishustin, D. Anchishkin, L. Satarov, **O. Stashko**, and H. Stoecker. Condensation of interacting scalar bosons at finite temperatures. ***Phys. Rev. C***, 100(2):022201, August 2019.
16. **O. Stashko** and V. Zhdanov. Spherically symmetric configurations of General Relativity in presence of scalar fields: separation of circular orbits. ***General Relativity and Gravitation***, 50(9):105, September 2018.